Life Cycle Fatigue Management for High-Speed Vessel Using Bayesian Updating Approaches

by

Jiandao Zhu

A dissertation submitted in partial fulfillment
of the requirements for the degree of
Doctor of Philosophy
(Naval Architecture and Marine Engineering)
in The University of Michigan
2014

Doctoral Committee:

Assistant Professor Matthew D. Collette, Chair
Associate Professor Dale G. Karr
Associate Professor Jerome P. Lynch
Assistant Professor David J. Singer

ACKNOWLEDGEMENTS

Foremost, I would like to express my sincere gratitude to my advisor, Dr. Matthew Collette, for his continuous support of my research, his inspiration, and his patience. I am still thankful that I made decision at beginning to pursue a Ph.D degree under his guidance. Dr. Collette provided me with numerous opportunities to absorb knowledge, to see the world and to grow as a student, an engineer, and a person. All these I will never forget this experience and will always appreciate it for the rest of my life.

In addition to my advisor, I would like to thank the rest of my thesis committee: Dr. Dale Karr, Dr. David Singer and Dr. Jerome Lynch, for their encouragement, insightful comments, and hard questions. Their effort has resulted in much high quality thesis. Also I would like to acknowledge the support of Dr. Paul Hess of the office of naval research code 331 under Grant N00014-10-1-0193.

Several colleagues helped advance my research. I would like to thank Dr. Armin Troesch who answered all my questions during my research and was always supportive, as well as his team: David Hodapp and Dr. Dae-Hyun Kim who provided me with the LAMP data to validate my research.

In addition, I would like to thank Dr. Ray Kuo and Dr. Luis O. Garza-Rios from ExxonMobil & Dr. Dingwu Xia and Robin Preston from BP. Thank you for giving me unique internship projects that helped me to broaden my view of the structural health monitoring world.

I would also like to extend my gratitude to my parents. Mom & Dad, thank you

for giving birth to me, inspiring me become a man who I want to be, and trying your best to support every decision I have made since I was born.

Lastly, I would recognize the effort from Mr. Thomas Bayes (1701-1761). He discovered the famous Bayes' theorem which all fundamental theory of my thesis is based upon. His name and contributions should never be forgotten.

TABLE OF CONTENTS

LIST OF FIGURES

Figure

LIST OF TABLES

Table

LIST OF ABBREVIATIONS

BCC body-centered cubic

BNT Bayes Net Toolbox

CDF cumulative distribution function

CLG conditional linear Gaussian

COV coefficient of variation

CPD conditional probability distribution

CPT conditional probability table

DAG directed acyclic graph

DBN dynamic Bayesian network

DBNs dynamic Bayesian networks

ECA engineering critical assessment

EE empirical equation

EM expectation-maximization

EMD earth mover's distance

FAD failure assessment diagram

FE finite element

FFS fitness-for-service

FFT fast Fourier transform

FORM first-order reliability method

HDBN hybrid dynamic Bayesian network

HMM hidden Markov model

IFFT inverse fast Fourier transform

JHSS joint high-speed sealift

JIP joint industry project

LAMP Large Amplitude Motion Program

LEFM linear elastic fracture mechanics

LR linear regression

LRS linear response surface

MAP maximum a posteriori

MCMC Markov chain Monte Carlo

MH Metropolis-Hasting

PMF probability mass function

POD probability of detection

POF probability of failure

RAO response amplitude operator

RPDD reliability purposed dynamic discretization

SHM structural health monitoring

SIM structural integrity management

SORM second-order reliability method

VBM vertical bending moment

XFEM extended finite element method

ABSTRACT

Life Cycle Fatigue Management for High-Speed Vessels Using Bayesian Updating Approaches

by

Jiandao Zhu

Chair: Matthew Collette

Structural fatigue cracking in lightweight high-speed vessel structures is a central maintenance and lifecycle costing concern. While traditional pass-fail approaches provide a simple design oriented metric to limit the amount of fatigue cracking observed in service, these approaches struggle to make accurate mid-life predictions of future fatigue performance and the associated uncertainties and risks. A stochastic method of modeling crack growth and fatigue life prediction is proposed based on dynamic Bayesian networks. This is a graphical model represented by sequences of random variables with defined conditional independences between these variables. The aim is not only developing a computationally efficient and robust fatigue life prediction model, but also to incorporate the life cycle monitoring results to determine as-built fatigue properties of vessels via a Bayesian updating approach. A robust discretization technique is also studied to facilitate determining specific reliability levels. The model is then extended to consider variable amplitude loading with a Markov chain Monte Carlo load updating strategy. By sampling from the posterior load distribution data at available sea states, the uncertainties of engineering model

used at the initial design stage can be identified and corrected. Thus, a more accurate load prediction integrated with through life information updating is obtained. The proposed framework is then further extended by utilizing simulation data for a specific structural detail generated by using extended finite element method (XFEM). The core idea behind XFEM is to generate the mesh independent of discontinuity domains which makes cycle-by-cycle fatigue cracking simulation possible. The example case study addresses a stiffened panel from joint high-speed sealift (JHSS) with load information simulated by the Large Amplitude Motion Program (LAMP). The results show that both load updating and crack inspection updating are necessary for accurate reliability estimation.

CHAPTER I

INTRODUCTION

1.1 Research background

The marine structural fatigue problem is subject to different types of uncertainty, such as uncertainty in wave loads, structural details, and crack growth mechanism. A typical design stage fatigue life prediction method uses deterministic analyses in conjunction with a safety factor to achieve acceptable performance. Existing methods can be divided into three categories: stress life approach, strain life approach and fracture mechanics based approach. Although these methods have been under development since the early 19th century, they still struggle to make accurate life prediction of future fatigue performance, associated uncertainties, and risks.

A more attractive way to address those uncertainties is under the scope of structural health monitoring (SHM). SHM is a process of implementing a damage identification strategy for aerospace, civil, and mechanical engineering infrastructure *Farrar et al.* (2001). Since an increasing number of vessels have extensive data monitoring systems installed for hull performance and stress monitoring to obtain the life cycle information, this life cycle data can help to support inspection, repair, and life-extension decisions by reducing the uncertainties of design stage fatigue approaches in a cost-effective and risk-acceptable manner for the vessel owner. There has been extensive study of SHM systems for marine and offshore structures. Generally, they

consist of four steps according to *Farrar et al.* (2001):

(1) operational evaluation,

(2) data acquisition, normalization and cleansing,

(3) feature selection,

(4) statistical model development.

Since this dissertation will mainly focus on how to interpret the SHM data related to step four, the detailed review of rest of steps will not be presented here.

1.2 Research overview

The development of statistical models is concerned with the implementation of algorithms that operate on the extracted features to quantify the damage state of the structure (*Farrar et al.*, 2001). In terms obe enf structural fatigue problems, the application of SHM is initially built up from a structural reliability approach, which calculates failure probability in terms of a specified set of limit states for a certain time. Some classic methods were proposed by different authors to solve reliability problems, including simulation, first-order reliability method (FORM)/second-order reliability method (SORM) or direct integration. The details are described in the books by *Ditlevsen and Madsen* (1996) and *Melchers* (1996) and will not be talked about here.

When additional information obtained by inspection or monitoring tools becomes available, that information could be potentially used as a diagnostic and prognostic tool to assess the structural performance for maintenance and repair needs. The simplest study is to use SHM data for design stage validation to improve the design load and structural response estimation. Storhaug and his colleagues (2007; 2011) followed this approach using onboard measurements of wave induced vibration on a container

ship for fatigue damage estimation. *Okada et al.* (2006) compared the design stage analysis and onboard measurement for stress and deflection of a container ship to evaluate the design assumptions. The long-term prediction of each structural component was generally proven to be appropriate, if a little conservative in some regions. Instead of those direct comparisons, a more common approach is to use reliability updating methods. For example, *Jiao and Moan* (1990) developed an analytical approach based on FORM and SORM to update reliability for both one component and system level using proof-loading and non-destructive inspection updating as examples. *Guedes Soares and Garbatov* (1996) studied fatigue reliability of the ship hull girder and using the first two statistical moments to approximate the distribution. Inspection and repair were considered by roughly matching the condition to an intact structure at certain time. Other examples could be found from *Ditlevsen and Madsen* (1996) or *Moan* (2011). All those reliability updating methods stated above try to solve the problem by simplifying the model: either the number of updated random variables or inherent physical relation.

It is also more attractive if a certain degree of artificial intelligence is involved for interpreting the life-cycle data, forecasting the structural conditions, and acting as a decision making support system. *Kesavan et al.* (2007) established the artificial neural networks to build a mapping relationship between structural damage and physical parameters. This was trained from finite element simulation data. *Okasha et al.* (2010b) implemented a statistical damage detection technique using vector autoregressive modelling for detection and localization of damage of a high speed vessel. The methodology was demonstrated using strain data obtained from seakeeping trials of a naval HSV-2.

Besides the techniques mentioned above, the Bayesian approach is also popular, and has been widely applied with SHM by many researchers. The major advantage is that it enables the inclusion of existence design knowledge as prior information.

Therefore, even without extensive life-cycle data, the updated model can still provide a reasonable prediction and reflect the bias of design knowledge as well as remaining uncertainty in prediction. One of major applications is to use Bayesian updating for fatigue reliability prediction as well as inspection and repair planning. *Nielsen et al.* (2011) used a Bayesian approach to estimate the remaining fatigue life with full-scale strain measurements, wave environment data and operation profile records. The fatigue life prediction uses both time domain and frequency domain analysis, which generally coincided. However, in this work, the Bayesian modelling method has only been applied to estimate the wave spectrum. *Rabiei and Modarres* (2013a,b) built a recursive Bayesian framework combined with an acoustic emission based monitoring approach and inspection data for a fatigue diagnostic and prognostic solution. However, the framework assumes pure Gaussian distributions for all inputs, which is a relatively limiting assumption. Also, the updating model highly relies on acoustic emission based technology, which is in limited marine use today. *Straub* (2009) studied the benefits of dynamic Bayesian networks (DBNs) in modelling the deterioration processes. dynamic Bayesian network (DBN) is a Bayesian network relating variables to each other over adjacent time steps. His study showed potential in monitoring, inspection, maintenance, and repair planning. The major advantage of DBN model is that it converts all stochastic distribution into a discrete space, therefore, there is no restriction in type of distribution prior or posterior with SHM data being presented. However, the generation of conditional probability relationships specified by conditional probability table (CPT) is troublesome, and the reliability estimation often requires a small failure probability calculation from discrete mass function, which could be sensitive to the generation of conditional probability relations. *Mohanty et al.* (2011, 2010) developed multivariate Gaussian process model for both offline and online fatigue crack prediction. The model is trained by fatigue test experiment data, and results indicate that the rate-based prediction model has better correla-

tion with actual crack size compared with direct crack size prediction. *Sankararaman et al.* (2011) further connected a finite element model, crack growth model, and Gaussian process surrogate model through a Bayesian network for the uncertainty analysis and model validation. The Bayesian hypothesis test has been used together with a confidence metric to access the validity and quantify the confidence in fatigue crack growth prediction. The proposed Bayesian framework can easily accommodate other advanced analysis models and corresponding model uncertainty. *Ling and Mahadevan* (2012) predicted loading sequence by constructing a Bayesian autoregressive integrated moving average model with real-time load monitoring data. He then integrated this into a fatigue damage prognosis framework aided by Gaussian process surrogate modelling. Sensitivity analysis has also been studied using Bayesian networks. *Cohen et al.* (2011) compared the Monte Carlo simulation and stochastic Bayesian approach to examine the probability of crack detection using a truncated initial crack length. *An et al.* (2011) used Markov chain Monte Carlo (MCMC) simulation to incorporate field data from multiple identical locations as prior knowledge and obtain a refined fatigue life distribution. However, the fatigue model applied is based on stress life approach which is relatively simple. *Zárate et al.* (2012) used MCMC simulation as model updating and prognosis tools for fracture mechanics based fatigue crack growth. However, the uncertainties in the stress intensity range and loading are considered by a series of proposed polynomial equations, which may be sensitive to the assumed degree of freedom.

Other applications include life-cycle ship structural performance assessment by integrating SHM data into the bending moment prediction (*Okasha et al.*, 2010a); wave estimation for navigational support using ship response measurement data (*Pascoal and Guedes Soares*, 2009; *Nielsen and Jensen*, 2011); time variant corrosion degradation (*Straub and Faber*, 2007); assessment seismic fragility from empirical data (*Straub and Der Kiureghian*, 2008); optimal sensor placement for detecting cracks of unknown

location (*Flynn and Todd*, 2010).

Instead of working on one component or one failure type, a system level integrity management using Bayesian network has also been studied by many authors. One advantage is that it facilitates the modelling process of combining different related components into a single framework, while sensitivity analysis provides a measure of the contribution from a particular source due to observation. An overview paper can be found by *Weber et al.* (2012). *Jensen and Mansour* (1994) used Bayesian updating to calculate system level reliability based on inspection results and repair strategies for a large number of identical structural details. However, an analytical expression of Paris' law is applied, since the geometry function is assumed to be independent of crack length. This only applies to the crack on simple structures such as an edge crack or a center crack, while the analytical solutions are generally unknown for more complicated structural details. *Mahadevan et al.* (2001) used Bayesian networks to estimate and improve reliability of a structural system with multiple correlated failure sequences. Although the structure system illustrated is simple, it shows the potential of Bayesian network to solve the reliability problems. *Friis-Hansen* (2000) applied the Bayesian networks as a decision making support tools into different marine applications including inspection planning, upheaval buckling and condition monitoring of marine diesel engines. *Montes-Iturrizaga et al.* (2009) studied progressive deterioration due to combined effect of different damage for structural integrity management (SIM) of a jacket. Later his team (*Faber et al.*, 2012; *Heredia-Zavoni et al.*, 2012) also applied the Bayesian network to assess the different failure scenarios of a FPSO system.

Developing efficient Bayesian tools to handle computational expensive reliability problems is another interesting research area. *Bensi et al.* (2013) developed efficient Bayesian network formulations by using discrete optimization algorithm for modelling system level reliability. *Straub* (2011) presented a novel solution to reliability updat-

ing when measurements monitoring and other information of the equality type are available, while most of other reliability problems deal with unequal information. In the meantime, he (*Straub and Kiureghian*, 2010a,b) combined the Bayesian Networks with the structural reliability method to create an enhanced Bayesian Network for engineering risk and reliability analysis. The proposed network enables efficient and accurate assessment of probabilities of rare events represented by computationally demanding physically based models. *Neil et al.* (2007) developed dynamic discretization algorithm for a general class of hybrid Bayesian network. An entropy function has been introduced to measure the error and iteratively adjust the error accordingly. Later, they *Marquez et al.* (2010) applied their algorithm to structural reliability analysis for a robust and efficient reliability output.

1.3 Research contribution

In this dissertation, An accurate reliability based fatigue life prediction framework relying on life-cycle SHM data by using Bayesian updating techniques has been proposed. Various SHM data has been collected and incorporated into the proposed framework, which includes sea environment, vessel operational profile, load as well as inspection records. The proposed methods are composed of two parts: a lifetime load updating framework and life-cycle fatigue management using both stress life (S-N) based approach and fracture mechanics approach.

The primary contributions of this thesis can be summarized as:

1. For the load updating framework, a two-level updating strategy was proposed including a cell-based updating method by using MCMC method as well as a lifetime load updating method by constructing a hierarchical Bayesian model. Three updating parameters are selected to capture the impact of ship speed on the experienced loads, wave height on the skewness of the load distribu-

tion, and the bandwidth of the loading process. Using the MCMC method, distributions for these parameters are found for observed cells in cell-based updating approach. To predict these parameters in unobserved cells, hierarchical Bayesian models are used to establish mapping relations between uncertainty factors and their influencing parameters in the operational profile. The model are then trained via the data from the observed load cells. Different model and learning approaches are explored to compare the updated factors in unobserved cells which leads to refined prediction of lifetime loading.

2. A stress life based fatigue management approach was proposed based on the concept of estimating the as-built fatigue properties of a high-speed vessel through crack inspection results. This approach treats the vessel as an on-going fatigue experiment. By using local fatigue approaches, the number of fatigue parameters that must be determined is significantly reduced. Two different methods of interpreting inspection results and predicting future fatigue performance were presented: a simple logit regression approach and a probit regression approach based on determining the overall life distribution factors. The MCMC method has been proposed to update this model.

3. A reliability based dynamic discretization method was proposed which extends upon a model introduced by (*Straub*, 2009), where a DBN is used to model a general structural deterioration process. However, the focus of the investigation is the accuracy of the reliability output and it relationship to the discretization scheme, including cases with inspection evidence. The goal for the proposed algorithm is to find an optimum discretization method for DBN based deterioration processes with lower computational complexity while achieving the same level of accuracy for reliability analysis as conventional discretization methods.

4. The load updating model and DBN based deterioration process model are in-

tegrated. The updated load is transferred to stress distribution for an accurate load input in the fatigue crack growth model. A stiffened panel on the upper deck of JHSS mid-section was illustrated as an example. A crack growth model using the extended finite element method (XFEM) technique has also been built to predict the stress intensity factor during the crack propagation. With the help of the proposed dynamic discretization, the updated load data, crack inspection records as well as stress intensity factor predicted by XFEM are all incorporated into the DBN based deterioration process model to predict reliability accurately and efficiently.

CHAPTER II

BACKGROUND TO BAYESIAN METHODS

2.1 Introduction

The objective of this chapter is to introduce the theory upon which the examples of the following chapters are based. The following sections start with the introduction of Bayesian networks, which play an important role in this thesis. Next, Bayesian updating approaches will be introduced. This section is grouped into Bayesian inference methods and Bayesian learning methods. These updating methods have different strength and weakness making them suitable for particular problem features.

2.2 Bayesian networks

A Bayesian network is a directed acyclic graph (DAG) where the nodes represent the stochastic system variables and arcs symbolize the dependencies or the cause-effect relationships among the variables. A simple Bayesian network example is shown in Fig. 2.1. It is formed by the nodes X, Y, Z, together with directed edges: X and Y are called parents of Z, while Z is the child of X and Y. The nodes may be observable evidence, latent variables or parameters. Edges represent the conditional dependencies between connected nodes. A conditional probability relation should be specified for each node in terms of its state and that of its attached parents.

This relation could be a discrete conditional probability table or a continuous based conditional relation. Hence, it is a graphical representation of conditional probability and causality relationships between variables.

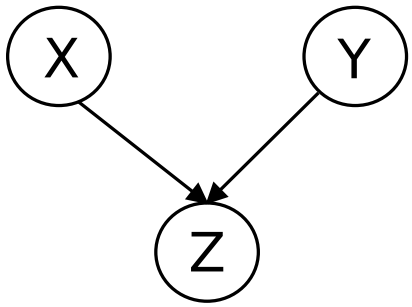

Figure 2.1: A three nodes Bayesian network.

2.3 Use Bayesian approaches to interpret structural health monitoring data

The Bayesian approaches estimates the degree of belief in a hypothesis based on collected evidence. The theorem can be derived from Bayes' rule. For the Fig. 2.1, the probability of event x_i happens given observation of z_i state is

$$P(x_i|z_i) = \frac{\sum_Y P(z_i|x_i, Y)P(Y)}{P(z_i)} \tag{2.1}$$

where $P(Y)$ is a prior distribution and $P(z_i|x_i, Y)$ is called the likelihood function, which is also the conditional relation specified at first.

One of promising areas of using Bayesian inference is to interpret the SHM data. For a SHM problem, Z normally represents certain monitoring data obtained during a vessel's operation and the X and Y represent their related variables. However, in reality, the inference of Bayesian network for SHM can be much more challenging than a simple network shown in Fig. 2.1 for four main reasons:

(1) the observation Z can be related with multiple variables, or even multiple layers

of variables,

(2) Some of variables may be unobservable (latent variables) or the relation between variables and observation may be unclear,

(3) Different sources of uncertainty may exist including measurement uncertainty, model uncertainty and prior knowledge uncertainty,

(4) Not enough data is available to train the model. Especially for rare events, it takes longer time or more frequent inspections for one to be observed.

The item one relies on tools of inferring the network. Although the inference of a Bayesian network has been proven to be a NP hard problem (*Darwiche*, 2009), various algorithms have already been developed for this task. Those algorithms can be generally divided into exact inference algorithms (e.g., junction tree, variable elimination), deterministic approximation inference algorithms (e.g., loopy belief propagation), and stochastic approximation algorithms (e.g., MCMC, particle filtering). Since the Bayesian inference in this thesis will be performed mainly by MCMC and junction tree algorithms, only these two algorithms will be introduced in the Sections 2.4.1 and 2.4.3 respectively. The details of the remaining algorithms will not be presented and can be found in most Bayesian network books such as *Darwiche* (2009).

Item two relates with training the model with available data and selecting the best hypothesis in terms of how well it can explain data. Typically, the purpose of training is to make predictions for future cases in which only the inputs to the network are known. Compared with conventional learning methods, Bayesian learning not only predicts the expectation but also the confidence level based on data. However, one challenge is to adapt to different characteristics of SHM data, such as how to incorporate data which is uncertain (e.g., input is a distribution instead of a value

or how to identify the uncertain relations for SHM data). These problems will be addressed in Section 2.5.

Item three and item four both rely on how to construct an appropriate network to quantify different sources of uncertainties and accurately predict rare events. Since each node represents a random variable in a Bayesian model, if the inherent physical relations could be captured correctly by the model, the stochastic distribution for each node is expected to be updated, which also leads to a refined prediction. These issues are more problem specific and will be addressed in the the example cases in the following two chapters.

2.4 Bayesian inference

2.4.1 Junction tree algorithm

Junction tree algorithm is one of most widely used algorithms to infer the Bayesian network, which is originally developed by *Lauritzen and Spiegelhalter* (1988), *Jensen et al.* (1990), and *Jensen* (1996). A junction tree is a representation of the probabilistic model equivalent to that of the network that enables efficient and consistent updating of the model.

Below, a step-by-step description of this inference algorithm will be presented. The algorithm is illustrated according to an example of a so-called hidden Markov model (HMM) defining in Fig. 2.2. The example is directly related with the crack growth model that we will construct in the following chapters.

2.4.1.1 Moralize the graph

Consider an DAG Ω as shown in Fig. 2.2, the moral graph is an undirected graph which is constructed as follows:

1. For each node N in Ω, add an undirected edge between every pair of its parents,

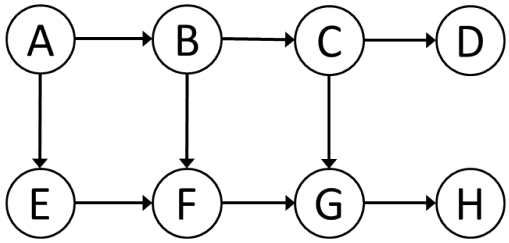

Figure 2.2: A HMM example.

if an arc does not already connect them.

2. Convert every directed edge in Ω to an undirected edge.

For example, since there is no arc linking the parents B, E of F, the edge linking the B and E is added. The same step occurs for the parents C, F of G. The corresponding moral graph is shown in Fig. 2.3.

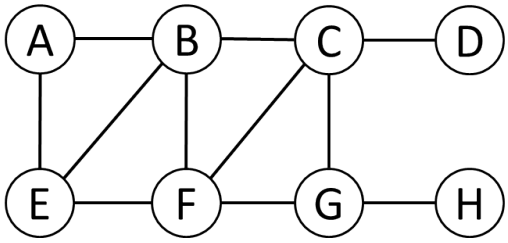

Figure 2.3: The corresponding moral graph of HMM.

2.4.1.2 Triangulation

The objective of this step is to identify subsets of nodes of the moral graph called clusters. This involves determining an ordering of the nodes, and then using node elimination to obtain a set of elimination cliques. One way of doing this is eliminating according to the minimum weight of each node. The minimum weight of the node is defined as follows:

Definition II.1. For any node N, the weight of N is the number of edges that needs to be added to its set of neighbors to ensure that the N and its neighbours form a

complete sub-graph.

Definition II.2. A complete graph is one in which every pair of distinct nodes is connected by an edge.

Definition II.3. A maximal complete sub-graph is one that is not only complete but that is not contained in any larger, complete subgraph.

The procedure of triangulating the moral graph is given as follows:

1. Determine the node N with minimum weight. This relates to identify additional edges that may need to be added to neighbours of N.
2. Add the edges identified in the previous step to the graph.
3. Define as a cluster the node N and its neighbours.
4. Remove the node N from the graph.

Again, take Fig. 2.3 as example, Table 2.1 shows each step the minimum weight nodes, removed node and formed cluster.

Step	Minimum Weight Nodes	Removed Nodes	Cluster
1	A, D, H	A	ABE
2	E, D, H	D	CD
3	E, H	H	GH
4	G, E	G	GCF
5	E, C	E	BEF
6	B, C, F	B	BCF
7	C,F	C	CF
8	F	F	F

Table 2.1: The process of triangulation for HMM example.

2.4.1.3 Creation of junction tree with cliques

The junction tree can then be formed by connecting the clusters obtained in previous step. The process is as follows:

1. Remove any cluster that is a subset of another cluster.

2. For the remaining n clusters, iteratively insert edges between pairs of clusters until the clusters are connected by $(n-1)$ edges. This can also be viewed as inserting $(n-1)$ separators between clusters. A separator between two clusters is defined as a common subset of the nodes in the two clusters.

3. Select the candidate separators by choosing the separator with the highest number of members.

For the example case, after the removal step, there are six clusters left: BAE, BEF, BCF, CD, GCF, GH. The candidate separators include separator BE between clusters BAE and BEF, separator BF between clusters BEF and BCF, separator CF between clusters BCF and GCF, separator C between clusters BCF and CD, and separator G between clusters GCF and GH. The junction tree is shown in Fig. 2.4 where the rectangle denotes the separator while the circular node denotes cluster.

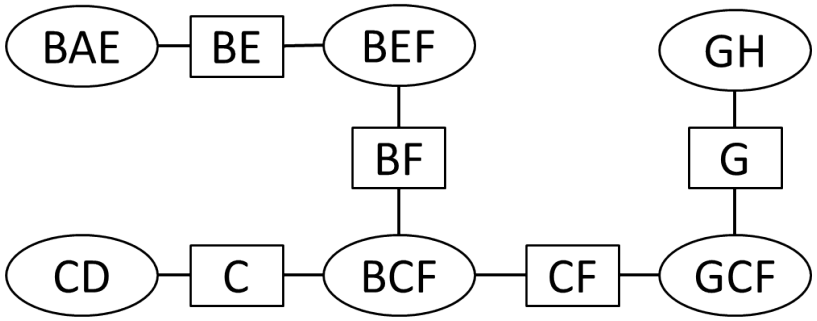

Figure 2.4: The junction tree for HMM example.

2.4.1.4 Propagation in a junction tree

The propagation algorithm for a junction tree relies on the basic message passing algorithm between the two clusters. Here the so-called Hugin architecture is

discussed, which is relatively time efficient compared with the Shafer-Shenoy architecture. Further reading could be found in *Jensen et al.* (1990); *Shenoy and Shafer* (1990); *Lepar and Shenoy* (1998).

Consider a simple example of a Bayesian network as shown in Fig. 2.5(a). Its

(a) (b)

Figure 2.5: Bayesian network (left) and junction tree (right) for crack propagation example.

corresponding junction tree is shown in Fig. 2.5(b). Two clusters are formed given that Bayesian network example: cluster V, which is composed of node A and B, and cluster W, which is composed of node B and C. V and W have a non-empty intersection S, which is the separator of two clusters. A potential is defined as a function over a set of variables, mapping each instantiation of these variables to a non-negative number. For this case, the clusters V and W have the potentials ψ_V and ψ_W and the separator S also has its potential ϕ_S. For the following paragraphs, we always denotes ψ as the potential of the cluster and ϕ as the potential of the separator. The message passing algorithm is an exchange of information between V and W. Therefore, following cluster tables could be obtained:

$$\psi_V = P(B|A)P(A) \tag{2.2}$$

$$\psi_W = P(C|B) \tag{2.3}$$

If there is an evidence observed at cluster W, either on node B or node C, the updated V and S, which denotes ψ_V^* and ϕ_S^* could be obtained:

$$\psi_V^* = \psi_V \frac{\phi_S^*}{\phi_S} \tag{2.4}$$

$$\phi_S^* = \sum_{W \setminus S} \psi_W \tag{2.5}$$

The first equation marginalizes the potential ψ_W with respect to S and stores the result as the separator potential. The second equation rescales the potential on V by multiplying by an likelihood factor that is the ratio of the new separator potential to its old value.

If the information needs to be passed from V back to W using the same rules, it follows that:

$$\phi_S^{**} = \sum_{V \setminus S} \psi_V^* \tag{2.6}$$

$$\psi_W^{**} = \psi_W^* \frac{\phi_S^{**}}{\phi_S^*} \tag{2.7}$$

It can be proven that the ψ_V^{**} and ψ_W^{**} satisfy local consistency condition with respect to their separator S which is shown as follows:

$$\sum_{W \setminus S} \psi_W^{**} = \psi_S^{**} = \phi_S^* \frac{\phi_S^{**}}{\phi_S^*} = \frac{\phi_S^{**}}{\phi_S^*} \sum_{V \setminus S} \psi_V^* = \sum_{V \setminus S} \frac{\phi_S^{**}}{\phi_S^*} \psi_V^* = \sum_{V \setminus S} \psi_V^{**} \tag{2.8}$$

Then the updated probability could be marginalized from the corresponding cluster, which implies:

$$\begin{aligned} P(A) &= \sum_B \psi_V^* \\ P(B) &= \sum_C \psi_W^* = \sum_A \psi_V^* \\ P(C) &= \sum_B \psi_W^* \end{aligned} \tag{2.9}$$

To pass the message in a junction tree, the following protocol needs to be obeyed: A cluster can send a message to a neighbouring cluster only when it has received message from all of its other neighbours. The process is composed of two steps: collecting evidence and distributing evidence. Again, take the Fig. 2.4 for example. If probability of P(A) needs to be calculated, the cluster of BAE is found as a temporary root. Then all the messages are sent in the direction of cluster BAE starting from the leaf cluster (CD, GH). The message ϕ_G and ϕ_C are placed at the

separator G and C respectively. Then, after collecting the message ϕ_G, the cluster GCF assembles the message with its potential ψ_{GCF}, and sends the message ϕ_{CF} out. Again, the cluster BCF collects the message ϕ_C and ϕ_{CF}, and assembles them with its own potential ψ_{BCF} to form ϕ_{BF}. Finally, the cluster BEF collects ϕ_{BF}, and sends the message to cluster BAE.

When collection and distribution of evidence has been performed, we have performed a full propagation. When another marginal $P(X)$ needs to be calculated, a cluster V that contains X is found, and the joint probability $P(V)$ of V can be calculated by assembling the incoming messages and cluster potential. The $P(X)$ is then a projection of $P(V)$ down on to X.

2.4.2 Inference of a dynamic Bayesian network

A DBN is a special class of Bayesian network which relates random variables to each other over adjacent time steps. The DBN is normally used to model a dynamic system, each time when a new observation arrives, the time index t is increased by one. Therefore, the model consists of a sequence of slices, each of which consists of one or more Bayesian network nodes. The slices are connected by directed links from nodes in slice t to nodes in slice $t+1$. Consider a example of DBN as shown in Fig. 2.6, which is a time-frame extension of Fig. 2.2 with semi-infinite collection of random variables.

To infer the example DBN, three types of probability need to be defined first: a prior probability $P(A_1)$, state-transition functions including $P(B_1|A_1)$, $P(C_1|B_1)$, $P(A_t|A_{t-1})$, $P(B_t|B_{t-1}, A_t)$ and $P(C_t|C_{t-1}, B_t)$ (notice that $P(B_1|A_1)$ and $P(B_t|B_{t-1}$ are different since the parent of B_1 is A_1, while the parents of B_t is B_{t-1} and A_t. Similar for C_t nodes), and an observation function $P(D_t|C_t)$.

The inference methods can be applied for solving three problems: filtering, smoothing and prediction. Take the DBN shown in Fig. 2.6 as example and denote h_t as

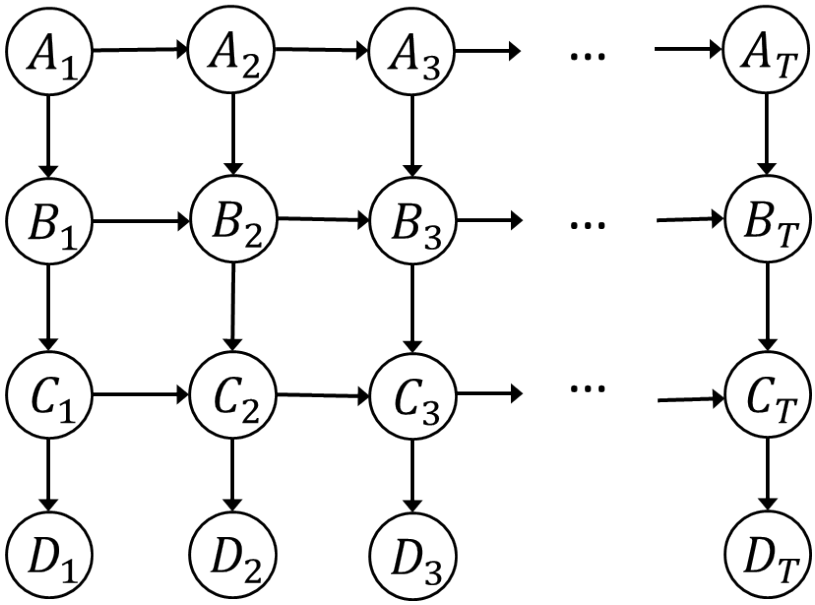

Figure 2.6: A DBN example.

hidden nodes (i.e. unobserved nodes), which include all the random variables at time t except observation D_t. Then, filtering is estimating the posterior distribution over the time t, which is $P(h_t|D_{1:t})$. The smoothing problem is estimating the state of the past given all the evidence up to the current time T, which is $P(h_t|D_{1:T})$. The prediction problem is to predict the future, which is $P(h_{t+h}|D_{1:t})(h > 0)$. The simplest way of doing this is by "unrolling" the DBN into a static Bayesian network and infer the model by using a junction tree algorithm presented above. Also, in certain cases, when all the conditional probability distribution (CPD) is linear Gaussian, the analytical solution is available by using Bayesian linear regression (*Carlin and Louis*, 2009) or Kalman filter (*Kalman*, 1960).

A more advanced method has been developed for DBN allowing an "online inference" which uses constant memory space and computational time per iteration (Murphy 2002). Three methods have been developed for online inference including the basic backward and forward algorithm, the frontier algorithm, and the interface algorithm. Here, the frontier algorithm is described, which is an extended version of the

forward-backward algorithm. The basic idea is to "sweep" a Markov blanket across the DBN composed of a forward pass step which computes $\alpha_t(i) = P(X_t = i|D_{1:t})$ and then backward pass step which computes $\beta_t(i) = P(D_{t+1:T}|X_t = i)$. Then they are combined into a final answer $\gamma_t(i) = P(X_t = i|D_{1:T}) \propto \alpha_t * \beta_t$.

Again, take the Fig. 2.6 as example, the nodes in the Markov blanket will be denoted by F; the nodes to the left and right of the frontier will be denoted by L and R. h_F refers to the hidden nodes in F, e_F refers to the evidence in F, e_L refers to the evidence in L, and e_R refers to the evidence in R. Therefore, in the forward pass, the move of Markov blanket should follow following rules: a node X is added when all its parents are already in the frontier. Therefore, the joint probability distribution can be rewritten as

$$P(e_L, e_F, h_F, X) = P(e_L, e_F, h_F)P(X|e_F, h_F) \tag{2.10}$$

Similarly a node X can be removed when all of its children are in the Markov blanket. There are two cases: If that X is a hidden node, we can obtain that the joint probability is the marginalization in terms of X.

$$\begin{aligned} P(e_{L+X}, e_{F-X}, h_{F-X}) &= P(e_L, e_F, h_{F-X}) \\ &= \sum_X P(e_L, e_F, X, h_{F-X}) \\ &= \sum_X P(e_L, e_F, h_F) \end{aligned} \tag{2.11}$$

if the X is observed, then the marginalization is skipped.

$$\begin{aligned} P(e_{L+X}, e_{F-X}, h_{F-X}) &= P(e_{L+X}, e_{F-X}, h_F) \\ &= P(e_L, e_X, e_{F-X}, h_F) \\ &= P(e_L, e_F, h_F) \end{aligned} \tag{2.12}$$

For the backward pass, the Markov blanket can be advanced from slice $t + 1$ to slice t by adding and removing nodes in the opposite order used in the forward pass. Again, when a node X is added to F, because X is removed at this step in the forward

pass and all X's children are in F, which "shield" X from e_R, the joint probability of $P(e_R|e_F, h_F, X) = P(e_R|e_F, h_F)$. So, adding X simply means expanding the domain of the frontier that contains it. To remove node X from F, we want to compute $P(e_{R+X}|e_{F-X}, h_{F-X})$ from $P(e_R|e_F, h_F)$. Again, two cases have been discussed, if X is a hidden node, then $e_{R+X} = e_R$, and $e_{F-X} = e_F$. Therefore, the X' CPD node is multiplied to the current Markov blanket and then marginalized. Then, following equation holds:

$$\begin{aligned} P(e_{R+X}|e_{F-X}, h_{F-X}) &= P(e_R|e_F, h_{F-X}) \\ &= \sum_X P(X, e_R|e_F, h_{F-X}) \\ &= \sum_X P(X|e_F, h_{F-X}) P(e_R|X, e_F, h_{F-X}) \\ &= \sum_X P(X|e_F, h_{F-N}) P(e_R|e_F, h_F). \end{aligned} \tag{2.13}$$

If X is observed, the step is the same, except X doesn't need to be marginalized.

$$\begin{aligned} P(e_{R+X}|e_{F-X}, h_{F-X}) &= P(e_{R+X}|e_{F-X}, h_F) \\ &= P(e_X, e_R|e_{F-X}, h_F) \\ &= P(e_X|e_{F-X}, h_F) P(e_R|e_X, e_{F-X}, h_F). \end{aligned} \tag{2.14}$$

Fig. 2.7 shows the "sweep" of the Markov blanket for the frontier algorithm using the example of DBN in Fig. 2.6. Therefore, for the forward pass, the node A_2 is added, followed by the removal of node A_1 since all the children of A_1 are in the "blanket". Then node B_2 is added followed by the removal of B_1. When node D_1 is removed, we would say that the Markov blanket moves one time step. The backward pass does the similar thing except the "add" and "remove" operations are reversed compared to the forward pass. One thing needs to be noticed is when doing "add" and "remove" operations for each node, the "remove" step should always have high priority since this will lead to reduced dimensions of joint probability density function for Markov

blanket, which tends to reduce computational cost.

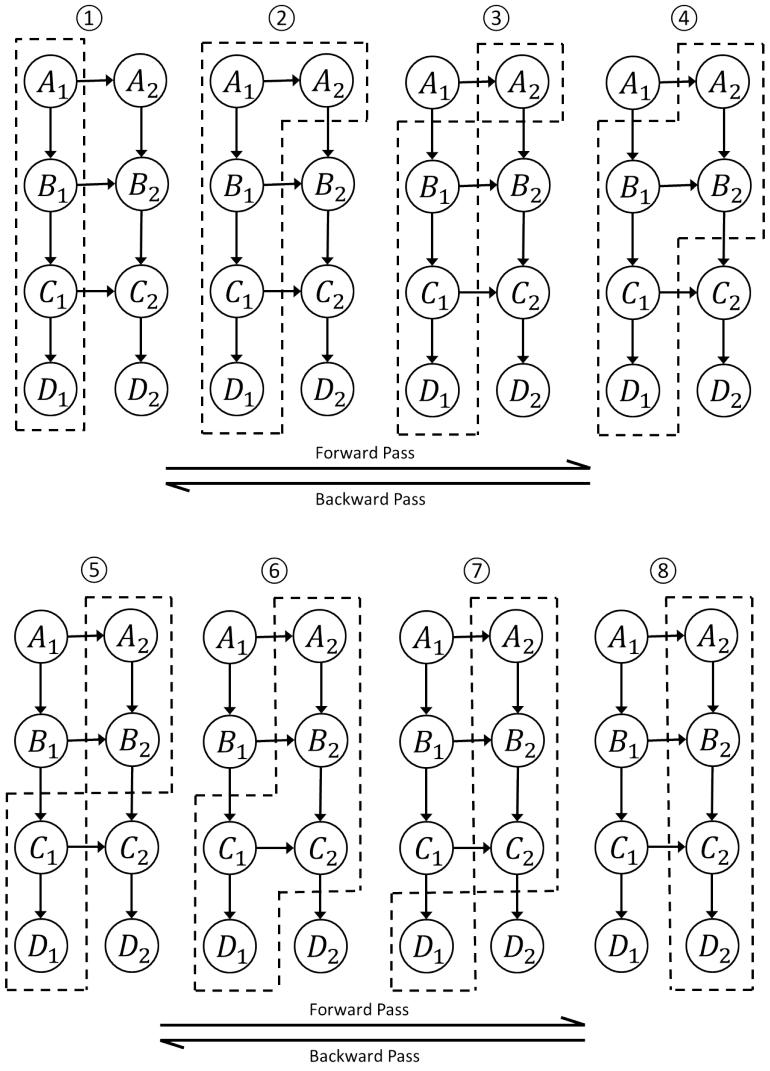

Figure 2.7: The sweep of Markov blanket for frontier algorithm applied into example in Fig. 2.6.

2.4.3 MCMC method

Unlike exact inference (i.e. junction tree algorithm or frontier algorithm) which calculates the actual probability, MCMC is a method of sampling from probability distribution based on constructing a Markov chain. The method belongs to the group

of approximate inference algorithms. The overview of MCMC method presented in this section is based on that presented in *Gamerman and Lopes* (2006). Given a function $f(\Phi)$ and an underlying distribution $P(\Phi)$, a Markov chain is a sequence of random variables $\Phi = \{\Phi_1, \Phi_2, ...\Phi_n\}$. a series of samples $\phi = \{\phi_1, \phi_2, \phi_3, \ldots, \phi_n\}$ is then generated from the distributions of $P(\Phi_1)$, $P(\Phi_2|\phi_1)$, $P(\Phi_3|\phi_2)$, $P(\Phi_4|\phi_3)$, ..., $P(\Phi_n|\phi_{n-1})$ respectively. If that Markov chain satisfies some properties, then MCMC does not have to sample directly from the distribution of $P(\Phi)$ and it can be proven that the sample mean converges to the expectation of distribution of $P(\Phi)$. This facilitates the calculation of distribution $P(\Phi)$, especially when related $f(\Phi)$ cannot be explicitly expressed.

In the following paragraphs, the properties of Markov chains that guarantee the consistency of estimates produced by MCMC will be defined.

2.4.3.1 Markov chains

A Markov chain is defined as follows: define a set of states $S = s_1, s_2, s_3, s_4, ..., s_r$. The process starts in one of these states and moves successively from one state to another. Each move is called a step. If the chain is currently in state s_i, then it moves to state s_j at the next step with a probability denoted by q_{ij}, and this probability does not depend upon which states the chain was in before the current state. The probability q_{ij} is called transition probability which denotes $q_{ij} = P(\Phi_k = s_j|\Phi_{k-1} = s_i)$. The above definition for Markov chain is defined under discrete space. For a continuous space Markov chain, everything is similar except the transition probability is a continuous distribution which is no longer a CPT.

Suppose if a Markov chain has a initial distribution of $P(\Phi_1)$ which is set to some given distribution $\pi(\Phi)$. If generated samples for any ϕ_k still satisfy the distribution of $\pi(\Phi)$, we say that $\pi(\Phi)$ satisfies the stationary distribution for the Markov chain. Also if every state ϕ' is reachable from every other state ϕ, which means that $P(\Phi_i =$

$\phi'|\Phi_1 = \phi)$, we say that a Markov chain is irreducible. The states of the Markov chain are said to be recurrent if each state is guaranteed to be visited an infinite number of times when we simulate the chain. Also the following theorem holds.

Theorem II.1. Let Φ_1, Φ_2, $\Phi_3, \ldots, \Phi_n$ be an irreducible Markov chain and let $\pi(\Phi)$ be its stationary distribution. Let $f(\Phi)$ be a function and $\phi_1, \phi_2, \phi_3, \ldots, \phi_n$ be a sample simulated from the given Markov chain. It can be proven that the sample mean converge to the expectation of function f:

$$\lim_{n\to\infty} \frac{1}{n} \sum_{i=1}^{n} f(\phi_i) = E(f) = \sum_{\phi} f(\phi)\pi(\phi).$$

Therefore, to use the MCMC algorithm, an irreducible Markov chain needs to be constructed with an appropriate stationary distribution. It can be further proven that following relations exists.

Theorem II.2. A stationary process is reversible iff there exists a positive collection of numbers $\pi(\phi_i)$ summing to unity such that

$$\pi(\phi_i)P(\Phi_k = \phi_j|\Phi_{k-1} = \pi_i) = \pi(\phi_j)P(\Phi_k = \pi_i|\Phi_{k-1} = \phi_j)$$

This condition is knows as detailed balance. It can be further proven that if a Markov chain satisfies a detailed balance condition, then $\pi(\Phi)$ is guaranteed to be a stationary distribution. Therefore, the task becomes to construct a Markov chain which satisfies the detailed balance condition.

Two algorithms will be introduced in the next two section for constructing reversible Markov chains systematically called Metropolis-Hasting (MH) algorithm and Gibbs sampling.

2.4.3.2 Metropolis-Hasting algorithm

The MH algorithm stems from papers by *Metropolis et al.* (1953) and *Hastings* (1970). These are considered as basic papers for the characterization of the method.

Consider a distribution $\pi(\Phi)$ from which a sample must be drawn via Markov chains. According to the detailed balance condition, a kernel function $K(\phi_i, \phi_j)$ has

been constructed in a way such that $\pi(\Phi)$ is the equilibrium distribution of the chain.

According to *Metropolis et al.* (1953), the kernel function $K(\phi_i, \phi_j)$ consists of two elements: an arbitrary transition kernel $q(\phi_i, \phi_j)$ and a probability $\alpha(\phi_i, \phi_j)$ such that

$$K(\phi_i, \phi_j) = q(\phi_i, \phi_j)\alpha(\phi_i, \phi_j),\ if\ \phi_i \neq \phi_j \tag{2.15}$$

where $q(\phi_i, \phi_j)$ is the density of kernel function. Therefore, when $\phi_i = \phi_j$, the kernel function can be written as

$$K(\phi_j, \phi_j) = 1 - \int q(\phi_i, \phi_j)\alpha(\phi_i, \phi_j)d\phi_i \tag{2.16}$$

Then the transition kernel of this Markov chain can be grouped in the general expression which is given by

$$P(\phi_i, A) = \int_A K(\phi_i, \phi_j)d\phi_j + r(\phi_i)I_A(\phi_i) \tag{2.17}$$

where

$$K(\phi_i, \phi_j) = q(\phi_i, \phi_j)\alpha(\phi_i, \phi_j) \tag{2.18}$$

$$r(\phi_i) = 1 - \int q(\phi_i, \phi_j)\alpha(\phi_i, \phi_j)d\phi_j \tag{2.19}$$

Hastings (1970) proposed a method to define $\alpha(\phi_i, \phi_j)$ which is the acceptance probability for the Markov chain moving from ϕ_i towards ϕ_j.

$$\alpha(\phi_i, \phi_j) = \begin{cases} min(\frac{q(\phi_i,\phi_j)\pi(\phi_i)}{q(\phi_j,\phi_i)\pi(\phi_j)}, 1) & \pi(\phi_i)q(\phi_i, \phi_j) > 0 \\ 1 & \pi(\phi_i)q(\phi_i, \phi_j) = 0 \end{cases} \tag{2.20}$$

It is shown below that the transition kernel $K(\phi_i, \phi_j)$ satisfies detailed balance equation.

Theorem II.3. The transition kernel for MH algorithm satisfies detailed balance condition.

Proof. if $q(\phi_i, \phi_j)\pi(\phi_i) = q(\phi_j, \phi_i)\pi(\phi_j)$, hence, $\alpha(\phi_i, \phi_j) = \alpha(\phi_j, \phi_i) = 1$. This implies

that

$$K(\phi_i, \phi_j)\pi(\phi_i) = q(\phi_i, \phi_j)\pi(\phi_i) \; and \; K(\phi_j, \phi_i)\pi(\phi_j) = q(\phi_j, \phi_i)\pi(\phi_j)$$

Therefore, we can have that $K(\phi_i, \phi_j)\pi(\phi_i) = K(\phi_j, \phi_i)\pi(\phi_j)$ showing that the detailed balance equation holds.

If $q(\phi_i, \phi_j)\pi(\phi_i) > q(\phi_j, \phi_i)\pi(\phi_j)$, in which case:

$$\alpha(\phi_i, \phi_j) = \frac{q(\phi_i, \phi_j)\pi(\phi_i)}{q(\phi_j, \phi_i)\pi(\phi_j)} \; and \; \alpha(\phi_j, \phi_i) = 1$$

Hence:

$$\begin{aligned} K(\phi_i, \phi_j)\pi(\phi_i) &= q(\phi_i, \phi_j)\alpha(\phi_i, \phi_j)\pi(\phi_i) \\ &= q(\phi_i, \phi_j)\frac{q(\phi_j, \phi_i)\pi(\phi_j)}{q(\phi_i, \phi_j)\pi(\phi_i)}\pi(\phi_i) \\ &= q(\phi_j, \phi_i)\pi(\phi_j) = q(\phi_j, \phi_i)\alpha(\phi_j, \phi_i)\pi(\phi_j) \\ &= K(\phi_j, \phi_i)\pi(\phi_j) \end{aligned}$$

if $q(\phi_i, \phi_j)\pi(\phi_i) < q(\phi_j, \phi_i)\pi(\phi_j)$. Here,

$$\alpha(\phi_i, \phi_j) = 1 \; and \; \alpha(\phi_j, \phi_i) = \frac{q(\phi_i, \phi_j)\pi(\phi_i)}{q(\phi_j, \phi_i)\pi(\phi_j)}$$

Therefore,

$$\begin{aligned} K(\phi_j, \phi_i)\pi(\phi_j) &= q(\phi_j, \phi_i)\alpha(\phi_j, \phi_i)\pi(\phi_j) \\ &= q(\phi_j, \phi_i)\frac{q(\phi_i, \phi_j)\pi(\phi_i)}{q(\phi_j, \phi_i)\pi(\phi_j)}\pi(\phi_j) \\ &= q(\phi_i, \phi_j)\pi(\phi_i) = q(\phi_i, \phi_j)\alpha(\phi_i, \phi_j)\pi(\phi_i) \\ &= K(\phi_i, \phi_j)\pi(\phi_i) \end{aligned}$$

In practical application, simulation of a draw from π using the Markov chain defined by the transition Kernel of Eq. 2.17 can be set up as follows: Given that the latest drawing has yielded the value x, the next value in the sequence is generated by

drawing a value y from a proposal distribution $q(y|x)$. The Markov chain then moves towards y with acceptance probability $\alpha(x, y)$ shown in Eq. (2.20). The algorithm of MH is shown below.

Algorithm 1 The MH algorithm.

Specify an initial value $x^{(0)}$
for $i = 1$ to N **do**
    Generate x^* from $q(x|x^{(i-1)})$
    Generate u from $\mathrm{U}(0, 1)$
    if $u \leq \alpha(x^*, x^{(i-1)})$ **then**
        $x^{(i)} = x^*$
    else
        $x^{(i)} = x^{(i-1)}$
    end if
end for
Discretize the space of x and compute distribution $P(X)$ according to its relative frequency
return P(X)

2.4.3.3 Gibbs sampling

Gibbs sampling which was originally discussed by *Geman and Geman* (1984) is another way of sampling the posterior probability. It is a special case of MH algorithm where the random value is always accepted ($\alpha = 1$) and the transition kernel is formed by the full conditional distributions.If we assume as before that the distribution of interest is $\pi(\Phi)$ where $\Phi = (\phi_1, \phi_2, \ldots, \phi_d)$. Each component ϕ_i can be a scalar, a vector, or a matrix. Consider that full conditional probability distributions $\pi_k(\phi_k) = \pi(\phi_k|\phi_{-k})$, $k = 1, 2, \ldots, d$ are available, which means that they are completely known and can be sampled. Therefore, the sampling starts with a initial value of $\Phi^{(0)}$ and condition each parameter on current values of the other $d-1$ parameters. Then sample from the resultant distributional form and repeat this operation on the other parameters in turn. This is easier to simulate than simulation from a complex joint distribution directly. Once the sample converges, all subsequent samples are from the target distribution. The algorithm of Gibbs sampling is shown

below. As the number of iterations increases, the chain approaches its equilibrium condition. Convergence is then assumed to hold approximately and the resulting value $\Phi^{(i)}$ is a draw from π

Algorithm 2 The Gibbs sampling algorithm.

1: Specify an initial value for the parameters $\Phi^{(0)} = (\phi_1^{(0)}, \phi_2^{(0)}, \phi_3^{(0)}, \ldots, \phi_d^{(0)})$
2: Initialize the iteration counter to $i = 1$
3: Obtain a new value $\Phi^{(i)} = (\phi_1^{(i)}, \phi_2^{(i)}, \ldots, \phi_d^{(i)})$ from $\Phi^{(i-1)}$ through successive generation of values

$$\begin{aligned}
\phi_1^{(i)} &\sim \pi(\phi_1|\phi_2^{(i-1)}, \phi_3^{(i-1)}, \phi_4^{(i-1)}, \ldots, \phi_d^{(i-1)}) \\
\phi_2^{(i)} &\sim \pi(\phi_2|\phi_1^{(i)}, \phi_3^{(i-1)}, \phi_4^{(i-1)}, \ldots, \phi_d^{(i-1)}) \\
\phi_3^{(i)} &\sim \pi(\phi_3|\phi_1^{(i)}, \phi_2^{(i)}, \phi_4^{(i-1)}, \ldots, \phi_d^{(i-1)}) \\
&\ldots \\
\phi_d^{(i)} &\sim \pi(\phi_d|\phi_1^{(i)}, \phi_2^{(i)}, \phi_3^{(i)}, \ldots, \phi_{d-1}^{(i)})
\end{aligned}$$

4: Increment i and repeat until convergence occurs

2.4.3.4 Estimating convergence

A key issue in the successful implementation of different MCMC algorithm is the number of runs until the chain approaches a stationary condition. This is also called the length of the burn-in period. Typically the first 1000 to 5000 elements are thrown out, and then various convergence tests are used to assess whether a stationary distribution has indeed been reached. However, a poor choice of starting values and proposal distribution can greatly increase the required burn-in time. One of areas that many current researchers focus on is whether an optimal starting point and proposal distribution can be found.

There are several suggestions in terms of successfully implementing an MCMC algorithm. One suggestion for a starting value is to start the chain as close to the center of the distribution as possible. A chain is said to be poorly mixing if it is in small region of the parameter space for long period of time, as opposed to a

well mixing chain that more broadly explores the space. A poorly mixing chain can arise when the target distribution is far from the proposal distribution or the target distribution have multiple peaks and the starting value is trapped close to one peak. To solve this, we can tune the proposal distribution to adjust the mixing, and in particular the acceptance probability of the chain. This is generally done by adjusting the proposal distribution: for example, by adjusting the variance or changing to a non-informative prior distribution (uniform distribution), or changing the degrees of freedom. To increase the acceptance probability, one decreases the variance of proposal distribution. However, *Gamerman and Lopes* (2006) note a trade-off: if the variance is too large, the moves are large, but are often not accepted. This leads to high autocorrelation and very poor mixing, requiring much longer chains. If the proposal variance is too small, the moves are generally accepted, but the change of each move is small, again generating high autocorrelations and poor mixing.

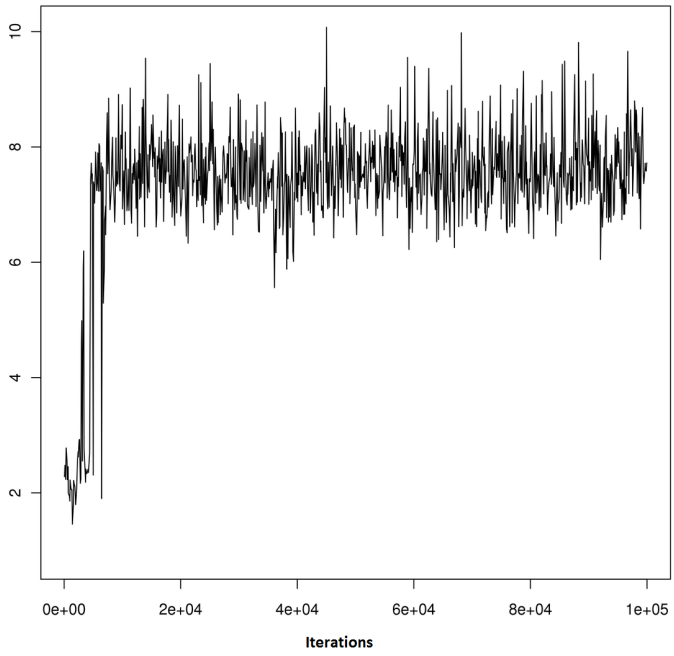

Figure 2.8: An example of trace plot of MCMC algorithm.

A good way to check the convergence is to plot the time series trace which is the value of certain random variable versus the number of iterations. Fig. 2.8 shows

example of trace plot without any burn-in period. It can be seen from figure that after about $1E4$ iterations, the sampling becomes generally stationary, therefore, the first $1E4$ iterations may be discarded as a burn-in period. Another way of convergence diagnostics is to plot the autocorrelation function versus time lag. If the random variable is from a stationary process, correlated draws still provide an unbiased picture of the distribution provided the sample size is sufficiently large. One strategy for reducing autocorrelation is thinning the output and storing only every mth point after the burn-in period. Several formal tests exist to estimate the convergence and details, and can be found in the book by *Geman and Geman* (1984).

2.5 Bayesian learning

Rather than update the model probability based on evidence in Bayesian inference, the purpose of Bayesian learning focuses on training the model parameters from data sets. Although, the focus of two tasks have some overlaps (e.g., the MCMC method could be both applied as inference or learning tools), Bayesian learning often refers to more complicated cases such as learning from incomplete data set or even learning the Bayesian network structure. Two popular learning approaches will be introduced in the following sections which mainly focus on how to handle incomplete data as well as data which contain uncertain measurements. The extension of dealing with soft evidence in Section 2.5.2.4 is contributed by the author.

2.5.1 The maximum likelihood approach

The maximum likelihood approach determines model parameters by maximizing the probability of observing the given data set.

Consider a simple Bayesian network example as shown in Fig. 2.1. A complete data set D^c is given below in Fig. 2.9(a). By assuming the cases are generated independently according to their true probabilities, an empirical probability of instantiation

Case	X	Y	Z
1	T	T	F
2	F	T	F
3	F	F	T
4	T	T	F
5	T	F	F

(a) Complete data set D^c

Case	X	Y	Z
1	T	?	T
2	F	T	?
3	?	F	T
4	T	?	F
5	F	?	?

(b) Incomplete data set D^i

Case	X	Y	P(Z=T)
1	T	T	50%
2	F	F	30%
3	F	T	40%
4	T	T	60%

(c) Complete data set with soft evidence D^s

Figure 2.9: Bayesian learning data sets.

of x, y, z can be defined in Eq. (2.21), which is simply the frequency of occurrence in the data set.

$$P(x, y, z|D^c) = \frac{D^c_{\#}(x, y, z)}{N} \tag{2.21}$$

where $D^c_{\#}(x, y, z)$ is the number of cases for the instantiation of x, y, z. A posterior distribution of z given the evidence of x and y is then shown below:

$$P(z|x, y) = \theta_{z|x,y} = \frac{D^c_{\#}(z)}{D^c_{\#}(x, y, z)} \tag{2.22}$$

According to the example above, the concept of maximum likelihood approach could be restated as follows:

Definition II.4. A complete data set D for variables X is a vector $d_1, d_2, \ldots, d_N$ where each d_i is called a case and represents a instantiation of variables X. The empirical distribution of event α happens could be calculated as:

$$P_D(\alpha) = \frac{D_{\#}(\alpha)}{N} \tag{2.23}$$

where $D_{\#}(\alpha)$ is the number of cases d_i in the data set D that satisfy event α. Also, the maximum likelihood estimates of conditional probability relations could then be written as:

$$\theta_{x|u}^{ml} = P_D(x|u) = \frac{D_{\#}(x,u)}{D_{\#}(u)}. \tag{2.24}$$

However, this maximum likelihood approach has its own drawback: when the data size is small, some events have not yet been observed, the maximum likelihood hypotheses assign zero to those events, which leads to a zero-count problem. For the example in Fig. 2.1 with data shown in Fig. 2.9(a), the $P(X = T|Z = T) = P(X = T \cup Z = T|Z = T) = 0/1 = 0$. Therefore, the maximum likelihood approach requires that the sample size should be big enough to have all possible outcomes, and it also does not take any prior information into account.

A Bayesian learning techniques will be introduced below and applied into our proposed SHM framework. The algorithm deals with this problem by incorporating prior knowledge into the estimation process. The method is based on Bayesian exact inference by assuming a conjugate prior and is further extended to integrate the data set with missing data and soft evidence as shown in Fig. 2.9(b) and (c) respectively.

2.5.2 Bayesian estimates using the EM algorithm

2.5.2.1 Dirichlet prior

Consider X is a node in Bayesian network with values $x_1, x_2, ...x_k$ and $\boldsymbol{U}$ is its parents. A parameter set for variable X and parent instantiation $\boldsymbol{u}$ can be denoted by $\theta_{X|\boldsymbol{u}}$, which is the set of network parameters $(\theta_{x_1|\boldsymbol{u}}, \theta_{x_2|\boldsymbol{u}}, ...\theta_{x_k|\boldsymbol{u}})$. The Dirichlet prior $p(\theta_{X|\boldsymbol{u}})$ can then be assumed which is specified by a set of exponents $\alpha_{x|\boldsymbol{u}}$ as shown in Eq. (2.25)

$$p(\theta_{X|\boldsymbol{u}}) = Dir(\alpha_{X|\boldsymbol{u}}) = \eta \prod_x [\theta_{x|\boldsymbol{u}}]^{\alpha_{x|\boldsymbol{u}}-1} \tag{2.25}$$

where η is a normalized factor

$$\eta = \frac{\Gamma(\sum_x \alpha_{x|\boldsymbol{u}})}{\prod_x \Gamma(\alpha_{x|\boldsymbol{u}})} \tag{2.26}$$

Here Γ is the Gamma function. It can be proven that the expected value of network parameter $\theta_{x|\boldsymbol{u}}$ is given by

$$E(\theta_{x|\boldsymbol{u}}) = \frac{\alpha_{x|\boldsymbol{u}}}{\alpha_{X|\boldsymbol{u}}}. \tag{2.27}$$

And the variance of this parameters is given by

$$Var(\theta_{x|\boldsymbol{u}}) = \frac{E(\theta_{x|\boldsymbol{u}})(1 - E(\theta_{x|\boldsymbol{u}}))}{\alpha_{X|\boldsymbol{u}} + 1}. \tag{2.28}$$

Finally, the mode of Dirichlet distribution is given in Eq. 2.29, which is the value having the largest density.

$$Mod(\theta_{x|\boldsymbol{u}}) = \frac{\alpha_{x|\boldsymbol{u}} - 1}{\alpha_{X|\boldsymbol{u}} - k} \tag{2.29}$$

where k is the number of states.

2.5.2.2 Bayesian estimates for complete data

The reason that we assume the Dirichlet prior is that the Dirichlet distribution is a conjugate prior for the multinomial distribution. This means that if the prior distribution of the multinomial parameters is Dirichlet, then the posterior distribution is also a Dirichlet distribution. The benefit of this is that the posterior distribution is easy to compute, and also, in some sense, it is possible to quantify how much our beliefs have changed after collecting the data.

Definition II.5. Let $(p_1, p_2, \ldots, p_k)$ be the vector of multinomial parameters (i.e. the probabilities for the different categories). If

$$(p_1, p_2, \ldots, p_k) \sim Dir(\alpha_1, \alpha_2, \ldots, \alpha_k)$$

which is the prior before collecting the data, then given observations $(x_1, x_2, \ldots, x_k)$

in the different categories, the posterior distribution can be described as:

$$(p_1, p_2, \ldots, p_k)|(x_1, x_2, \ldots, x_k) \sim Dir(\alpha_1 + x_1, \alpha_2 + x_2, \ldots, \alpha_k + x_k)$$
$$\propto \prod_x [\theta_x]^{\alpha_x + D^c_{\#}(x) - 1}$$

Although the choice of Dirichlet distribution according to conjugate prior may be unrelated to actual prior beliefs, it is still popular due to its flexibility and convenience to use.

The goal of Bayesian learning can be stated as to find parameter estimates that maximize the posterior distribution of $p(\theta_{X|\boldsymbol{u}}|D^c)$. A maximum a posteriori (MAP) estimate can be applied as shown in Eq. (2.30), which is derived from mode value of $\theta_{X|\boldsymbol{u}}$.

$$\theta^{MAP}_{x|\boldsymbol{u}} = \frac{\alpha_{x|\boldsymbol{u}} + D^c_{\#}(x\boldsymbol{u}) - 1}{\alpha_{X|\boldsymbol{u}} + D^c_{\#}(\boldsymbol{u}) - k} \tag{2.30}$$

Therefore, the smaller the number of sample size $\alpha_{x|\boldsymbol{u}}$ and the less confidence we have for the initial distribution of parameters. Consider the example of Fig. 2.1 with data set shown in Fig. 2.9(a), if the parameter set $\theta_{X|\overline{z}} = (\theta_{\overline{x}|\overline{z}}, \theta_{x|\overline{z}})$ with a prior density of $\rho(\theta_{X|\overline{z}})$ specified by the exponents:

$$\alpha_{x|\overline{z}} = 3 \quad and \quad \alpha_{\overline{x}|\overline{z}} = 5$$

Then the posterior density of $\rho(\theta_{X|\overline{z}}|D)$ is also Dirichlet with exponents is equal to

$$\alpha^{'}_{x|\overline{z}} = 3 + 3 = 6 \quad and \quad \alpha^{'}_{\overline{x}|\overline{z}} = 5 + 1 = 6$$

And the posterior expectation of parameters according to Eq. 2.27 which is also called the Bayesian estimate in the context of Dirichlet distributions are:

$$\theta^{BE}_{x|\overline{z}} = \frac{3+3}{6+6} = \frac{1}{2} \quad and \quad \theta^{BE}_{\overline{x}|\overline{z}} = \frac{5+1}{6+6}.$$

Moreover, according to the Eq. 2.30, the MAP estimate is:

$$\theta_{x|\overline{z}}^{MAP} = \frac{3+3-1}{6+6-2} = \frac{1}{2} \quad and \quad \theta_{\overline{x}|\overline{z}}^{MAP} = \frac{5+1-1}{6+6-2} = \frac{1}{2}.$$

Therefore, for this case, the expectation of parameter and MAP estimate of parameter are the same.

2.5.2.3 Expectation-maximization algorithm for incomplete data

However, sometimes SHM data might be missing due to unobservable parameters or downtime of the monitoring equipment, This creates an incomplete data set. When the data set D^i is incomplete as shown, in Fig. 2.1(b), an iterative expectation-maximization (EM) algorithm needs to be involved. The EM iteration is composed of a expectation step ("E" step), which creates a function for the expectation of the log-likelihood evaluated using the current estimate for the parameters, and a maximization step ("M" step), which computes parameters maximizing the expected log-likelihood found on the E step. These parameter-estimates are then used to determine the distribution of the latent variables in the next E step.

The goal here is to maximize the density $\rho(\theta|D)$, which could be expected as follows:

$$\rho(\theta|D) = \sum_{D^i} \rho(\theta|D, D^c) P(D^i|D). \tag{2.31}$$

Instead of optimizing this quantity which is often intractable, log likelihood function will often be optimized

$$E(\theta|D, \theta^{(t)}) = \sum_{D^c} [\log \rho(\theta|D, D^c)] P(D^c|D, \theta^{(t)}). \tag{2.32}$$

where θ^t are some initial estimates. The resulting estimates from this new optimization problem are then guaranteed to improve on the initial estimates, which is shown below:

Theorem II.4. If $\theta^{(t+1)} = \arg\max_{\theta}\{e(\theta|D, \theta^t)\}$, then $\rho(\theta^{(t+1)}|D) \leq \rho(\theta^{(t)}|D)$.

Under the Dirichlet prior assumption, it can be further proven that the θ for maximum expectation at $t+1$ step can be expressed by

$$\theta_{x|\boldsymbol{u}}^{(t+1)} = \frac{\alpha_{x|\boldsymbol{u}} + D_{\#}^{i}(x\boldsymbol{u}|\theta^{(t)}) - 1}{\alpha_{X|\boldsymbol{u}} + D_{\#}^{i}(\boldsymbol{u}|\theta^{(t)}) - k} \tag{2.33}$$

where $D_{\#}^{i}(\cdot\,|\theta^{t})$ is the expected counts given the parameter sets at t step. This can be expressed as:

$$D_{\#}^{i}(\cdot\,|\theta^{t}) = \sum_{D^{i}} P_{\theta^{t}}(.|d) \tag{2.34}$$

where d is one of data set. The calculation of Eq. (2.34) needs the inference of the network, which can be performed by the basic junction tree algorithm.

Again, for the example of Fig. 2.1 with data set shown in Fig. 2.9(b), we assume that we need to estimate the parameter $\theta_{x|z}$ using the maximum the likelihood estimates. After an initial assumption of conditional probability relations, the next iteration of $\theta_{x|z}^{(1)}$ could be calculated as follows:

$$\theta_{x|z}^{(1)} = \frac{\sum_{i=1}^{5} P_{\theta^{(0)}}(x, z|d_i)}{\sum_{i=1}^{5} P_{\theta^{(0)}}(z|d_i)}$$

where $P_{\theta^{(0)}}(\cdot\,|d_i)$ is the posterior distribution of data d_i based on initial estimates of $\theta^{(0)}$. This could be obtained by performing inference on the Bayesian network as introduced in previous sections. This process can be repeated until some convergence criterion is met. Notice that if too much data is missing, then the posterior distribution takes more iterations to converge or the converged posterior distribution might still spread widely on the domain. Also, some other search method could be applied for the EM algorithm to maximize the expectation of likelihood function, such as gradient based search or explicitly calculating the maximum point. The details can be found in *Darwiche* (2009).

2.5.2.4 Dealing with soft evidence

Soft evidence is the evidence that has a probability distribution which is another common situation for SHM data. This is often caused by an uncertain of observation or measurement uncertainty. Fig. 2.9(c) shows an example of uncertain data set where the observation of node C is uncertain. To incorporate these soft evidence, a Monte Carlo sampling method is applied to sample from the probability distribution of the soft evidence. The inference is performed independently for each sampled evidence and then the posterior distributions will be summed all together to calculate the expect counts in Eq. 2.34. The number of samples chosen will be according to the probability distribution of soft evidence as well as the assumed prior exponents. If the probability distribution is narrow or prior exponents are small, then a small number of samples will be sufficient to represent the distribution. If the distribution spreads widely or prior exponents are large, then relatively more samples will be necessary.

The EM algorithm considering both missing data as well as soft evidence is presented below. The proposed algorithm uses MAP estimates to maximize the likelihood function although other estimates such as Bayesian estimates can also be used. When the observed data sets are large enough, both estimates should produce similar results. The convergence criterion compares the parameters of $\theta^{(t)}_{X|\boldsymbol{u}}$ and $\theta^{(t-1)}_{X|\boldsymbol{u}}$. The iterative procedure stops until the change of parameters for the current iteration is negligible compared to the previous iteration.

Algorithm 3 MAP estimates using EM algorithm.

Specify the number of samples n for each soft evidence
Specify the exponents of Dirichlet prior for each state of node $\alpha_{X|\boldsymbol{u}}$
Specify the initial distribution of $\theta^{(0)}_{X|\boldsymbol{u}}$
$t = 0$
while $|\theta^{(t)}_{X|\boldsymbol{u}} - \theta^{(t-1)}_{X|\boldsymbol{u}}| \geq o$ **do**
    $c_{x\boldsymbol{u}} = 0$, $c_{\boldsymbol{u}} = 0$
    for $i = 1$ to D^i **do**
        for each instantiation $x\boldsymbol{u}$ **do**
            for $j = 1$ to n **do**
                Sample a evidence d from soft evidence
                $c_{x\boldsymbol{u}} = c_{x\boldsymbol{u}} + P_{\theta^{(t)}}(x\boldsymbol{u}|d)$
                $c_{\boldsymbol{u}} = c_{\boldsymbol{u}} + P_{\theta^{(t)}}(\boldsymbol{u}|d)$
            end for
        end for
    end for
    Update parameters $\theta^{(t+1)}_{x|\boldsymbol{u}} = (c_{x\boldsymbol{u}} + \alpha_{x|\boldsymbol{u}} - 1)/(c_u + \alpha_{X|\boldsymbol{u}} - k)$
    t=t+1
end while
return $\theta^{(t+1)}_{X|\boldsymbol{u}}$

CHAPTER III

LIFETIME WAVE LOAD UPDATING APPROACH

3.1 Introduction

Fatigue failures are a significant limit state for the structure of marine vessels. Large ocean-going vessels see on the order of 10^8 wave cycles during their service lives; this frequent cyclical loading, which is coupled with the corrosive ocean environment, makes fatigue failures a central maintenance concern for aging vessels. In calculating the fatigue limit state, the wave loading spectrum constitutes a major sources of uncertainty. Using on-board structural monitoring equipment to measure the fatigue load spectrum is frequently proposed as a way to reduce this uncertainty (*Mohanty et al.*, 2011; *Nielsen et al.*, 2011; *Sankararaman et al.*, 2011; *Rabiei and Modarres*, 2013a). However, as a result of a given ship's ability to change both trade routes and speed in response to global political and economic shifts, the lifetime wave loading on a ship is not statistically stationary; it may in fact vary significantly over short time scales. Monitoring can thus provide a snapshot of the fatigue life consumed, but using monitoring data to update design-stage predictions and future life forecasting is a more complex endeavor. This chapter introduces a novel updating approach, where spectral correction terms are determined by means of a series of statistically

stationary operational observations. A hierarchical Bayesian model is proposed for the integration of all of these observations into a model that is enable to capture dependence on vessel route and speed. This model is then integrated over an estimated future operational profile in order to provide an updated fatigue load spectrum for service life and repair forecasting.

3.2 Literature review

For large commercial and military vessels, considerable fatigue damage is caused by long-term wave induced VBM of the ship's hull girder (*Munse et al.*, 1982). Thus, at the design stage, engineers seek to approximate the loading spectrum of the VBM response. The "simplified method" (*Bai*, 2003) assumes the long-term stress range distribution at a ship structural element follows the Weibull distribution, this load history is often embedded into the life prediction formulas. Normally, either a regression approach or engineering judgement is needed in order to decide the Weibull scale and shape parameter. Such a distribution can be updated by SHM as previously proposed by *Okasha et al.* (2010a); *Zhu and Frangopol* (2013). However, this approach breaks the tie between the vessel's operational exposure and long-term fatigue loading. If the vessel changes its trade route, or its operating profile, the assumed future loading will not change with it because the load distribution does not include a dependence on these variables.

"Spectral based fatigue analysis" is a more advanced direct calculation method, but it has received less attention in the marine SHM community to date. In this method, the vessel's lifetime exposure at sea is divided into many small load cells (*Sikora*, 1983; *Sikora et al.*, 2002), each of which represents a specific environmental sea state, the ship's heading with respect to waves, and speed. The long-term load distribution is then built up by means of a series of short-term direct calculations within each load cell as well as the probability of the vessel operating in that cell.

In the spectral approach, it is necessary to determine the distribution of VBM within each specific cell in which a given vessel may operate. A range of approaches exist for these types of calculations, including direct non-linear simulation (*Wu and Moan*, 2006). Alternatively, there are also many simplified methods available that provides accurate and, efficient approximations of the bending moment with sufficient engineering accuracy. Most of these methods start from a linear system approach, within which a response amplitude operator (RAO) is used to transform an input wave spectrum into a bending moment response spectrum (*Jensen*, 2001). A semi-empirical RAO formed by means of the regression of a series of RAO model tests was used to represent all load cells. That RAO is obtained from a normalization of the magnitude, frequency, speed, and heading of several ships' sea trials data (*Sikora*, 1983; *Sikora et al.*, 2002). This RAO is then used to estimate the maximum wave induced moments acting on ships, as well as lifetime exceedence of the load spectrum. *Jensen and Mansour* (2002); *Jensen et al.* (2004) used a semi-analytical approach in order to derive the frequency response function for wave induced bending moments as well as ship motions for given load cell parameters. Although the linear RAO approach is known to underestimate extreme VBM responses, it is able to adapt quickly to different hull characteristics and operational profiles, thus providing a good approximation of the fatigue loading spectrum. An additional advantage of these linear methods is that they are able to provide a reasonable prior belief for structural model updating methods that may also be able to account for missing non-linearities. It is important to note, however, that these methods have only been used as early-stage design tools.

For all of these reasons, the accuracy of short-term, or cell-based fatigue damage calculation is a key issue in estimating accumulated fatigue life. While the conventional RAO approach assumes a normally-distributed stress response with narrow banded spectral shape (*Wirsching and Haugen*, 1974), it is known that both non-

linearities and wide-banded responses do in fact occur in certain conditions. The effect of bandwidth in fatigue damage using a simulated Gaussian process has also been studied by *Wirsching and Shehata* (1977). Rain-flow counting was used first to identify stress cycles and fatigue life was then calculated by the well-known Palmgren-Miner's rule (*Miner*, 1945). Later, *Dirlik* (1985) proposed an empirical solution for the rain-flow range density function that was based on extensive computer simulation. In an alternative formulation, based on the results of the Monte Carlo simulation, *Wirsching and Light* (1980) suggested a correction factor for the approximation of fatigue damage from the narrow band assumption. *Kim et al.* (2007) also provided a theoretical approximation to the cycle correction factor for a general wide-banded Gaussian process according to the *Rice* (1945) distribution.

In addition to the modeling of fatigue load by the Gaussian wide-banded process, researchers have also studied the contribution of non-Gaussian effects. *Lutes et al.* (1984) pointed out that the empirical correction factor could not be adequately described as a function only of the spectral widths, and therefore suggested considering the higher order approximation. Winterstein (1988; 2000) found that the first four moments are sufficient to capture a great deal of the non-Gaussian characteristics of the structural response. Hermite polynomials have been used to approximate the process by distribution moments. The effect of kurtosis on fatigue life was first studied only via Monte Carlo simulations, and it was shown that the mean damage accumulation rate increases as kurtosis increases. This was later confirmed with fatigue experiments of welded joints by *Sarkani et al.* (1994). *Yu et al.* (2004) discovered that skewness also plays a very important role in fatigue damage. The mean damage accumulation rate decreases as skewness increases. *Jensen and Mansour* (2002) considered the non-linearity for the skewness in his long-term wave induced load by using Hermite polynomials. Then *Wang and Sun* (2005) derived an analytical first-order approximation of the non-normality correction factor as a function of both kurtosis

and skewness for a narrow-banded process. The application of these studies includes the fatigue damage analysis of ship structures (*Wang*, 2010), mooring lines (*Gao and Moan*, 2007), and wind turbines (*Winterstein and Kashef*, 2000), etc. Nevertheless, the development of a general theoretical model for cumulative fatigue damage under wide-banded non-Gaussian processes has remained elusive. Despite a large number of numerical and experimental approaches that generally show good agreement with the measured data, estimation results are still potentially subject to large errors especially in severe sea conditions (*Hughes and Paik*, 2010).

As outlined in Chapter One, the application of artificial intelligence techniques has therefore been studied in order to better understand fatigue loading from monitoring data. This data may include environmental conditions, structural responses or ship operation records. However, most current approaches do not address the issue of long-term fatigue loading spectra under different operational conditions, (e.g., changes in a ship's trade route environment, or mission). In what follows, we seek to generalize these approaches so that such considerations can be included when updating loading models as part of a wider SHM system. In the proposed method, a ship's lifetime experience is first divided into many load cells, where each cell corresponds to a unique combination of sea state, vessel heading relative to waves, vessel speed, and vessel condition. Jensen's (2002; 2004) analytical approach and non-linear contributions of VBM are applied as prior predictions of wave load for each cell. Lifetime loading profiles are then constructed by means of the probabilistic integration of those individual cells. Using an SHM system in order to sense the ship's VBM response and current environmental conditions, a cell-based updating strategy is also presented. A group of three updating parameters are selected so as to capture the impact of ship speed on the experienced loads, wave height on the skewness of load distribution, and the bandwidth of the loading process. Using the MCMC method, distributions for these parameters are found for observed cells. In order to predict

these parameters in unobserved cells, hierarchical Bayesian models are used to establish mapping relations between uncertainty factors and their influencing parameters in operational profile. These models are then trained via the data from those observed load cells. Different models and learning approaches are explored to compare the updated factors in unobserved cells. This leads to a refined prediction of lifetime loading. After the hierarchical Bayesian models are trained, it is then possible to integrate the cell-based loading responses across any future operational profile and obtain an updated prediction of future fatigue loading for the vessel.

An overview of the proposed two-level lifetime load updating framework will be given in Section 3. This will be followed by a cell-based updating approach in Section 4, as well as a lifetime load updating approach in Section 5. Both updating approaches employ the Bayesian methods that were introduced in Chapter Two. Two examples of the approach are given in Section 6. The first example is a validation of the proposed framework with a known model, while the second example uses high fidelity simulation results as SHM data to update lifetime load.

3.3 A proposed lifetime load updating framework

The proposed lifetime load updating procedure is shown in Fig. 3.1. This framework is based on existing spectral fatigue methods, such as those proposed by *Sikora et al.* (2002) and *Jensen and Mansour* (2002), which are summarized below. In these approaches, the ship's lifetime exposure at sea can be divided into many blocks or cells (*Sikora et al.*, 2002), with each cell corresponding to an "operational mode" defined by sea state (SS), which itself consists of a significant wave height and wave period; the vessel's speed (U); and heading angle relative to wave (β). The size of cell should be small enough that a statistical stationary condition can be assumed within each cell. In each cell, the probability of the VBM exceeding a given value is calculated by a suitable seakeeping prediction method, such as *Jensen and Mansour* (2002), and

expressed as $G(m|SS, \beta, U)$. With the response in each cell known, lifetime VBM exceedence probability can be determined by the proper weighting of every stationary cell exceedence probability that the vessel is likely to experience. This is shown in Eq. 3.1 where W is the normalized weighting function related to the ship's exposure in each cell.

$$F(m) = \iiint G(m|SS, \beta, U)W(SS, \beta, U)dSSd\beta dU \tag{3.1}$$

Extending this spectral loading method for updating via in-service monitoring, we assume that a subset of the operational cells that a vessel is likely to encounter has been observed. We also assume that monitoring data is available for load cell 1 to load cell n (denoted by a solid circle in Fig. 3.1), while load cell k does not have any observed data available and load response needs to be predicted (denoted by a dashed circle). An engineering load prediction model based on spectral method that is normally used during the design stage has been chosen as shown inside the first solid rectangle. This engineering model is expected to be controlled by several parameters $\mathbf{\Theta}_i = (\theta_1, \theta_2, \theta_3, \cdots), i = 1, 2, 3, \ldots n$. A direct estimation of response distribution using the design stage engineering model leads to a prior prediction that may not match the in-service observation. This difference can be mostly described as mean shift, as well as change of variance and shape of a distribution that can be captured by updating the cell-based parameters $\mathbf{\Theta}_i$. Because $\mathbf{\Theta}_i$ is updated within each cell, it is dependent for each cell. However, since the underlying loading process is continuous in the cell variables (SS, U, β), a relationship is expected to exist between those variables and the cell-based parameters $\mathbf{\Theta}_i$. Therefore, a hierarchical Bayesian model is further developed to train the relations between operational mode parameters and its corresponding $\mathbf{\Theta}_i$. With the trained relations in the hierarchical Bayesian model, the updated $\mathbf{\Theta}_k$ in those unobserved load cells can be further obtained, while the initial design loading estimate is taken into account as prior information. As long as those unobserved cells are refined based on SHM data, the cell information can be

integrated into lifetime load prediction according to Eq. 3.1. If the vessel's operational profile changes, it is still possible to forecast future fatigue load spectra using all of the load updating performed to date by simply changing the $W(SS, \beta, U)$ term in Eq. 3.1. Therefore, compared with the "simplified method" discussed in the literature review, the proposed method allows model updates to be re-used, even if a given vessel's operational conditions have significantly changed.

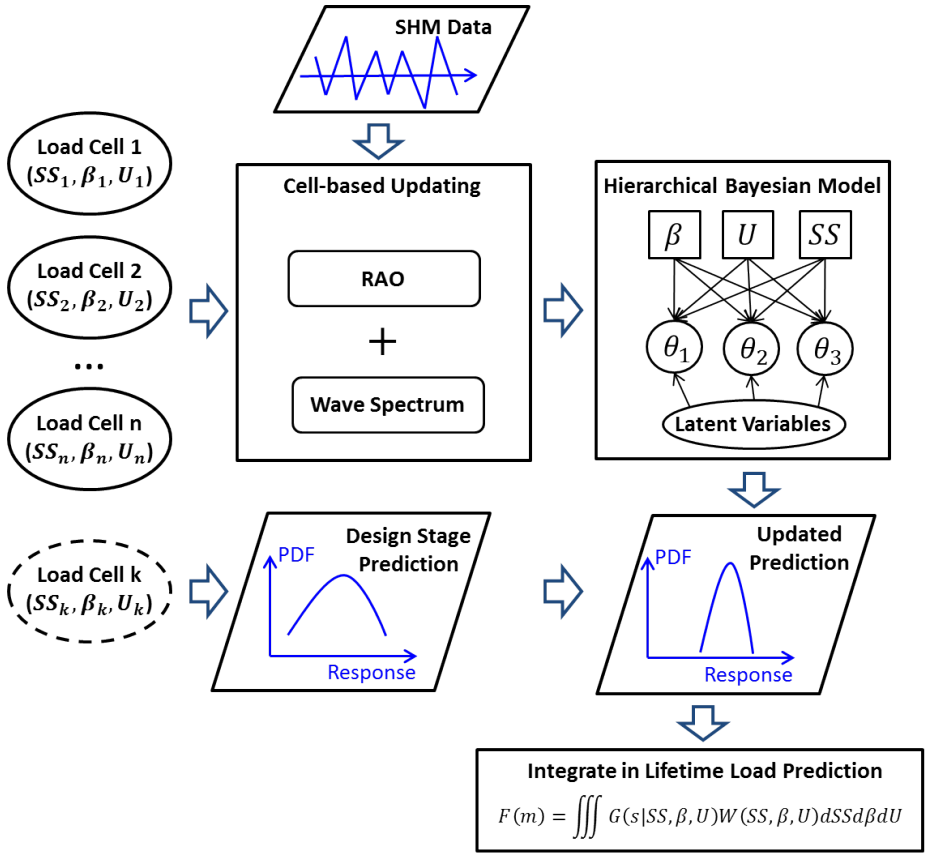

Figure 3.1: A proposed lifetime load updating procedure.

3.4 Cell-based load updating strategy

3.4.1 Design stage prediction of vertical bending moment

Jensen's (2002; 2004) closed form expression for the frequency response function of vertical wave induced bending moment Φ_M has been used as an engineering model

for calculating RAO as shown in Fig. 3.1. The expression is derived analytically by using linear strip theory from a box shaped vessel, while the small contribution of hydrodynamic damping is neglected. The expression is as follows:

$$\frac{\Phi_M}{\rho g B_0 L^2} = \kappa \frac{1-kT}{(k_e L)^2}[1-\cos(\frac{k_e L}{2}) - \frac{k_e L}{4}\sin(\frac{k_e L}{2})]F_v(Fn)F_c(C_b)\sqrt[3]{|\cos\beta|} \quad (3.2)$$

where B_0 is the maximum waterline breadth, L is the length of box, T is the draught, C_b is the block coefficient, $k = \frac{2\pi}{\lambda}$ is the wave number, λ is the wave length, ω is the wave frequency, β is the heading angle with 180° as corresponds to head sea. The Smith correction factor is approximated by

$$\kappa \approx \exp(-k_e T) \quad (3.3)$$

where k_e is the effective wave number.

$$k_e = |k\cos\beta| \quad (3.4)$$

The correction factor for the block coefficient F_c has the expression shown in Eq. (3.5)

$$\begin{aligned} F_c(C_b) &= [(1-\vartheta)^2 + 0.6\alpha(2-\vartheta)] \\ \vartheta &= 2.5(1-C_b),\ C_b = \max(0.6, C_b) \end{aligned} \quad (3.5)$$

and the speed correction factor is given in Eq. (3.6).

$$F_v(Fn) = 1 + 3Fn^2,\ Fn < 0.3 \quad (3.6)$$

An ITTC recommended modified Pierson-Moskowitz family is used here with an input of significant wave height H_s and average wave period T_0. The response of wave induced VBM can be calculated as Eq. (3.7).

$$S_{VBM}(\omega) = S_{wave}(\omega) \times \Phi_M^2 \quad (3.7)$$

The non-Gaussian characteristics of the response will also be considered following

the approach of *Jensen and Mansour* (2002), since such non-linearities are common for the vessel structures under the wave loads. Various non-Gaussian models have been formulated through series transformation; these models use non-Gaussian statistical moments (skewness and kurtosis) to represent the non-Gaussian contribution of a Gaussian process, often by using Hermite series (*Winterstein*, 1988; *Winterstein and Kashef*, 2000). A comprehensive study of the effect of skewness and kurtosis by varying the speed, heading, and wave can be found in Mansour and Wasson (1995). Jensen's non-Gaussian behavior for the sagging moment will be studied here only by considering skewness μ_3, since kurtosis has a less significant impact on the moment (*Jensen and Mansour*, 2002). Consider a wave induced bending moment as random variable, which is assumed as

$$M = \epsilon_0 + \epsilon_1 U + \epsilon_2 U^2 \tag{3.8}$$

where U is a standard normal process that is denoted as a parent variable. A quadratic term has been added in Eq. (3.8) that can preserve the first three statistical moments of M and reflect the skewness of the data. By equating these statistical moments equal to 0, standard deviation s and skewness μ_3 respectively, Eq. (3.8) can be solved as shown below:

$$\begin{cases} \epsilon_0 = -\eta s \\ \epsilon_1 = \sqrt{1-\eta^2}s \\ \epsilon_2 = \eta s \end{cases} \tag{3.9}$$

where η can be solved by

$$4\eta^3 - 6\eta + \mu_3 = 0 \tag{3.10}$$

Newton's method can be applied to solve Eq. (3.10) iteratively. This equation only holds for sagging $\mu_3 > 0$, which ensures a monotonic variation between M and U.

For a broad-banded Gaussian process, the cumulative distribution function (CDF)

of response peak x is given by *Ochi* (1990) in Eq. (3.11).

$$F_p(x) = \Phi(\frac{u}{\tau}) - \sqrt{1-\tau^2}\exp(-\frac{1}{2}u^2)(1-\Phi(-\frac{\sqrt{1-\tau^2}}{\tau}u)) \tag{3.11}$$

where $u = x/\sqrt{m_0}$ is the normalized response with a mean of zero and a standard deviation of one. τ is the bandwidth which is defined by

$$\tau = \sqrt{1 - \frac{m_2^2}{m_0 m_4}} \tag{3.12}$$

where m_i is the ith spectral moment. This formulation is for a broad-banded Gaussian process. When $\tau = 0$, it becomes a narrow-banded case, which is a Rayleigh distribution; when $\tau = 1$, it becomes an extreme broad-banded case, which is a normal distribution.

For a slightly non-Gaussian narrow-banded process ($\tau = 0$), u can be substituted by solving for Eq. (3.8). However, for a slightly broad-banded distribution (which is the most common case), a certain amount of error will be involved if τ is still calculated from the spectral moments with non-Gaussian skewness. A correction factor of χ has been introduced as shown in Eq. (3.13).

$$\tau' = \chi\tau \tag{3.13}$$

To find the original bandwidth τ under the Gaussian process, a fast Fourier transform (FFT) technique is applied to transform the $S_U(\omega)$ to an auto-correlation function $R_{uu}(\tau)$ for U in Eq. (3.8). Then, the auto-correlation function of $R_{MM}(\tau)$ can be found by using Eq. (3.14) which can be further converted to $S_M(\omega)$ by inverse fast Fourier transform (IFFT).

$$R_{MM}(\tau) = (\mu_3\eta)^2 R_{UU}(\tau=0)^2 + 2(\mu_3\eta)^2 R_{UU}(\tau)^2 + \mu_3^2(1-2\eta^2)R_{UU}(\tau) \tag{3.14}$$

3.4.2 Cell-based updating via MCMC

According to the framework above, three parameters $\mathbf{\Theta} = (k, \mu_3, \chi)$ are specified which will be explained below. Those parameters represent the uncertainties in the engineering model that cause differences between the prior prediction and the real time measurements.

1. A scaling factor k for the speed correction term F_v in Eq. (3.6). This represents error related to the impact of ship speeds on experienced load. This factor could change the magnitude of response peak by changing the response spectrum. However, the peak distribution shape will not be changed. The modified speed correction terms then becomes $F_v(Fn) = k(1 + 3Fn^2)$.

2. A skewness factor μ_3. This measures error in relation to the impact of wave height on the skewness of the load distribution, which is the non-Gaussian behavior of the response. Skewness is a measure of symmetry; thus for a Gaussian process, μ_3 will equal zero. Change of skewness for the sagging moment will change the shape of peak distribution, especially the probability of a large peak occurring region. Although a deterministic skewness value can directly be obtained from the time domain SHM data as long as the length of the monitoring time is sufficient, it is still considered an uncertainty factor. The distribution of skewness may still influence prediction results.

3. A bandwidth correction factor χ. This factor measures the error related to the bandwidth of the loading process, which is an adjustment of bandwidth calculated from the Gaussian process. Therefore, the updated bandwidth τ' only represents a variable that can be applied into the Gaussian process peak distribution. It is thus neglects the inherent physics of a broad-banded non-Gaussian process, since the analytical solution is generally unknown. Nevertheless, for an engineering model, this facilitates a quick approximation of response peak

distribution during the design stage by applying the knowledge of Gaussian process.

According to the model above, a design stage prediction model for response load can be expressed in Eq. (3.15) with a prediction error term ε:

$$F_p(x) = g(x|k, \mu_3, \chi) + \varepsilon \tag{3.15}$$

Assume that initial prior distribution of parameters is obtained that denotes $f_0(k, \mu_3, \chi)$ and ε satisfies a normal distribution with mean 0 and standard deviation σ_ε. With the collected SHM data for the corresponding load cell, the posterior distribution of $f(k, \mu_3, \chi|D)$ can be obtained via a standard MCMC method. The predictive distribution of response can be further computed via the integral through each parameter

$$F_p(x|D) = \int_{\Theta=(k,\mu_3,\chi)} f(k, \mu_3, \chi|D) g(x|k, \mu_3, \chi) \mathrm{d}\Theta \tag{3.16}$$

3.5 Lifetime load updating using hierarchical Bayesian model

The goal of lifetime load updating is to predict unobserved load cells by learning knowledge from observed ones. According to Eq. (3.15), the VBM distribution in each cell is characterized by three hyperparameters: k, μ_3 and χ. Therefore, if the same hyperparameters in unobserved cells can be obtained, it is possible to predict VBM distribution. A hierarchical Bayesian model is built as shown in Fig. 3.1 to link the distributions of hyperparameters between the observed and unobserved cells. Two cases will be discussed below: one assumes empirical knowledge is available; the other assumes that no empirical knowledge is available.

Since much research (*Wirsching and Shehata*, 1977; *Yu et al.*, 2004; *Jensen and Mansour*, 2002; *Wang and Sun*, 2005) has been done to characterize relations be-

tween hyperparameters and operational profiles, these relations can potentially be applied with updated factors trained from SHM data. Therefore, for the first case, we can assume that there is an empirical equation (EE) h available for the estimation of hyperparameters in each cell which is a function of U_i, $\cos(\beta_i)$ and SS_i, The corresponding Bayesian model can then be written as:

$$\boldsymbol{\Theta}_i = h(\boldsymbol{L}, U_i, \cos(\beta_i), SS_i) + \varepsilon \tag{3.17}$$

where $\boldsymbol{L} = (l_1, l_2, l_3, \cdots)$ is the latent variable that is assumed to be unchanged among different cells and ε is the error term used to measure the bias between empirical prediction and observed evidence. A monotonic function h is recommended, as it is relatively easier to learn latent variables from data.

For the second case, there is no empirical knowledge that can be applied, so a simple linear response surface (LRS) can be constructed as shown in Eq. (3.18)

$$\boldsymbol{\Theta}_i = l_1 U_i + l_2 \cos(\beta_i) + l_3 SS_i + \varepsilon \tag{3.18}$$

In order to predict the hyperparameters for all of the load cells, the distributions of those latent variables must first be obtained. Three methods are compared for their ability to find the latent variables: the linear regression (LR) method, the MCMC algorithm, and the EM algorithm. Since the input hyperparameters are treated as probability distributions, special modifications have been implemented for the three methods so as to incorporate probabilistic inputs. For the LR approach, the LRS model is built on each cumulative probability level ranging from 0 to 1 with interval of 0.1. Therefore, the predictive distributions of hyperparameters need to be reconstructed in terms of this series of probability levels. For the MCMC algorithm, a "potential class" (*Lauritzen et al.*, 1990) is added so as to incorporate "soft evidence" and the joint probability can be re-written as

$$p(\boldsymbol{\Theta}_i, \boldsymbol{L}) \propto \gamma(\boldsymbol{\Theta}_i) p(\boldsymbol{\Theta}_i | \boldsymbol{L}) p(\boldsymbol{L}) \tag{3.19}$$

where $\gamma(\boldsymbol{\Theta}_i)$ is the potential factor which is each sample's corresponding probability level from the SHM data. For the EM algorithm, Algorithm Three in Chapter Two uses n number of deterministic values sampled from the "soft evidence" and the posterior distribution for each sample is then added.

Each of these three methods have its advantages and disadvantages. The LR method is simple and robust, but it does not reflect any physical relations and may lead to large error when few load cells are observed. The MCMC approach is able to deal with continuous space directly as well as a non-linear function; however, it is prone to convergence issues. The EM algorithm is based on the exact inference method, which is more robust and efficient; however, discretization is needed for all continuous nodes.

3.6 Example

To evaluate the proposed updating framework, the JHSS vessel (*Okasha et al.*, 2010a) has been studied with operational profiles divided into 60 load cells. The ship's main particulars are listed in Table 3.1. The probability of occurrence for each load cell is assumed as shown in Table 3.2 according to the operational profiles from Sikora's paper (2002) and a scatter diagram of the north Atlantic sea. For example one, the VBM monitoring data is generated from Jensen's method with known skewness and other parameters. This example is intended to validate the performance of the framework. For example two, the VBM data is simulated by using Large Amplitude Motion Program (LAMP) software (*Lin et al.*, 2008), which is considered to be more accurate, especially when non-linear response becomes significant. However, since the skewness and other parameters are not direct inputs from LAMP, the prediction accuracy of lifetime VBM peak distribution can be compared between the proposed framework and the LAMP simulation.

The errors between the two distributions are compared using earth mover's distance

(EMD). The EMD is a method that allows for the evaluation of the dissimilarity between two multi-dimensional distributions by finding the least expensive transportation cost. The details of this method can be found in Rubner's paper (*Rubner et al.*, 2000).

Length overall	294.06 m
Length between perpendiculars	290 m
Beam	31.99 m
Draft	7.74 m
Block coefficient	0.484

Table 3.1: Main particulars of JHSS.

Sea State	Speed (knots)	Heading Angle 0°	45°	90°	135°	180°
SS=5 ($H_s = 3.26m$, $T_z = 8.5s$)	15	3.56E-2	7.13E-2	7.13E-2	7.13E-2	3.56E-2
	20	2.06E-02	4.15E-02	4.15E-02	4.15E-02	2.06E-02
	30	4.11E-02	8.29E-02	8.29E-02	8.29E-02	4.11E-02
	40	1.13E-02	2.17E-02	2.17E-02	2.17E-02	1.13E-02
SS=7 ($H_s = 7.5m$, $T_z = 10.5s$)	15	8.93E-03	9.87E-03	3.23E-03	6.35E-03	3.88E-03
	20	6.82E-03	1.69E-02	1.78E-03	6.76E-03	4.00E-03
	30	6.82E-03	1.69E-02	3.56E-03	6.76E-03	4.00E-03
	40	8.23E-04	2.23E-03	2.23E-03	2.23E-03	3.53E-03
SS=8 ($H_s = 11.5m$, $T_z = 11.5s$)	15	7.77E-04	9.85E-03	0.00E+00	3.89E-04	0.00E+00
	20	0.00E+00	5.96E-04	0.00E+00	5.18E-05	3.24E-04
	30	0.00E+00	5.96E-04	0.00E+00	5.18E-05	3.24E-04
	40	0.00E+00	0.00E+00	0.00E+00	0.00E+00	0.00E+00

Table 3.2: Probability of occurrence for different load cells under the north Atlantic sea.

3.6.1 Validation against known parameters

A validation is performed with all time domain VBM data generated from known parameters. The inference is then performed for both cell-based updating and lifetime load updating in order to determine whether it can recover those parameters from the data.

The time domain VBM data is simulated using Jensen's method to represent our

monitoring data. The skewness and scaling factor are assumed initially for each load cell according to Eq. (3.20) and Eq. (3.21) respectively:

$$\mu_3 \cong aH_s(1 - exp(\frac{-bFn}{|\cos\beta|})) \tag{3.20}$$

$$k \cong 1 \tag{3.21}$$

where a and b for Eq. (3.20) are 0.08 and 10, respectively, according to the recommendation of *Jensen and Mansour* (2002). Examples of simulated time domain VBM data for low skewness cell and high skewness cells are compared in Fig. 3.2, while sagging peak points are selected to plot the CDF.

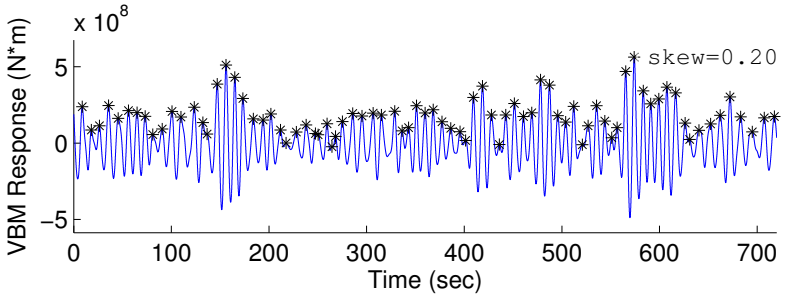

(a) Low skewness cell: sea state 5, heading angle 180°, speed 15 knots

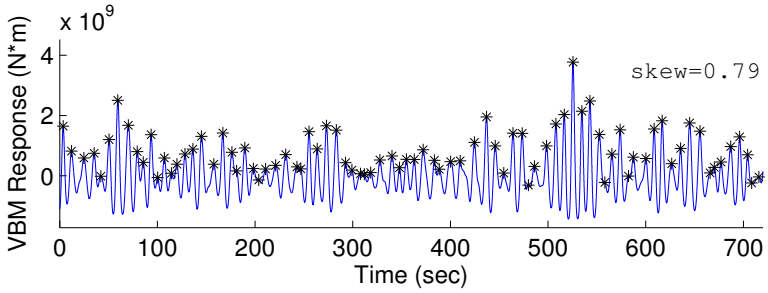

(b) High skewness cell: sea state 8, heading angle 180°, speed 20 knots

Figure 3.2: Simulated time domain VBM data.

Two types of validations are performed. The first determines whether the MCMC method is able to find the assumed hyperparameters and predict the VBM from posterior distribution in the cell-based updating. The second determines whether the hyperparameters in unobserved load cells can be successfully predicted as well

as whether prediction accuracy is expected to be improved by using a lifetime load updating strategy.

3.6.1.1 Validation for cell-based updating

A cell-based updating strategy is performed for all of the load cells in order to find the posterior distribution of k, μ_3 and χ. Fig. 3.3 and Fig. 3.4 provide examples of posterior distribution for those hyperparameters as well as peak CDF prediction for the cells shown in Fig. 3.2.

From the results, it can be seen that the MCMC algorithm finds the posterior distributions of k and μ_3 around their true values, although a small deviation is observed for k of high skewness case. Also by using those posterior distributions, both cases predicts the original simulated data very well compared with Jensen's method, since Jensen's method assumes distribution as narrow-banded, while the cell-based prediction considers bandwidth effect.

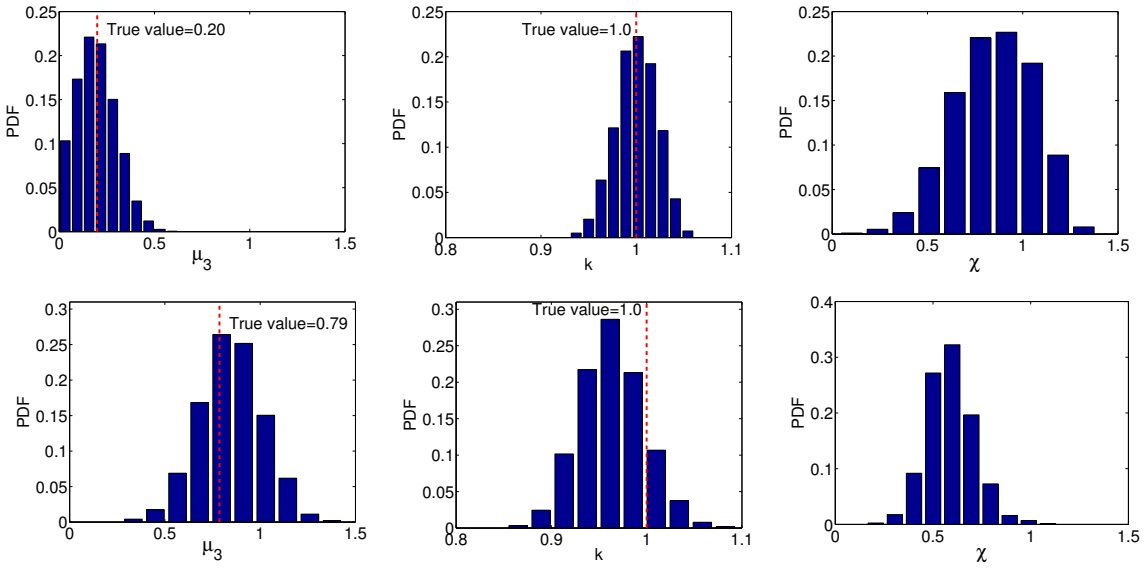

Figure 3.3: Posterior distribution for hyperparameters using cell-based updating (upper: low skewness cell, bottom: high skewness cell).

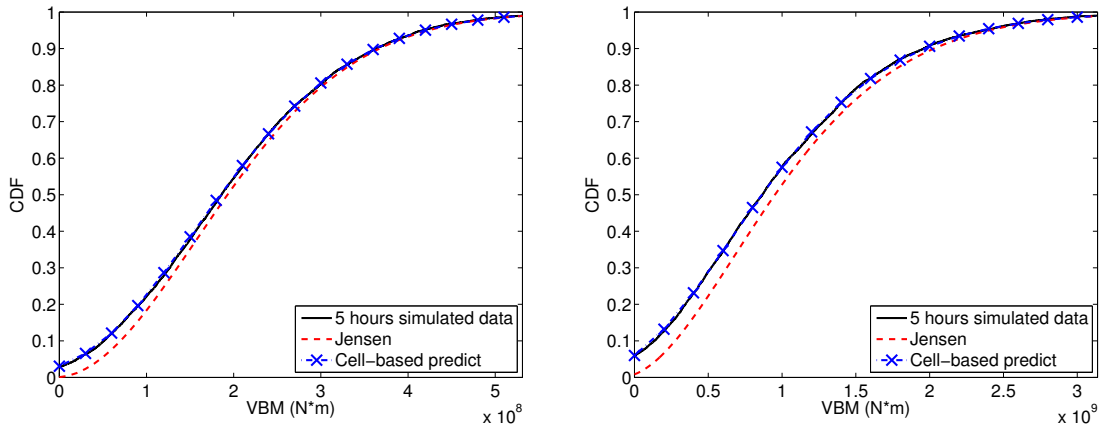

Figure 3.4: Cell-based peak CDF prediction (left: low skewness cell, right: high skewness cell).

3.6.2 Validation for lifetime load updating

The observed load cells are then sampled according to their probability of occurrence as shown in Table 3.2. The posterior distribution of parameters is further extracted from those observed load cells to build a hierarchical Bayesian method that is composed of a selected model (an LRS-based model and an EE-based model) with a selected learning approach (LR, MCMC and EM) as illustrated above. However, certain combinations may not be available (e.g. χ does not have an EE-based model). These are designated as "not run" in the table. A full list of hierarchical Bayesian method cases is shown in Table 3.3.

μ_3	LRS, LR	LRS, MCMC	EE, MCMC	EE, EM
k	LRS, LR	LRS, MCMC	EE, MCMC	–
χ	LRS, LR	LRS, MCMC	–	–

Table 3.3: Hierarchical Bayesian method cases.

The results are validated in terms of two aspects. First, for all EE-based models, since the μ_3 and k are generated according to Eq. 3.20 and Eq. 3.21, respectively, those latent variable distributions can be compared with the initial assumptions to

determine whether they are consistent. Second, the error in the predictive distribution of hyperparameters should decrease with each increase in observed cells.

Fig. 3.5 and Fig. 3.6 compare the posterior distributions of those latent variables using an EE-based model with a different number of observations. Fig. 3.5 uses the MCMC method for both μ_3 and k. It can be seen that with increased observation of cells, the latent variables become narrower and have a mean value close to true value. Although, a small deviation in mean value can be seen for the ε_{μ_3} and ε_k under 84% of observations which implies a possible over-fit when too many observation is used. Similarly, the results in Fig. 3.5 show the posterior distribution of latent variables using the EM approach for only μ_3 with uniform prior. When there are not enough cells observed, the posterior distributions are still flat and close to uniform distribution. However, prediction improves by increasing the number of observations, even though a deviation can also be seen for b_{μ_3}.

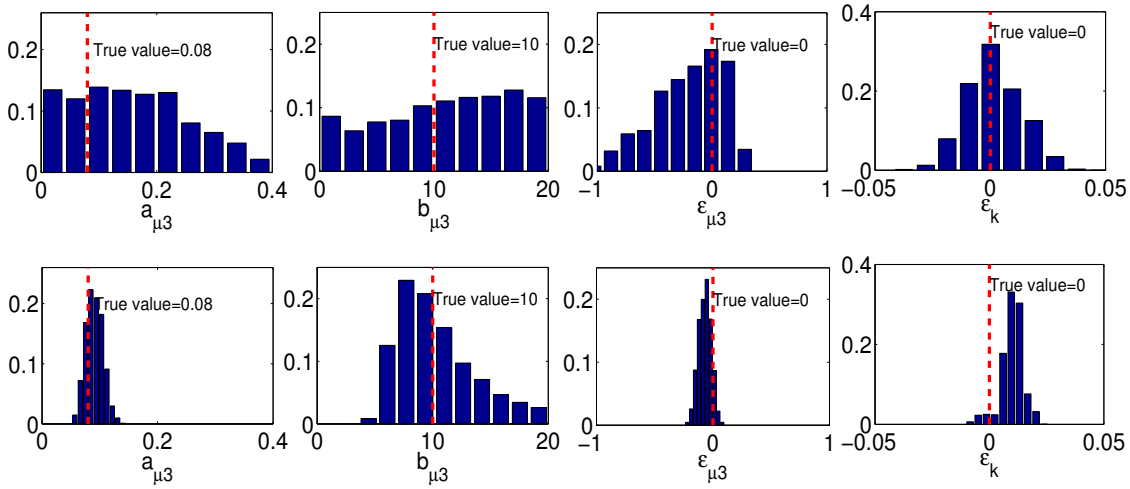

Figure 3.5: The posterior distribution of latent variables for μ_3 and k using MCMC algorithm (upper: 14% observed cells, bottom: 84% observed cells).

The EMD error for all those hyperparameters using different methods is then compared in Fig. 3.7. To achieve a consistent comparison, all load cells are re-predicted regardless of whether or not they are observed. Generally, the error for all those

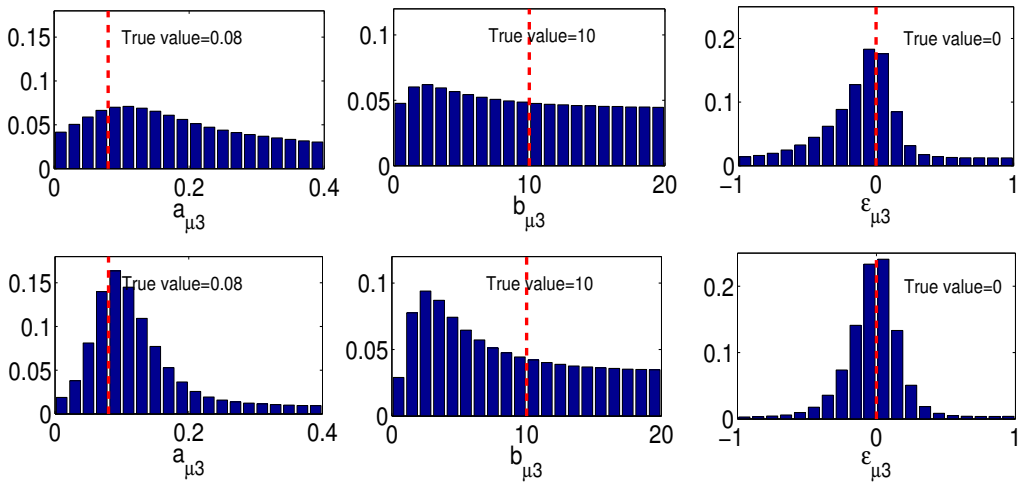

Figure 3.6: The posterior distribution of latent variables for μ_3 and k using EM algorithm (upper: 14% observed cells, bottom: 84% observed cells).

methods decreases when the number of observed cells increases, although a larger error is seen when using the LRS-based model with MCMC algorithm when a small percentage of cells is observed. This also shows that the deviation of latent variables from the EE-based model has less of an impact on the prediction of hyperparameters. Moreover, the prediction accuracy for all EE-based models is quite stable compared to the LRS-based model, even when only 14% of cells are observed. This is, however, under the assumption that data is simulated from the prediction model. The ability to gather data from a high fidelity numerical simulation is presented in the next section.

3.6.3 Load updating using LAMP simulation data

VBM data simulated from LAMP is further used here. For each load cell the LAMP simulates about three hours of data; this data is then filtered by a low pass filter to remove noise. Again, peak points have been selected to plot the VBM's CDF. The observed load cells are sampled in Table 3.2. The initial study found that Jensen's VBM prediction has a larger margin for error in the following sea conditions than in

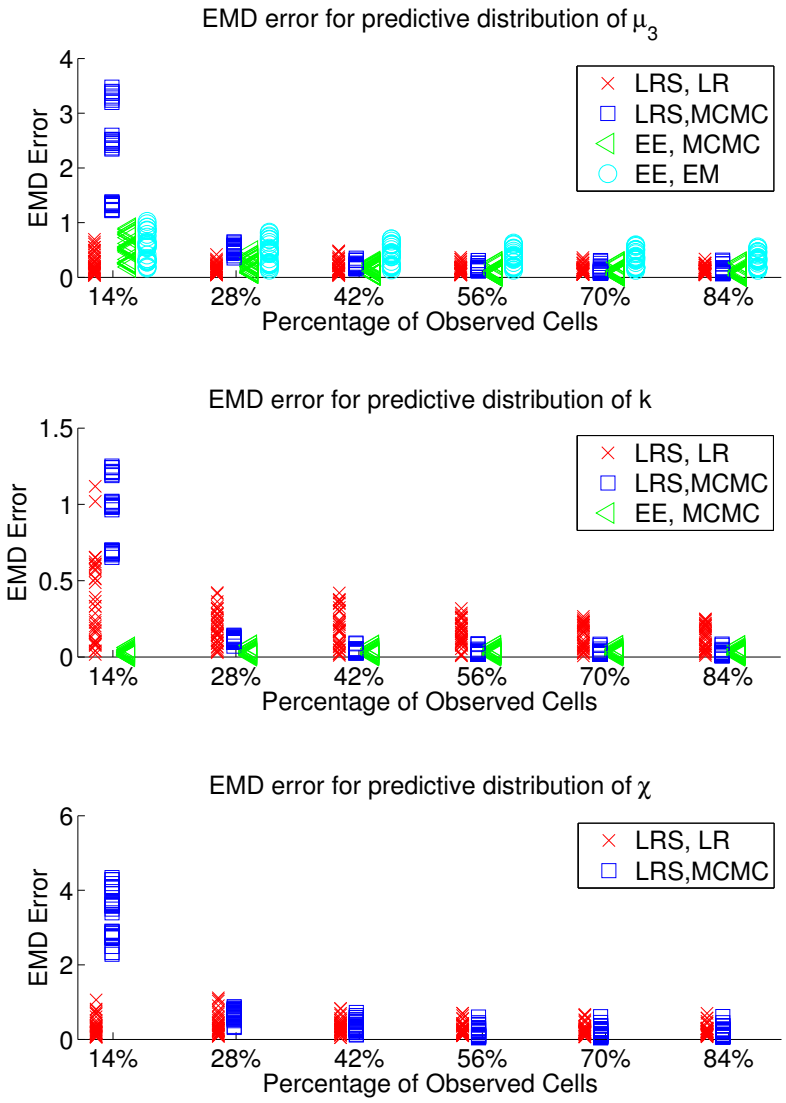

Figure 3.7: EMD error for predictive distribution of μ_3 (upper), k (middle) and χ (bottom) for each load cell.

the head sea conditions. Therefore, the surrogate model has been built separately for the following sea and head sea conditions. Four prediction cases are run and each case relies on the predictive distribution of three hyperparameters from the surrogate model as shown in Table 3.4.

	Case I	Case II	Case III	Case IV
μ_3	LRS, LR	LRS, MCMC	EE, MCMC	EE, EM
k	LRS, LR	LRS, MCMC	EE, MCMC	LRS, MCMC
χ	LRS, LR	LRS, MCMC	LRS, MCMC	LRS, MCMC

Table 3.4: VBM prediction cases.

The EMD error for each load cell has also been plotted in terms of number of observations as shown in Fig. 3.8. It can be seen that when above 42% of the load cells are observed, case II, case III, and case IV have less error for each load cell as compared to Jensen's method, while in case I, our method starts to outperform Jensen's method when around 70% of cells are observed. When there are not enough observations, the prediction by EE-based model (e.g., case III) is generally better than that of the LRS-based model (e.g., cases I, and II). The EE-based model may help to avoid such unreasonable predictions. However, when the number of observations is sufficient, prediction from the LRS-based model becomes more accurate. This may be because the EE-based model is less flexible in accommodating different observation cases when compared to the LRS-based model.

By applying Table 3.2, the lifetime VBM peak CDF prediction can be calculated as shown in Fig. 3.9. Again, the lifetime VBM peak distribution always uses re-predicted results from each load cell regardless of whether or not they are observed. Generally, it can be seen that with an increase in the number of observed cells, the lifetime VBM prediction improves by using a surrogate model approach for all four cases when compared to Jensen's prediction. When 28% of cells are observed, case II, case III and case IV perform similarly and are more accurate than case I. When 84% of cells are observed, case III predicts slightly better than the other cases; this

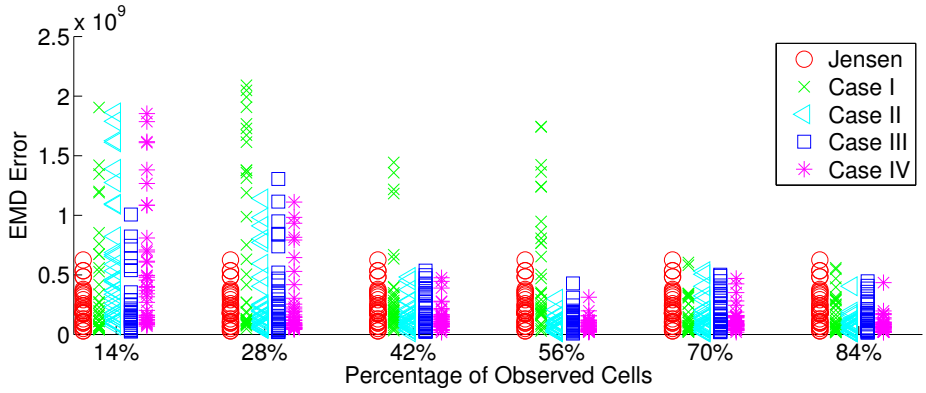

Figure 3.8: The EMD error for peak CDF prediction for each load cell.

result is different from the results of cell-based updating. This implies that the EE-based method may be more accurate in predicting load cells with a high probability of occurrence or in generally low sea state and low speed cases.

3.7 Conclusions

This chapter proposed a framework for using observed wave load monitoring data for the purpose of load updating. This framework is composed of a two-level updating strategy: cell-based updating to characterize every load cell by three hyperparameters and a surrogate model to predict hyperparameters in those unobserved cells, as well as peak cumulative distribution function. Three Bayesian learning approaches were applied: a continuous based Markov chain Monte Carlo method, discrete based methods and a simple linear regression method. All of these methods must be extended specifically to accommodate the probabilistic input data. Two models were used: an empirical equation-based model when empirical knowledge is available, and a linear response surface model when empirical knowledge is not available.

Validation was performed first by using simulated data with assumed parameters. The posterior distribution of parameters was therefore able to be compared with true

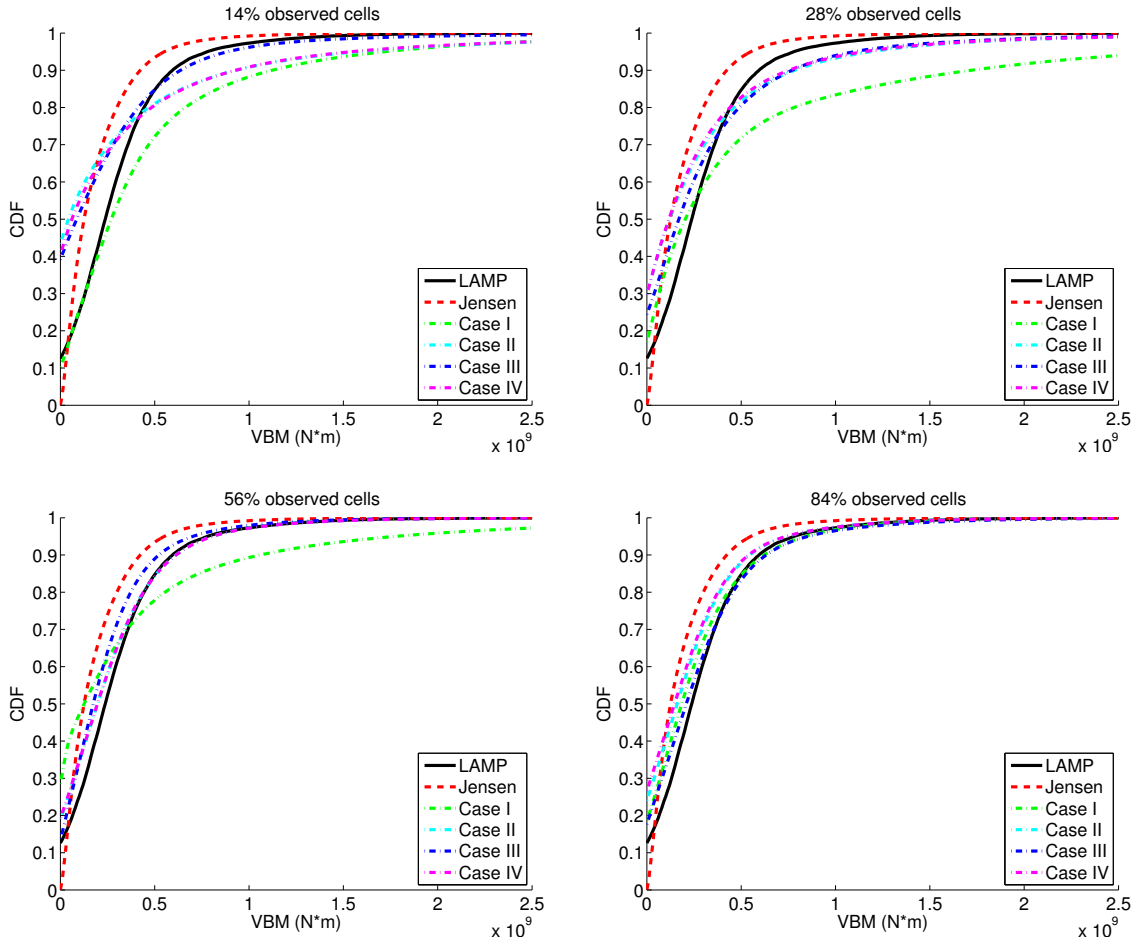

Figure 3.9: Lifetime VBM peak CDF prediction with different observed cells.

values. The results show that when observation is not sufficient enough, the empirical equation based model performs better than the linear response surface model, because it is helpful in avoiding certain unreasonable predictions. However, when the number of observations becomes sufficient, the situation is changed, since the empirical equation-based model loses some of its flexibility to accommodate different cases. This framework is further applied by using high fidelity LAMP simulation results as structural health monitoring data. The lifetime wave load is predicted in terms of different percentage of observed cells. The results prove that with increased number of observations, the accuracy of vertical bending moment peak distribution improves, as well as that when around 42% of the data is observed, the proposed methods are able to generate predictions better than Jensen's initial prediction. Moreover, although the empirical equation based model has an "over-fit" issue when a large amount of data is observed, it still predicts vertical bending moment distribution more accurately, implying better accuracy in cells with a high probability of occurrence.

CHAPTER IV

LIFE-CYCLE FATIGUE MANAGEMENT USING BAYESIAN UPDATING

4.1 Introduction

Structural fatigue cracking in lightweight high-speed vessel structures is a central maintenance and life-cycle cost concern. The crack typically appears at welds or discontinuities of structural details of service where the stress concentration is significant. It is typically caused by a fluctuating stress which can initiate microscopic cracks. Those microcracks could remain invisible and take a considerable amount of time to become observed, which is called an initiation period. Once the crack is observable, it undergoes a propagation period, which for ship structures is usually a small percentage of the total life. Fatigue failure typically caused by an unstable crack propagation where the rupture may happen. Though other failure modes are possible, failure by fatigue is progressive, irreversible cracking process, which unless detected and remedied, can lead to a catastrophic situation. However, although researchers have spent a significant effort studying fatigue in the past fifty years, the exact mechanism of a fatigue failure is complex and is not completely understood thus far.

In order to avoid potentially catastrophic situations, various models have been

proposed to relate the cyclic stress strain state at the notch or crack tip to the fatigue strength of the structural component. According to the different application purposes, fatigue methods for marine structure could be generally grouped into two categories. The first one is called the safe life fatigue design approach, which is based on experimental measurement of fatigue in terms of cycles to failure for different loading levels and specimen geometries. The second is called the fracture mechanics approach, which is based on an assumed initial crack size and predicting the subsequent crack propagation life under cyclic load. The design fatigue approach normally has been applied to the design stage estimation for the structure's fatigue life, while the fracture mechanics approach is mostly used for fitness-for-service (FFS) or engineering critical assessment (ECA) of remaining life of in-service structure. However, all the methods struggle to make accurate mid-life prediction of future fatigue performance and associated structural risks.

On the other side, in recent years, an increasing number of vessels have installed an extensive data monitoring system to collect vessels' performance and environmental records. This data could not only provide navigational assistance, but also potential structural integrity management support. Since the fatigue life prediction heavily relies on the past load history records, using SHM information to refine the prediction and support inspection planning and decision making becomes an attractive direction.

This "fatigue integrity management" framework will be presented after a literature review is first presented in Section 4.2. Two statistical models are proposed according to different purpose: one is based on the design S-N fatigue approach (Section 4.3) and the other one is based on fracture mechanics approach which is often used as FFS assessment (Section 4.4). Both models are able to incorporate not only the SHM data, but also design prior knowledge to reflect the knowledge from design codes and experimental testing programs. The updated models are expected to lead to a more accurate life prediction as well as a decision making support for repair

and maintenance needs. Finally, the suitability and accuracy of using this model for reliability ECA will be discussed since low failure probability events need to be accurately tracked. In Section 4.5, a novel discretization scheme has been developed specifically for the purposes of reliability prediction and performing inference from in-service structural measurements, and is one of the key academic contributions of this thesis. Through applications of two crack growth example problems, the algorithm is shown to be a robust and accurate structural reliability tool.

4.2 Literature review

Vessels' aging is a complex process of corrosion and crack growth which is influenced by many factors. The marine industry recognised that predicted structural loads and their effects during the design stage are subject to uncertainties. The life-cycle problem considered here fundamentally attempts to diagnose the as-built fatigue properties of the vessel in order to support inspection, repair, and life-extension decisions in a cost-effective and risk-acceptable manner for the vessel owner.

In spite of various crack detection and condition monitoring technology having been developed (*Yamamoto et al.*, 2007; *Wang et al.*, 2010; *Méndez and Csipkes*, 2013), much effort is still required to interpret the data. A consistent treatment of all available information is required to assess the existing structure, and show that the safety and risk assessment leads to acceptable levels of risk. *Moan et al.* (2004) established a reliability-based procedure for assessment of deteriorating ship structures by accounting for the interaction between fatigue and corrosion under different environmental conditions. *Garbatov and Guedes Soares* (2009) built a time-variant probabilistic model for maintenance and repair analysis of tanker deck plates due to corrosion. A joint industry project (JIP) MONITAS has also been performed in the offshore industry (*Hanson et al.*, 2010; *Takaoka et al.*, 2010; *Hosti et al.*, 2010). The idea is to monitor loads and structural stresses of FPSO to provide data for predict-

ing the remaining life of cracks. This project will also develop an advisory intelligent monitoring system. Reliability-based decision making software such as Rightship (www.rightship.com), VDST (*Lo Nigro et al.*, 2005) or DNV's hull integrity management (*Goksyr*, 2009) are also available. The vessel condition is assessed according to the collected information including class reports, inspection records, ship information, etc. This data helps owners and operators keep their ships' hull fit for purpose through continuous control of the hull condition, which reduce the maintenance costs and create business advantage.

Among those studies, Bayesian analysis has received high interests (*Jensen and Mansour*, 1994; *Ditlevsen and Madsen*, 1996). Most applications are based on simple Bayesian updating techniques, however, researchers have also proposed a more complicated Bayesian Network approach, which uses a network representation to express more complex dependence structures between components of the problem. The Bayesian network approach is easier to capture multiple uncertainties as well as loading amplitude. Those works can be found in *Friis-Hansen* (2000); *Mahadevan et al.* (2001); *Straub* (2009); *Straub and Kiureghian* (2010a); *Bensi et al.* (2013).

A key challenge in applying Bayesian networks to structural reliability modeling is the need to discretize continuous random variables for prediction and inference tasks. Such discretization schemes significantly impact both accuracy and computational cost of the model. Some schemes have already been developed for inference of a hybrid Bayesian Network containing both continuous and discrete nodes (*Chang and Chen*, 2005; *Cheng and Druzdzel*, 2000; *Gogate and Dechter*, 2005; *Langseth et al.*, 2009; *Neil et al.*, 2007), however, these approaches only work over a limited number of distribution and data types. For example, *Chang and Chen* (2005) developed a new efficient inference, which is referred to as the decision-tree based inference algorithm for hybrid dynamic Bayesian network (HDBN). The basic idea of this inference algorithm is to separate the nodes into four different types. The likelihood

table are precomputed by forward sampling in the topological order of the nodes in the network. The evidence space is partitioned into hyper-cubes based on the sampling data. Further, the posterior distribution of target nodes based on given evidence is inferred by separately considering the dynamic transitional nodes and static transitional nodes. This scheme shows some potential for inferring a general hybrid Bayesian network; however, the sampling technique it uses can affect the prediction accuracy, especially for reliability purposed modeling. *Neil et al.* (2007) developed a dynamic discretization scheme which iteratively splits intervals according to their relative entropy error until they converge. This approach allows for accurate approximations of marginal posterior distributions, however, if DBN inference is used to perform the time series based reliability analysis, the nodes at the same level in every time step will share the same discretization intervals. Additionally, node-by-node entropy tracking is less attractive for the DBN, because splitting and merging operations on a single node can impact the prediction accuracy at other time steps. One special type of hybrid Bayesian network is the conditional linear Gaussian (CLG) model (*Larsen and Marx*, 2012), where the exact computation of means and variances is available; however, the CLG can only manage cases where all variables satisfy a normal distribution. Stochastic sampling methods, such as the MCMC, are another potential option for inference of Bayesian networks (*Gamerman and Lopes*, 2006; *Beck and Au*, 2002). The advantage of using a sampling method is that it can be applied to a wide range of models and is easy to implement. Although the model always converges when given an infinite number of samples, the convergence rate is relatively poor, especially for a large model or large data sets. Also, a reasonable estimation of prior distribution needs to be provided, otherwise these methods can struggle with ill-convergence. For a reliability-based inference task, the accuracy of sampling a small "tail probability region" can also be an issue. Therefore, both hybrid and stochastic sampling algorithms presented have shortcomings for evidence-based

reliability updating inference.

4.3 Stress life (S-N) approach

4.3.1 Overview of stress life approach

In the traditional fatigue life prediction, stress life or S-N approach has been commonly applied for marine structures. The life or number of stress cycles of a certain material is determined by applying constant or variable amplitude load and recording the number of cycles to failure via experimental testing. Then, the magnitude of a cycles versus the logarithmic scale of cycles to failure is plotted as shown in Fig. 4.1. In reality, fatigue life data normally exhibits widely scattered results because of inherent microstructural inhomogeneity in the materials properties, surface finish, or environmental condition. Therefore, a design S-N curve is often constructed, which characterizes the minimum fatigue life at a given fatigue strength level so that the majority of the fatigue data fall above minimum. Fig. 4.1 shows a schematic representation of the design S-N curve. The choice of that design S-N curve is according to international standards and one common way to do this is to use a lower two sigma, or even three sigma design curve in which the curve can be derived by shifting the median S-N curve in logarithm coordinates to the left by two or three times the sample standard deviation. Certain materials, primarily body-centered cubic (BCC) steels, have an endurance or fatigue limit S_e below which the fatigue life is "infinite" in certain environments. For the linear portion of the S-N curve, the equation of the S-N line can be expressed as

$$N = \frac{A}{\Delta\sigma^m} \quad or \quad log(N) = log(A) - mlog(\Delta\sigma) \tag{4.1}$$

where N is number of cycles to failure, A and m are the material constants, and $\Delta\sigma$ is stress range.

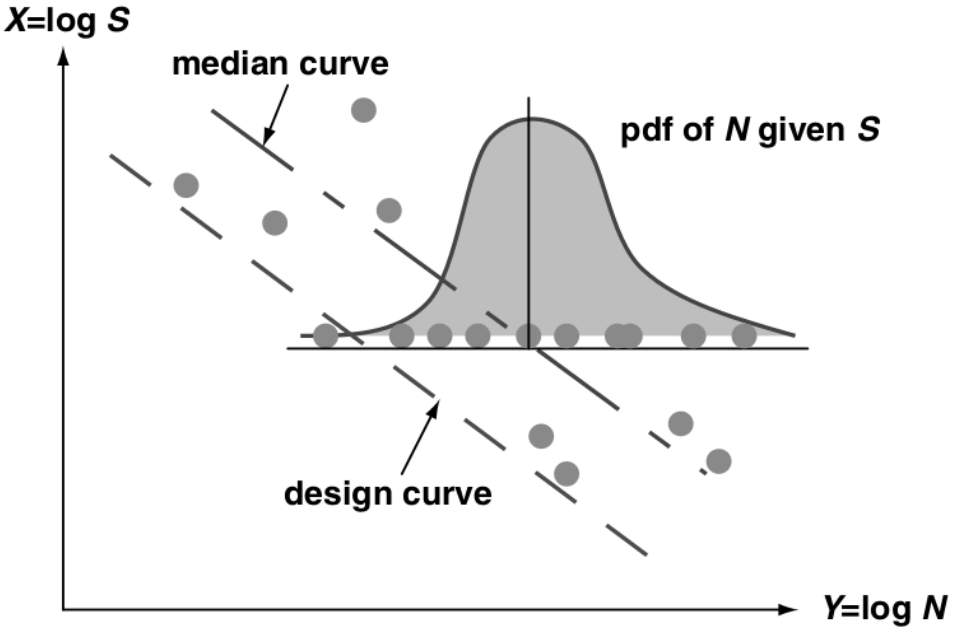

Figure 4.1: Typical S-N curve showing mean and design lines (*Lee et al.*, 2004).

The fatigue behaviour discussed above has dealt with constant amplitude loading. In contrast, most service loading history has a variable amplitude, which means loading varies in amplitude cycle-to-cycle. To calculate the damage under this type of loading, cumulative damage rules have been developed to deal with variable amplitude loading using the baseline data generated from constant amplitude tests. Among them, the Palmgren-Miner's rule has been widely employed, which was first proposed by *Palmgren* (1924) and was further developed by *Miner* (1945). The terminology of damage fraction D_i is defined first, which can be expressed as

$$D_i = \frac{n_i}{N_i} \tag{4.2}$$

where n_i is the number of cycles experienced at stress level S_i and N_i is the fatigue life in cycles at stress level S_i. Therefore, the damage fraction D_i is defined as the fraction of life used up by an event or a series of events. For example, the damage fraction due to one cycle of loading is $1/N$. In other words, the application of one cycle of loading consumes $1/N$ of the fatigue life. Then failure in any of the cumulative damage

theories is assumed to occur when the summation of damage fractions is equal to or is larger than one. The failure criterion for variable amplitude loading can now be stated as

$$D = \sum_{i=1}^{k} \frac{n_i}{N - i} \geq 1 \tag{4.3}$$

When applying the stress life approach to ship structural details, different types of stress analysis and corresponding S-N curves have to be chosen:

- **Nominal stress** A far-field stress in the component calculated by finite element models or simple methods like beam theory based on applied loads and the sectional properties of the component. The stress is calculated on the basis of the net cross section of a specimen without taking into account the effect of geometric discontinuities. The experimental S-N curved is developed to relate the number of cycles to the stress range. Therefore, when using these S-N curves the calculated stresses should correspond to the nominal stress used in creating these curves. Typically, one S-N curve corresponds to one component.

- **Hot-spot stress** A local stress at the hot spot where cracks may be initiated. Hot spot stress considers the influence of structural discontinuities due to the geometry of the connection but excludes the stress concentration effects of welds themselves. This approach has been widely applied to calculate the fatigue of weld connection. A fine-mesh finite element (FE) analysis is often involved to extrapolate the stress at the weld toe according to the stress gradient. This extrapolation is sensitive to the element sizes used in the finite element model and the modeling technique.

- **Notch stress** is the peak stress at the root of a weld or notch taking into account stress concentration due to the effects of structural geometry as well as the presence of welds. The fatigue notch factor relates the unnotched fatigue strength of a member to its notched fatigue strength at a given life. This allows

a single S-N curve to be used for all welded joints in the same environment. However, a considerable amount of uncertainty around each of these parameters still exists, which make the application of the notch stress approach difficult in practical applications.

4.3.2 Fatigue management based on stress life approach

Since fatigue life prediction is subject to significant uncertainty, a probabilistic fatigue approach is often preferred by many researchers, which incorporates different sources of uncertainties into the life calculation. The results could not only provide the predicted life distribution, but also update the life based on received data. Although classic reliability based fatigue approaches (such as FORM/SORM (*Ditlevsen and Madsen*, 1996)) have been well-developed so far that are capable of model updating as well as inspection scheduling, those methods are not flexible enough to quantify different uncertainties nor easy to be applied as SIM tool.

The proposed method for this section is mainly from the work presented in (*Zhu and Collette*, 2011). The method uses local fatigue approaches, which can collapse the fatigue lives of different structural details onto a common S-N curve. The service experience with the vessel is treated as an ongoing fatigue experiment which determines the as-built fatigue properties of the vessel. A Bayesian updating approach has been proposed to interpret the service life experience with the vessel and estimate the fatigue properties. It differs from the traditional reliability based fatigue approaches by adding more flexibility to the model representation as well as incorporating uncertainty. Therefore, the proposed method uses terminology of "fatigue management", since it overcomes the shortcomings of traditional reliability based fatigue approaches. As the method is based on stress life approach, each crack is only judged by a pass-fail metric that determines if a crack presents. A more accurate fracture mechanics based fatigue management approach will be presented in the next

section, which characterizes the actual crack growth.

The method is based on the limit state function proposed by *Souza and Ayyub* (2000) for reliability based fatigue design approach. The function is expressed as:

$$N_I = \frac{D_{cr} A}{k_f^m \Delta\sigma^m} \tag{4.4}$$

where D_{cr} is the Palmgren-Miner damage summation, typically taken as 1.0, k_f is a stress range uncertainty factor, A and m are S-N curve constants, and N_I is the number of loading cycles expected during the life of a structural detail. When multiple structural details need to be considered, hot-spot stress or more recently, notch stress approaches are often used which take advantage of the ability of finite element analysis to model stresses near the crack-generating notches of weld toes and weld roots in the detail by using fictitious notch radii. These methods can consider local detail geometry and generally give more accurate results than the nominal stress methods while only a single set of S-N coefficients A and m can be used for a wide variety of details. Therefore, these methods greatly reduce the number of coefficients that must be found to model the as-built properties of the ship.

For observing an as-built vessel, a stochastic description of the fatigue process is needed in place of a design-stage fixed-value idealization so that inspection results can be interpreted as probabilistic samples. In this work, a lognormal stochastic model is proposed, where each of the variables A, D_{cr}, and k_f in Eq. 4.4 are assumed to follow the lognormal distribution with location parameters λ and scale parameters ζ (*Collette*, 2011). Indicating the corresponding lognormal parameters with subscripts, under the assumption that the distribution for A, D_{cr}, and k_f are uncorrelated, the distribution of life to crack initiation, N_I, will also follow a lognormal distribution with parameters:

$$\begin{aligned} \lambda_I &= \lambda_{D_{cr}} + \lambda_A - m(\lambda_{k_f} + \ln \Delta\sigma) \\ \zeta_I &= \sqrt{\zeta_{D_{cr}}^2 + \zeta_A^2 + (m\zeta_{k_f})^2} \end{aligned} \tag{4.5}$$

4.3.2.1 Description of updating methods

The proposed updating approach assumes that there is a single, unknown set of three lognormal distributions for A, D_{cr}, and k_f that represent the actual as-built quality of the structural details in the vessel. The method seeks an alternative parametrization of fatigue life based on these three parameters. By calculating the corresponding local notch stress by a suitable local fatigue approach, the distribution of expected life of each detail can be found by Eq. 4.5. The vessel is inspected in-service, and the presence or absence of a crack at each detail in each inspection can be viewed as a sample of the corresponding life distribution for each detail. Thus an efficient method is required to go backwards from observations of the outcome of Eq. 4.5 for each detail to the vessel-wide underlying distribution of A, D_{cr} and k_f.

The method assumes that there are three primary sources of uncertainty in the fatigue life prediction problem: uncertainty in the loading applied to the fatigue details, uncertainty in lognormal parameters for the fatigue parameters A, D_{cr}, and k_f, and finally, the stochastic uncertainty of what amount of cycles the detail will actually fail once the distributions of A, D_{cr}, and k_f are known. The proposed updating approach for life-cycle predictions adopted here focuses on the second source of uncertainty, as the uncertainty in these parameters is fundamentally epistemic uncertainty in these parameters. If sufficient budget was available for testing during design and construction, these sources of uncertainty could be effectively removed. The first source of uncertainty in the applied loading is a mix of epistemic and stochastic uncertainty, including errors in the hydrodynamic model of the vessel as well as the fundamental stochastic nature of the ocean environment. It will not be considered further in this section. The third source is viewed as stochastic uncertainty and therefore non-reducible as well.

4.3.2.2 The MCMC model

An MCMC approach is applied with two variants in model, which attempt to estimate the distribution of initiation life as a function of applied stress only without tracing all the way back to the underlying distributions of A, D_{cr}, and k_f. Such approach allows future fatigue cracking to be predicted, however, it does not allow specific assessment of errors in the components of the S-N fatigue model.

PyMC (*Patil A, Huard D*, 2010) is a Python language module that implements a suite of MCMC algorithms as Python classes, and is extremely flexible and applicable to a large suite of problems. PyMC was used in this work to compute the MCMC models required for the logit and probit regression equations which will be introduced later on. In PyMC, a DAG graph is used to specify the parameters estimated by MCMC. For both logit and probit regression, the same DAG architecture can be used, as shown in Fig. 4.2. At the top of Fig. 4.2 are the two parameters which govern the regression-details provided in the next section. For these two parameters, the priors are assumed to have a normal distribution. P_{cr} is a logit or probit node, depending on the type of regression used, expressing the probability that a crack should have occurred at a given detail at a given time, and the crack is a binominal node indicating whether or not a crack has occurred. The rectangular nodes denotes the data that is input into the model, consisting of the applied external stress range, the number of elapsed cycles at the current inspection interval, and a vector of true/false inspection results indicating whether or not a crack was detected at each detail.

A number of sites are chosen to be inspected, all of which are assumed to share the same underlying fatigue parameters. Since additional cracks tend to occur as the number of applied cycles increases, the model tends to become more accurate as inspections are carried out later in the vessel's life. To speed up the MCMC process, the initial values of parameters for a given inspection are seeded with the results of previous inspections.

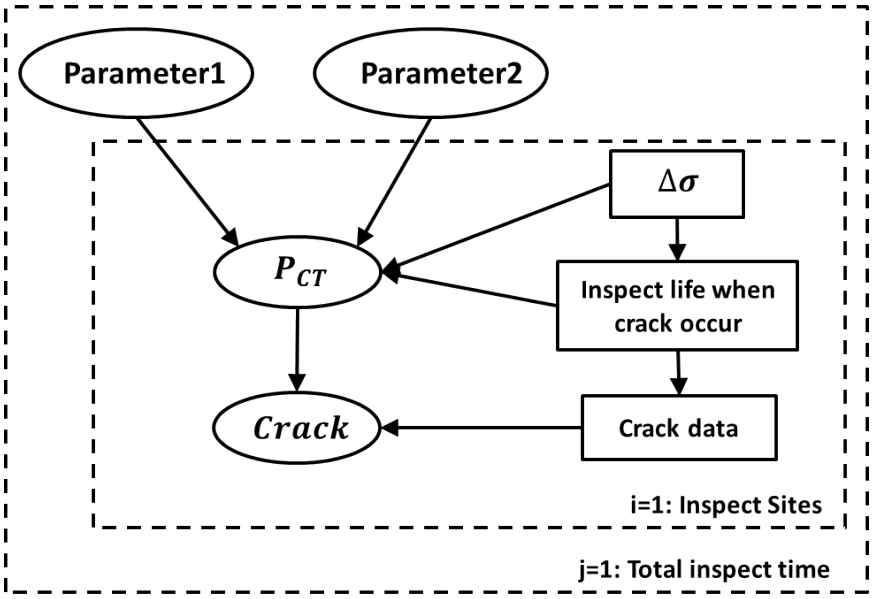

Figure 4.2: DAG used for logit and probit regression.

4.3.2.3 Logit regression

Logistic regression or logit is an aproach to learn function of the form f: $X \rightarrow Y$ or $P(Y|X)$ in the case where Y is discrete-valued and $X = (X_1, X_2, \ldots, X_n)$ is any vector containing discrete or continuous variables. The discussion of logit regression in this section is based on the methodology presented in *Albert and Chib* (1993). It assumes a parameteric form for the distribution $P(Y|X)$ then directly estimates its parameters from the training data. The parameteric model assumed by logistic regression in the case where Y is Boolean is expressed as:

$$P(Y = 1|X) = \frac{1}{1 + \exp(\beta_0 + \sum_{i=0}^{n} \beta_i X_i)} \tag{4.6}$$

and

$$P(Y = 0|X) = \frac{\exp(\beta_0 + \sum_{i=0}^{n} \beta_i X_i))}{1 + \exp(\beta_0 + \sum_{i=0}^{n} \beta_i X_i))} \tag{4.7}$$

In our fatigue model, we build a logit node, which is shown below:

$$P_{cr} = P(crack = 1|Life_{inspect}, \Delta\sigma) = \frac{1}{1 + \exp(-\alpha)} \tag{4.8}$$

where $\alpha = \ln(Life_{inspect}) - (\beta_1 - \beta_2 \ln(\Delta\sigma))$. Here P_{cr} is the probability of crack and $Life_{inspect}$ and $\Delta\sigma$ are the data that we want to fit. β_1 and β_2 are the model parameters. A Boolean node is then connected with the logit node as shown in Fig. 4.2 to provide the binary response of cracked or not cracked at each detail and inspection. The logit regression fits an empirical distribution to the observed fatigue data, and it is not attempting to directly update any of the existing lognormal S-N fatigue parameters presented in Eq. 4.4. With the parameters β_1 and β_2 known, prediction of future fatigue cracking at any point of time can be quickly accomplished.

4.3.2.4 Probit regression

The probit regression model is another approach using observed binary responses to estimate continuous underlying input parameters. The discussion of probit regression in this section is also based on the methodology presented in *Albert and Chib* (1993). The binary probit regression model is defined below:

$$p_i = \Phi(\boldsymbol{x_i}^T \boldsymbol{\beta}) \quad for \quad i = 1, 2, \ldots, N \tag{4.9}$$

where $\boldsymbol{\beta}$ is a $k \times 1$ vector of unknown parameters, $\boldsymbol{x_i}^T = (x_{i1}, x_{i2}, \ldots, x_{ik})$ is a vector of known covariates, and Φ is the cumulative standard normal distribution. From Eq. 4.5, it can be seen that the initiation life N_I satisfies the lognormal distribution with the parameters λ_I and ζ_I. The probability of a crack after N_I applied loading cycles follows the cumulative lognormal distribution with the same parameters, which can be written as follows:

$$P_{cr} = P(crack = 1|Life_{inspect}, \Delta\sigma) = \Psi(\frac{\ln(N_I) - \lambda_I}{\zeta_I}) \tag{4.10}$$

It is easy to see that this expression is consistent with the probit regression model. As the expression of λ_I also depends on the applied local stress $\Delta\sigma$ at each detail, we rewrite the expression λ_I as follows:

$$\lambda_I = \lambda_{D_{cr}} + \lambda_A - m(\lambda_{k_f} + \ln(\Delta\sigma)) = \lambda'_I - m\ln(\Delta\sigma) \tag{4.11}$$

where λ'_I is the parameter to be determined through probit regression. Unlike the logit regression, this model more closely follows the underlying fatigue model proposed in Eq. 4.4, although it does not attempt to trace back to the individual distribution of A, D_{cr}, and k_f. Once the parameters of the λ'_I and ζ_I are known, it is straightforward to predict the rate of future fatigue cracks.

4.3.3 Example cases

To evaluate the proposed updating approaches, an example problem was created. Using a nominal structural design for the JHSS vessel presented in *Okasha et al.* (2010a), a hypothetical fatigue inspection updating data set was generated. The midship section of the vessel is shown in Fig. 4.3 below. Inspections were assumed to concentrate on longitudinal web frame attachments in the uppermost vessel deck, including the underside of the top deck, the side shell between the top and first interior deck, and the underside of the first interior deck and double bottom structure. These locations were selected since they have the highest stress range under vertical hull girder bending and would be expected to crack first. A total of 176 details were included per web frame.

Simulated fatigue life data was first generated using the parameters shown in Table 4.1 where both the mean value and coefficient of variation (COV) are listed. The design stress was selected as an effective stress range that would lead to a 95% probability of the highest loaded detail completing the design life of 1×10^8 cycles without cracking. No variation was assumed in D_{cr}, and all the fatigue life variation

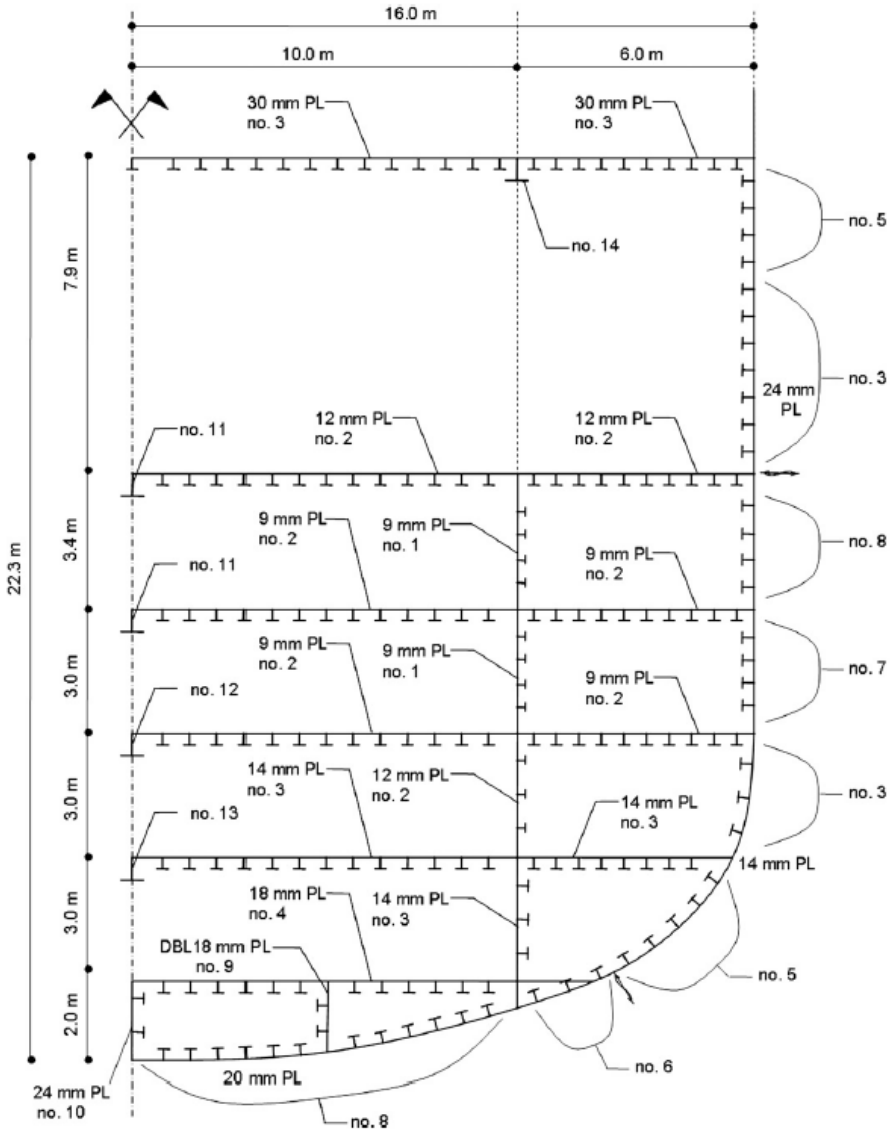

Figure 4.3: Midship section of JHSS (*Okasha et al.*, 2010a).

was assumed to take place in A.

Property	Mean Value	COV
A	1×10^{12}	0.3
m	4	–
D_{cr}	1.0	–
k_f	1.0	0.1
Design Life	1×10^8 cycles	–
Equivalent Stress Range	8.01 MPa	–

Table 4.1: Simulated fatigue properties of JHSS.

By using the parameters shown in Table 4.1 and a pseudo-random number generator, a fatigue cracking history for the hypothetical vessel was established, tracking the number of cycles each detail would crack. This data was then used to generate inspection data at various numbers of cycles, assuming for simplicity, perfect inspections that would always detect cracks if present. Inspections were set to occur between 6×10^7 cycle and 1.8×10^8 cycles, representing 60% and 180% of the vessel's design life. Inspections either covered one frame with 176 total details inspected or five frames, with 880 total details inspected. This synthetic inspection data was then provided to the two updating methods. The simulation was then run out to eight times the design life (8×10^8 cycles) to provide data for comparing the predictions of the future state of the structure made by the updating models with the simulated cracking data.

The logit regression approach was applied with $80,000$ MCMC cycles-including a $40,000$ cycle burn-in period-used to estimate the distributions of parameter β. Results were plotted as the average absolute error between the cracking probability predicted by the logit regression and the simulated fatigue data cracking probability. This probability was calculated at each detail and the average absolute error determined from all the details. Sample graphs are shown in Fig. 4.4 and Fig. 4.5 for the one and five-frame inspection data sets. One such line is generated for inspection case, and after the inspection occurs, the logit-fitted model is than extrapolated to predict

occurrence of cracking in the future. In each case, the model only received data for a single inspection with the inspection occurring at different periods in time.

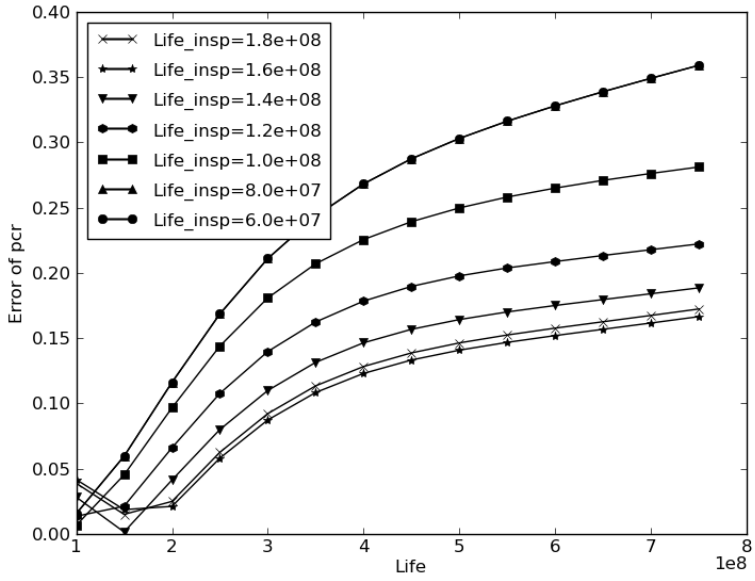

Figure 4.4: One-frame logit regression results.

Fig. 4.4 and Fig. 4.5 show that increasing the amount of data by a factor of five does not significantly change the prediction accuracy for this method. It is clear that inspecting early in the life, where few failures are anticipated, does not give as accurate predictions later in life. However, the error between the predictions and the simulated data can be quite small even at extreme lifetimes, which indicates that the method does hold some promise as a life-cycle analysis technique. The β_1 and β_2 parameters for the five-frame inspection are reproduced in Table 4.2 below against the inspection cycle. As inspections are carried out later and later in the vessel's life, more cracks have been observed and the estimate of the as-built fatigue parameters would be expected to become more accurate. As can be seen from Table 4.2, the mean parameters β_1 and β_2 appear to slowly converge but are still not converged even using inspection data at 180% of the original design life. Furthermore, the standard deviation of the parameters does not appear to converge. This result indicates that

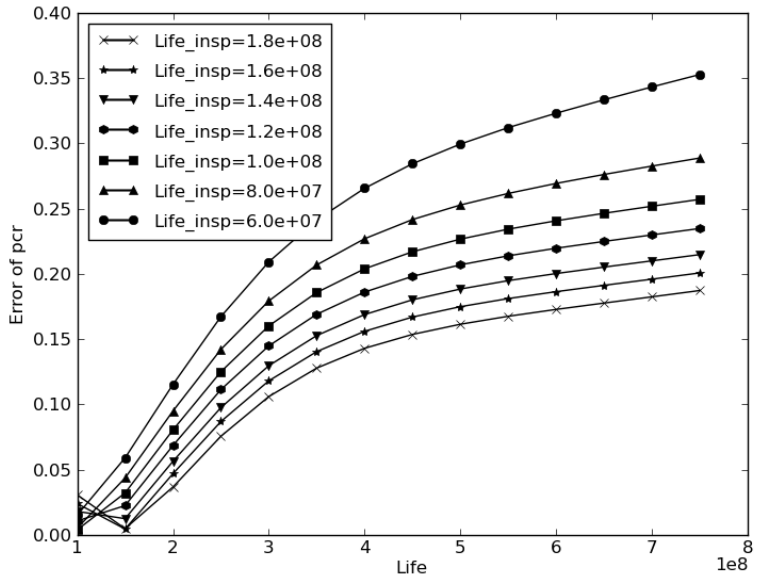

Figure 4.5: Five-frame logit regression results.

the method, while showing some promise, may require additional inspection data if stable results are to be obtained early in the vessel's life.

Inspection Cycle	Mean β_1	Std β_1	Mean β_2	Std β_2
6.0×10^7	29.2	5.30	2.23	2.86
8.0×10^7	38.8	5.88	8.14	2.80
1.0×10^8	46.4	6.74	12.3	3.24
1.2×10^8	52.9	7.13	15.6	3.43
1.4×10^8	58.5	7.29	18.4	3.50
1.6×10^8	64.0	7.04	21.1	3.38
1.8×10^8	69.4	6.86	23.8	3.30

Table 4.2: Logit regression parameters for the five frame case.

Similar procedure applies to the probit regression approach with $80,000$ MCMC cycles used to estimate the distribution of the regression parameters and a $40,000$ cycles burn-in period. The one-frame inspection set is shown in Fig. 4.6 below and the five-frame inspection in Fig. 4.7.

Unlike logit regression, it appears that adding additional data from one-frame to five-frames of inspection does increase the accuracy of the method noticeably at long

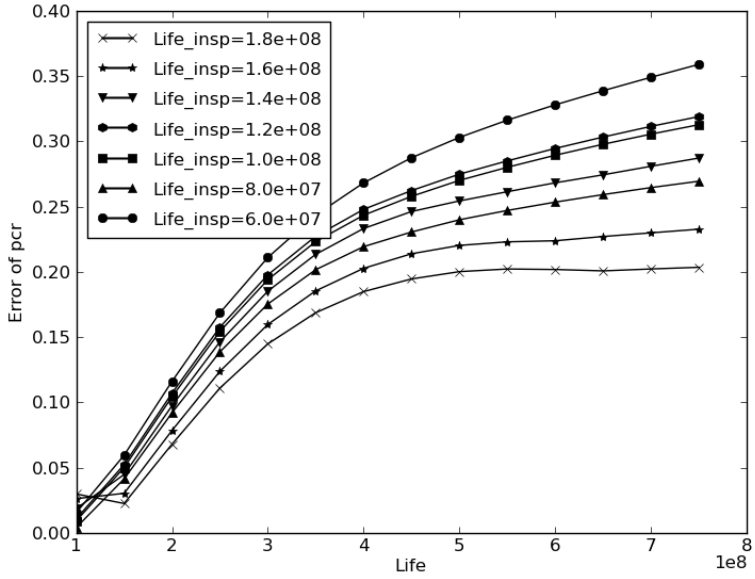

Figure 4.6: One-frame probit regression results.

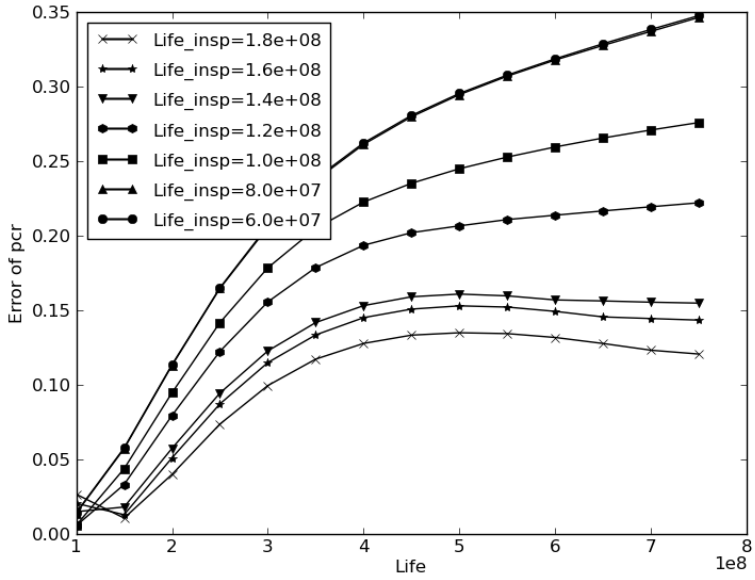

Figure 4.7: Five-frame probit regression results.

lives for probit regression. Table 4.3 shows that the parameters of the fatigue life distribution start to converge early, and are more stable than the logit parameter estimates. Additionally, the standard deviation of the estimates of these parameters reduces when more cracks are observed. This further indicates that the probit regression is more successful in determining the as-built fatigue properties from the inspection data than the logit method, provided a sufficient amount of available inspection data.

Inspection Cycle	Mean λ'_I	Std λ'_I	Mean ζ	Std ζ
6.0×10^7	33.5	4.78	2.60	1.61
8.0×10^7	31.0	4.55	2.25	1.72
1.0×10^8	28.9	1.78	1.46	0.90
1.2×10^8	28.5	0.78	1.35	0.47
1.4×10^8	28.4	0.37	1.38	0.27
1.6×10^8	28.2	0.27	1.29	0.22
1.8×10^8	28.1	0.19	1.25	0.17

Table 4.3: Probit regression parameters for the five frame case.

4.3.4 Summary

Overall, a new framework for life-cycle fatigue management was proposed based on the concept of estimating the as-built fatigue properties of a high-speed vessel through crack inspection results. This approach treats the vessel as an on-going fatigue experiment. By using local fatigue approaches, the number of fatigue parameters that must be determined is significantly reduced. A lognormal fatigue model for the initiation life period based on existing S-N fatigue approaches was proposed. Two different methods of interpreting inspection results and predicting future fatigue performance were presented: a simple logit regression approach and a probit regression approach based on the overall life distribution factors. The application of these methods to the example case presents an intriguing range of results. The simple logit regression model produced reasonable results, and generally performed the best for

the one-frame inspection case. The probit model, which more closely reflected the underlying statistical model used to generate the data, was better able to predict the future fatigue cracking of the vessel when provided with more data. Further investigation is necessary to study the relation between inspection approach and amount of inspection data available.

4.4 Fracture mechanics approach

4.4.1 Overview of fracture mechanics based approach

Although the conventional S-N approach has been widely applied as a pass-fail design stage engineering check, the accumulative fatigue damage indicator only gives the likelihood of a crack occurring with no information about the growth or length of the crack. Unlike the stress life approach, fracture mechanics based fatigue is capable of predicting the size of the crack in the structure at any time. This information can then be used to investigate the impact of an actual crack. Therefore, the method can visibly indicate how a model is performing when measurements become available.

According to *Radaj* (1996), a typical crack propagation process could be divided into several stages as shown in Fig. 4.8. This process includes a dislocation movement, crack nucleation, micro-crack propagation, and macro-crack propagation, final fracture. To model the fatigue process, the first three stages are often lumped into a calibrated initial crack size as robust engineering models of these phases are not yet available. To characterize the propagation stage, linear elastic fracture mechanics (LEFM)

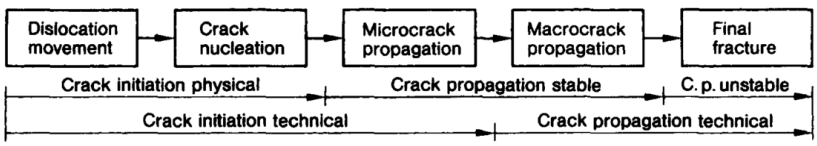

Figure 4.8: Micro and macro phenomena of material fatigue (*Radaj*, 1996).

has often been applied, which assumes that small displacements and general linearity

between stresses and strains. The accuracy of LEFM relies on the crack tip stress intensity factor K, which is, in turn, related with the applied loading, crack size , and the geometry of the crack location. A general form of the LEFM equation is given in Eq. 4.12. However, plastic deformation does occur in the region immediately adjacent to the crack tip; therefore, a plastic zone will form near the crack tip. Experience shows that the basis of LEFM remains valid if this region of plasticity remains small in relation to the overall dimensions of the crack and cracked body.

$$\sigma_{ij} = \frac{K}{\sqrt{2\pi r}} f_{ij}(\theta) \tag{4.12}$$

A general form of stress intensity factor is then given by

$$K = f(a)\sigma\sqrt{\pi a} \tag{4.13}$$

where σ is the far field stress applied to component, a is the crack length, $f(a)$ is the correction factor that depends on specimen and crack geometry. When the structural detail is simple, an explicit approximation of stress intensity factor can be given. Such approximations are tabulated in most of handbooks (*Tada et al.*, 2000; *Rooke and Cartwright*, 1976). However, if the structure details are complicated, then more advanced numerical calculation are necessary such as the energy release rate through a J-integral (*Suresh*, 1998).

The relations between stress intensity factor range ΔK and crack growth rate da/dN is often plotted in a log-log scale as shown in Fig. 4.9. In region I, when ΔK decreases, the crack growth rate drops significantly. The asymptote ΔK_{th} is the threshold of the stress intensity factor range below which no fatigue crack growth occurs. At the other extreme, when in region III, and when ΔK is large, the crack growth rate accelerates significantly. In this region, ΔK will approach the fracture toughness K_c and material will often fail by rupture.

In region II, the crack growth rate da/dN can be approximated linearly in re-

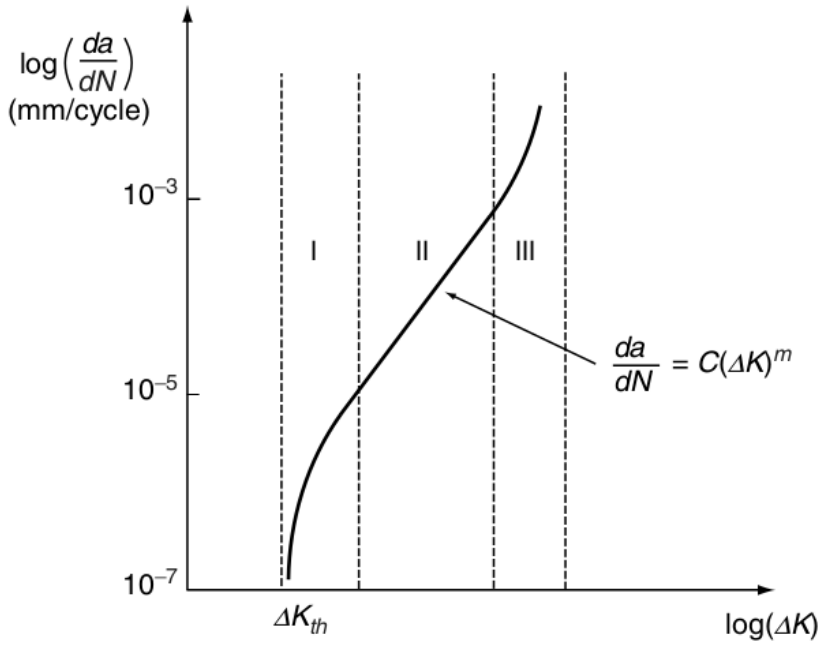

Figure 4.9: Schematic plot of the typical relationship between the crack growth rate and the range of the stress intensity factor (*Lee et al.*, 2004).

lation to the stress intensity factor range ΔK in the log-log plot. The relation is characterized through the known Paris' law, which is shown as below

$$\frac{da}{dN} = C(\Delta K)^m \tag{4.14}$$

where the C and m are material constants. To find C and m, a least square fit is often performed to fit the fatigue experimental data. Therefore, after substituting the Eq. 4.13 into the Eq. 4.14, the equation becomes

$$\frac{da}{dN} = C(f(a)\Delta\sigma\sqrt{\pi a})^m. \tag{4.15}$$

It is easy to find that this equation can not be solved by integrating the both sides directly, since $f(a)$ is the function of crack size, which cannot be solved explicitly. A general solving method divides the time into several small steps and assumes a constant $f(a)$ within each time step. Therefore, integration can be performed on both sides and the crack size at time of t can be expressed according to the crack size

at last time step of $t-1$, which is shown in Eq. 4.16

$$a_t = [(1-\frac{m}{2})CY(a_{t-1})^m \Delta\sigma^m \pi^{m/2} n + a_{t-1}^{1-\frac{m}{2}}]^{\frac{1}{1-m/2}} \tag{4.16}$$

where n is the number of cycle experienced at time step t.

4.4.2 Reliability updating using Bayes' rule

As the fracture mechanics approach uses crack size as direct input, it is more attractive to apply this approach into the reliability updating and fatigue management than the stress life approach. A simple reliability updating can be solved by the Bayes' rule: the probability of event A happens given the event B can be calculated by the event A and B happen together, divided by the probability only the event B happens. Eq. 4.17 shows the formula of updating probability of detecting a crack based on a previous inspection record.

$$P(m_{t_2} \neq 0 | m_{t_1} = 0) = 1 - \frac{P(m_{t_2} = 0 \cap m_{t_1} = 0)}{P(m_{t_1} = 0)} \tag{4.17}$$

where m_{t_1} and m_{t_2} stand for the inspection at t_1 and t_2 time. 0 means no crack has been detected and 1 means a crack has been detected. Fig. 4.10 shows an example of updated mean crack depth as well as the probability of detection (POD) after inspection performed at the 2nd year with no crack being detected. An exponential POD curve with respect to the crack size needs to be assumed first while the numerator and denominator terms in Eq. 4.17 could be calculated separately by using classic FORM/SORM method or Monte Carlo simulation.

Fig. 4.10 demonstrates that since there is no crack detected at the second year, the updated crack depth is smaller than the original design prediction, which shows a probability of overestimation in terms of the crack growth speed. Also, the POD can be updated. The value drops to zero when inspection is performed and no crack is found, and then grows faster than the design prediction in the following years. After

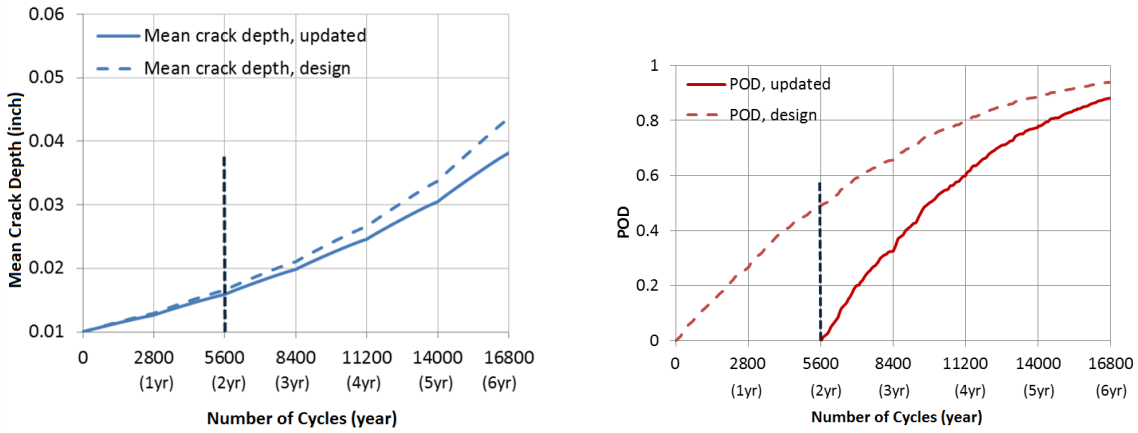

Figure 4.10: Detection updating for mean crack depth (a) and POD (b) after inspection performed at the 2nd year with no crack detected.

six years, the design and updated prediction have the same level of POD again.

4.4.3 Fatigue management based on fracture mechanics approach

Although the reliability updating method using Bayes' rule is simple and robust, it becomes intractable when complicated SHM information needs to be incorporated as evidence or multiple random variables need to be updated. To overcome these shortcomings, a DBN-based crack growth model is presented below that is capable of graphically combining the different sources of uncertainty together and inferring the distribution efficiently based on SHM data. The theory of DBN model has already been presented in Chapter Two.

The DBN structure used to model deterioration in this work is based on a general model first proposed by *Straub* (2009) and later used in *Zhu and Collette* (2013). Consider the crack growth model as a case of a general deterioration process modeled by DBN, as shown in Fig. 4.11. For $t = 1, 2, 3, \ldots, T$, the a_t node is the actual crack size at t time step while the a_0 node is the initial flaw size. The X_t node sets contain all those deterioration parameters, which control the crack growth rate at each time step. The M_t node represents the in-service measurement of crack size, which used

as updating evidence from in-service inspection.

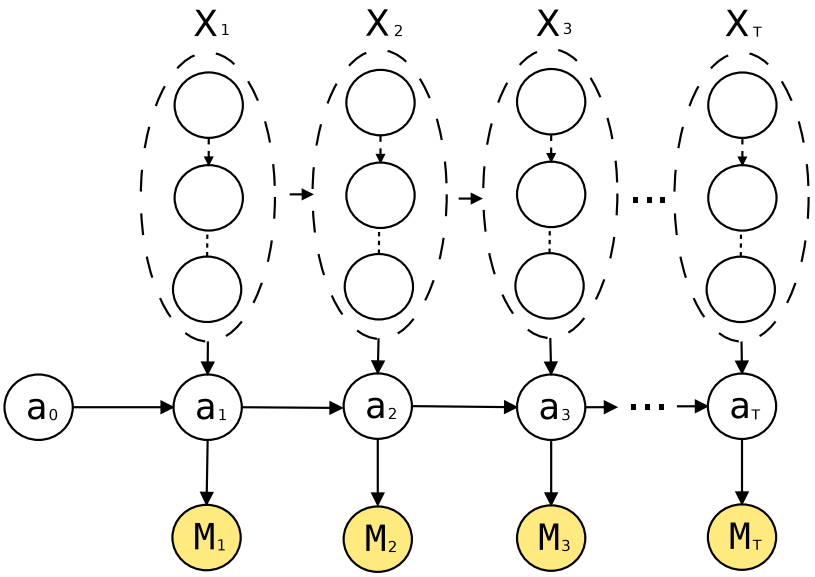

Figure 4.11: A general deterioration process modeled by DBN.

In such a model, it is common to assume that a critical crack size l_c, exists, and if the crack size exceeds l_c, then failure has occurred. For reliability analysis, the accurate calculation of the probability that crack size a_t is larger than l_c at each time step t is often more critical than modeling the whole distribution of the probability density function of the crack size. The probability of the crack size exceeding l_c is taken as the probability of failure (POF). The POF can be further transferred into a reliability index β as shown in Eq. (4.18).

$$\beta = -\Phi^{-1}(POF) \tag{4.18}$$

During initial design, the network runs to generate a prior engineering prediction of crack size over time. When in-service measurement of crack size are available, they are entered as evidence on the M_t nodes, and the network can be updated for the future belief of crack size as well as the parameters that drive the crack growth model. Assume until time step i ($i \leq T$), the $m_{1:i}$ nodes are observed as evidence (i is the latest inspection time). Then, two kinds of inference normally can be computed at

time step t: smoothing $P(a_{t=i-k}|m_{1:i})$ for $0 \leq k < i$ and prediction $P(a_{t=i+k}|m_{1:i})$ for $0 < k \leq T - i$. To infer a DBN, an iterative frontier algorithm is applied. A detailed description of frontier algorithm can be found in Chapter Two.

However, a central challenge with respect to DBNs for reliability problems is the need to discretize continuous random variables. Although the accuracy of reliability estimation could be resolved by increasing number of intervals, the resulting growth of computational cost would make the problem potentially intractable. As the Bayesian network inference problem has been shown to be N-P hard, there is strong motivation to minimize the number of discretization intervals needed to obtain acceptable accuracy.

4.4.4 Example case of mooring chain jack fatigue

4.4.4.1 Dynamic Bayesian network modeling

This example presents the application of the DBN to represent the fracture mechanics based fatigue model. The crack has been characterized by both depth and width and the interaction between these two parameters has also been considered. A crack on the mooring chain jack crossarm has been investigated with cyclic load occurring from opening and closing of the chain jack for chain movement. Load cells have been installed on the chain jack to record the load during that movement. The reliability analysis is performed to calculate the failure probability based on inspection and monitoring data. Although this example of the proposed DBN model has been applied into the offshore structure, the DBN also applicable to the ship structure.

The Fig. 4.12 shows the DBN of the two dimensional crack growth model. Here, the overall relationship between da/dN and ΔK is modelled by a bilinear S-N curve where two sets of crack growth properties need to be defined in Eq. 4.14. Since both crack depth a and crack width $2c$ are considered, the stress intensity factor is the

function of both a and c. Therefore, the updated Paris' law could be rewritten as

$$\text{Stage I}: \quad \begin{cases} \frac{da}{dN} = A_1 \Delta K_a(a,c)^{m_1} & \text{if } \Delta K_0 \leq \Delta K_a < \Delta K_t \\ \frac{dc}{dN} = A_1 \Delta K_c(a,c)^{m_1} & \text{if } \Delta K_0 \leq \Delta K_c < \Delta K_t \end{cases} \tag{4.19}$$

$$\text{Stage II}: \quad \begin{cases} \frac{da}{dN} = A_2 \Delta K_a(a,c)^{m_2} & \text{if } \Delta K_a \geq \Delta K_t \\ \frac{dc}{dN} = A_2 \Delta K_c(a,c)^{m_2} & \text{if } \Delta K_c \geq \Delta K_t \end{cases} \tag{4.20}$$

where ΔK_0 is the threshold stress intensity factor below which da/dN is assumed to be zero, ΔK_a and ΔK_c are the stress intensity factor range in terms of depth and width direction respectively, A_1 and m_1 are the material constants for Stage I, and A_2 and m_2 are the material constants for Stage II. The stress intensity factor is calculated by the BS 7910 (*British Standards Institution*, 2005) code while the failure is assessed by level 2A failure assessment diagram (FAD), considering both fatigue and fracture failure. The DBN model considers the uncertainty from A_2, initial crack

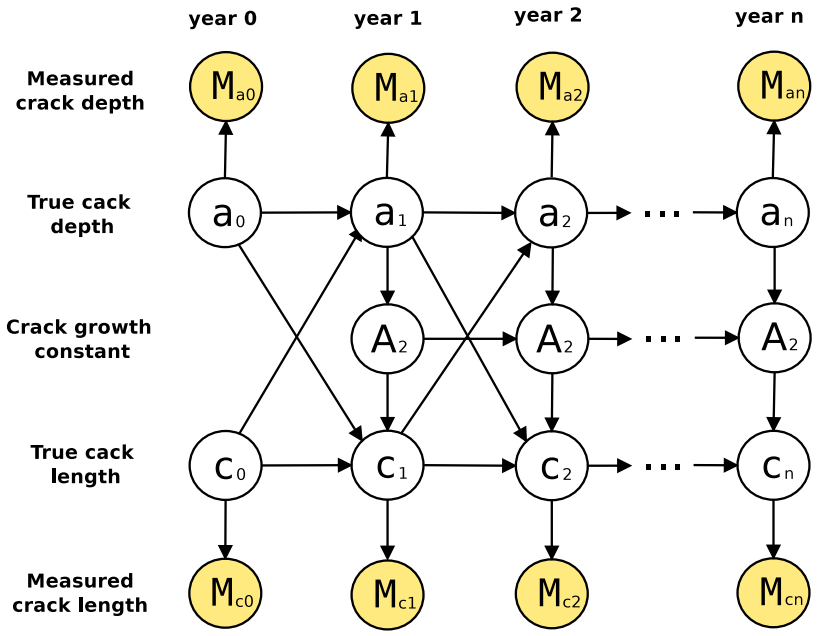

Figure 4.12: Two dimensional crack growth model using DBN.

size, and measurement uncertainty. Each slice represents a year, and the crack size at year t is related with A_2 at year t and the crack size at year $t-1$. The measured

crack size is assumed to satisfy the normal distribution with the mean of true crack size.

The model is applied into the mooring chain jack crossarm, which experiences cyclic loads during the mooring chain movement. Load cells have been installed to measure the mooring tension load during the movement. Cycle counting is then performed from the time domain tension load history to plot the histogram of tension load versus number of cycles for each year. Fig. 4.13 shows an example of a mooring tension load histogram for one offshore production semi-submersible. The total number of cycles is 2546. For the future years, a 10% scaling factor has been added to consider the uncertainty for future load prediction which reaches about 2800 cycles in total for each year. Since the sequence of load data is neglected, the crack growth has been integrated from the highest load level to the lowest load level. A FE analysis has been performed to transfer the tension load to the stress at stress concentration area where the crack occurs.

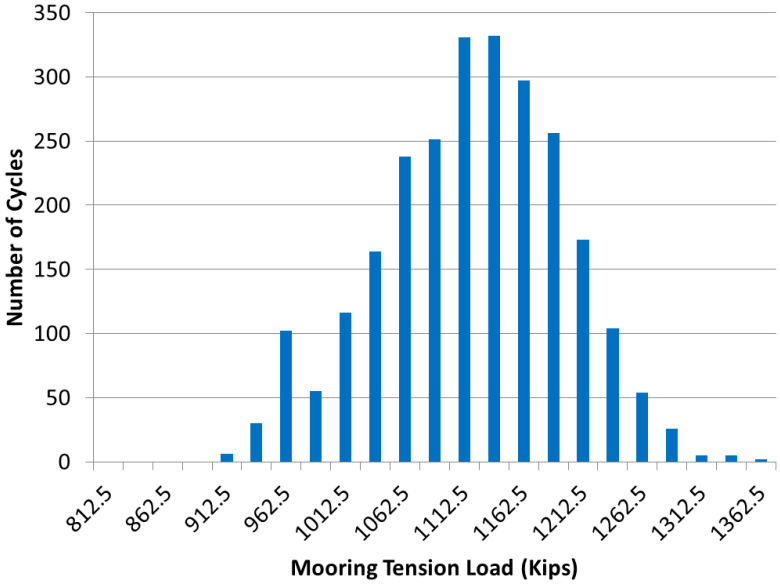

Figure 4.13: A example of load histogram for the chain jack.

The deterministic parameters and the random variables of the DBN model are listed in Table 4.4 and Table 4.5, respectively. Most of parameters are assumed

according to the recommendations of BS 7910 code while the others (such as measurement error) are determined according to typical ultrasonic tools specifications.

Variable	Unit	Value
m_1	-	8.16
A_1^*	-	1.72×10^{-15}
m_2	-	2.88
ΔK_0	$ksi\sqrt{inch}$	1.81
ΔK_t	$ksi\sqrt{inch}$	4.14

*The units of Paris' law constants are based on $da/dN = A_1(\Delta K)^{m_1}$ for ΔK in $(ksi\sqrt{inch})$ and da/dN in $(inch/cycle)$ and same for below.

Table 4.4: The parameters of two dimensional crack growth model.

Variable	Unit	Distribution
A_2	$inch$	$lognormal(m_{A_2} = 4.24 \times 10^{-10}, COV_{A_2} = 0.3)$
a_0	$inch$	$\exp(\mu_{a_0} = 0.01'') + 0.01''$
c_0	$inch$	$\exp(\mu_{c_0} = 0.02'') + 0.03''$
M_{a_t}	$inch$	$normal(m_{a_t} = a_t, std_{a_t} = 0.01'')$
M_{c_t}	$inch$	$normal(m_{c_t} = c_t, std_{c_t} = 0.02'')$

Table 4.5: The distributions of the DBN's random variables.

Before the implementation the inference of the DBN, discretization needs to be performed for each random variable, which is summarized in Table 4.6. The range of A_2 is chosen around the mean value, and the range of crack size has been chosen according to the limit of structure size. A logarithmic discretization has been chosen for all crack size random variables as the crack growth rate increases exponentially, while a uniform distribution has been assumed for the A_2 node. The probability mass function (PMF) of $P(A_2)$, $P(a_0)$, $P(c_0)$, $P(M_{a_t}|a_t)$ and $P(M_{c_t}|c_t)$ are calculated analytically according to Table 4.5. The $P(A_2|A_2)$ is assumed unchanged over time, and $P(a_t|A_2, a_{t-1}, c_{t-1})$ and $P(c_t|A_2, a_{t-1}, c_{t-1})$ are calculated according to the BS 7910. The number of cycles between the slices is $\Delta n = 2800$, as stated above. The frontier algorithm for DBN has been applied, which has already been described in Chapter Two.

Variable	Probable range	Num. of states	Interval boundaries
A_2	$8.4 \times 10^{-11} \sim 2.1 \times 10^{-9}$	60	$[0\ 8.4 \times 10^{-11} : 1.926 \times 10^{-9}/59 : 2.016 \times 10^{-9}]$
a_t	$0.01 \sim 7$	60	$\exp[\ln(7) : (\ln(7) - \ln(0.01))/60 : \ln(7)]$
c_t	$0.03 \sim 36$	60	$\exp[\ln(36) : (\ln(36) - \ln(0.03))/60 : \ln(36)]$
M_{a_t}			same discretization as a_t
M_{c_t}			same discretization as c_t

Table 4.6: Discretization scheme for the two dimensional crack growth model.

4.4.4.2 Results

A validation has been performed first to compare the results with the Monte Carlo simulation without any inspection information. This tracks the POF over time, showing that the DBN can predict the same features as conventional simulation. As shown in Fig. 4.14, the POF has been plotted with respect to the number of cycles or the year. For both methods, each bin of year basis variable amplitude load histogram shown in Fig. 4.13 has been split into smaller number of cycles if it is greater than 100 cycles. For each year, the integration is performed from the highest load to the lowest load, which assumes the higher load amplitude occurs first. These procedures guarantee enough accuracy as well as conservative results when performing forward integration for Eq. 4.16. Therefore, since each step size for Monte Carlo simulation is equal to or less than 100 cycles with higher load coming first, a sharp increase of POF can be seen at the beginning of each year. This step occurs because the probability of fracture is higher under the highest load. While, for the DBN method, although the curve is consistent with the Monte Carlo simulation, it does not have those sharp changes in POF. This is because the load has already been integrated into the CPT generation and the minimum time step for DBN is defined as one year.

Since no inspection result from the DBN model is generally consistent with the Monte Carlo simulation, the inspection data has been incorporated into the DBN to update the model. The Table 4.4.4.2 shows the assumed inspection records. Two

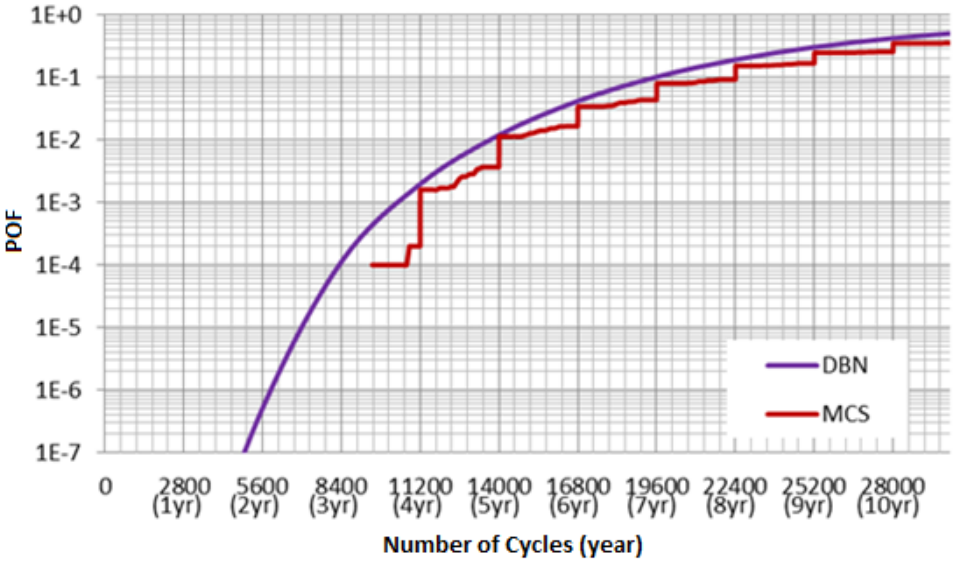

Figure 4.14: Validation of POF without inspection.

inspections have been performed at the third and sixth year with measurements of both crack depth and crack length. The results for on-line updating due to different

Inspection year	Measured Crack depth (a)	Measured crack length (2c)
$3rd$	$0.03''$	$0.18''$
$6th$	$0.05''$	$0.3''$

Table 4.7: Assumed inspection records.

measurement standard deviations are compared as shown in Fig. 4.15, as the uncertainty exists due to human factor or equipment. Generally, each time when an inspection is performed, the POF drops as the inspected results are far away from critical crack size. However, the POF does not drop as much after the second time inspection as the first time inspection since the inspected size is larger. Also, if the inspected results have a relatively high confidence, the POF will grow slower than the inspection with low confidence. Therefore, by identifying the POF at different stage of structure, the risk based integrity management can easily incorporate this DBN framework.

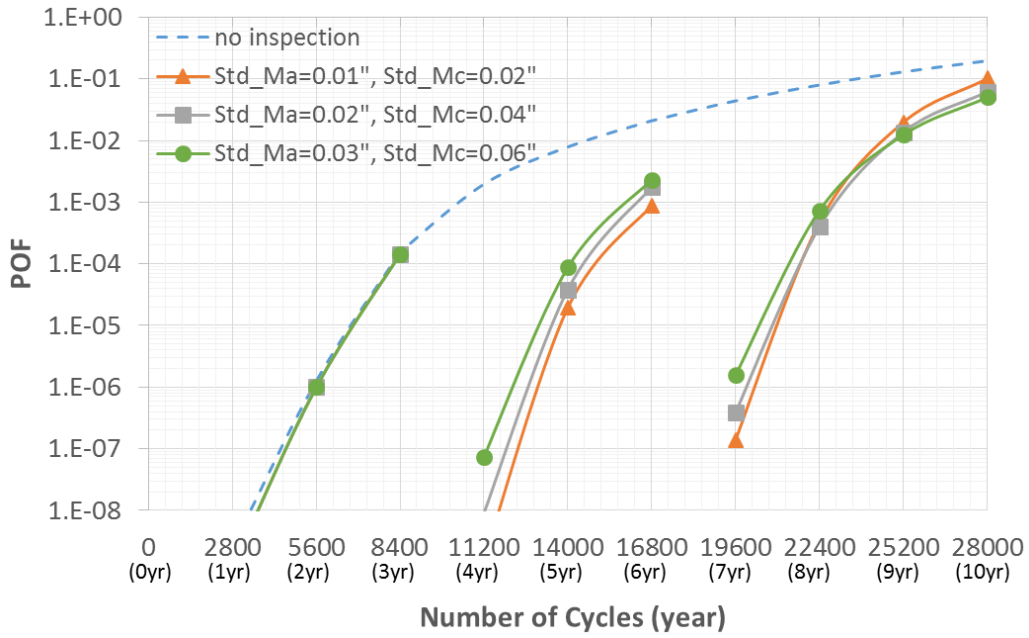

Figure 4.15: Comparison of different measurement confidence level for POF updating under inspection.

4.4.5 Summary

Generally, compared to the stress life based fatigue management, the fatigue management based on fracture mechanics approach could characterize the actual crack size, which is more convenient to incorporate the SHM information. The method is based on Paris' law, which uses linear regression to fit the logarithmic scale of fatigue data. A DBN was built according to the random variables, and inference was performed to find the prior and posterior distribution based on inspected crack size. Different inspection confidence levels were compared after the validation of the model. The POF was calculated as the reliability estimation was of interest for this example. The model used mooring chain jack crossarm as an example, and the inspection updating results shows the influence of measurement variance on the reliability output. The results can be used for guidance of chain jack crossarm replacement timing.

The discretization strategy is one of the important factors for the accuracy of reliability estimation, so a dynamic discretization scheme will be proposed in follow-

ing section that focuses on how to accurately evaluate the tail region's probability rather than the whole distribution shape. The scheme takes the form of an iterative algorithm, which dynamically partitions the discretization intervals at each iteration according to posterior distribution of each node. Through applications to two stochastic crack growth example problems, the algorithm is shown to be a robust and accurate DBN-based structural reliability tool.

4.5 Adaptive discretization for reliability estimations

4.5.1 Introduction

The inference of DBN involves applying different discretization techniques to discretize each continuous node into a discretized node. An exact inference method, such as a junction tree, typically can be applied to infer the Bayesian networks. Since exact inference has been proven to be a NP-hard problem (*Darwiche*, 2009), the computational cost will grow exponentially with respect to the number of intervals chosen for each node. The simplest and most traditional approach is a uniform discretization of all continuous nodes where discretization remains static throughout inference. Generally, increasing the number of discretization intervals improves the accuracy of the model; however, as life-cycle data becomes available for evidence, the posterior probability distribution concentrates on certain regions that the provided evidence suggests as more probable. Denser discretization intervals are required to maintain the level of accuracy in these more probable regions. Conversely, for regions with lower probability, the size of intervals can remain relatively large. Therefore, a uniform discretization approach can be computationally inefficient for this type of problem.

Beyond discretizing continuous random variables for reliability calculations, the probability of failure (POF) must be computed at any point during the structure's

service life. This value normally can be found from summation of the small "tail region" probability density functions, which can involve small probabilities, on the order of as little as $10^{-9} \sim 10^{-10}$, early in the structure's lifespan. The conventional discretization scheme focuses on properly approximating the whole probability distribution, and significantly fewer investigations have been made to investigate this "tail region probability".

The sections below attempts to extend upon a model introduced by *Straub* (2009) where a DBN is used to model a general structural deterioration process. However, the focus of the investigation is the accuracy of the reliability output and it relationship to the discretization scheme, including cases with inspection evidence. A new reliability purposed dynamic discretization (RPDD) algorithm is proposed, which is suitable for this DBN approach (*Zhu and Collette*, 2013). The goal is to find an optimum discretization method for DBN-based deterioration processes with lower computational complexity while achieving the same level of accuracy for reliability analysis as conventional discretization. The effect of inserting inspection evidence will also be considered and combined into the proposed algorithm. The error due to discretization will be identified first in next section, followed by an introduction of the new dynamic discretization technique. Two examples will be provided: first, a simple constant crack growth model with assumed normal distribution for all the nodes, and then *Straub* (2009)'s stochastic crack growth model. For both examples, the new dynamic discretization will be compared to the previous discretization for both computational cost and prediction accuracy. A summary will be provided in Section 4.5.5.

4.5.2 Discretization error identification

In the previous Fig. 4.11, all continuous nodes must be discretized, which can lead to an error in the reliability computation. This error can be split into two types

according to the different inference task it occurs in: smoothing or prediction.

Smoothing attempts to estimate the past crack size, given the measurement up to the current time, t. This is an effective way to trace how the crack develops as well as update the belief in the initial crack size. Due to uncertainty in crack size measurements, even if the measurement result at time step i is less than l_c, a small probability remains that actual crack size has already reached l_c. It is assumed that the error is dominated by the maximum probability bin in the discretization of each random variable that contributes to the POF calculation for the a_t node. The goal becomes to find this bin that contributes the most to the POF calculation. To solve this problem, another "virtual evidence" a_v $(1 < v \leq i)$ is inserted on the a_t node at which the crack size is above the l_c. By examining the parent nodes of the a_t node, the posterior distribution of these parents can be obtained. As virtual evidence of a failure has been introduced at a_t, the posterior distribution of a_t's parents represents an approximation of the most likely route to failure at a_t. The interval in a_t's parents' discretization that has the highest posterior probability can be hypothesized as the most likely bin to lead to a_t exceeding l_c, and is a good candidate for subdivision to increase the accuracy of the discretization. In additional to virtual evidence, any prior measurements can simultaneously be entered into the network during this calculation, allowing all available information to determine the optimum place for subdivision. Eq. (4.21) represents this hypothesis that smoothing error is proportional to the maximum probability given the inspection evidence $m_{1:i}$ and virtual evidence a_v. The smoothing error of X_t can also be obtained accordingly by changing the a_t with X_t in Eq. (4.21). It is significant to note that calculating the posterior distribution after inserting new evidence will result in extra computational cost. Therefore, the number of nodes to be queried should be as small as possible while still representing most of the distribution's characteristics. One method is to query the parents of each "virtual evidence", that is on the slice of "virtual evidence", or

one slice before, since those nodes are directly linked with or close to the measurement that could be affected significantly.

$$E_{smooth}(a_t) \propto max(P(a_t|m_{1:i}, a_v)) \tag{4.21}$$

In addition to smoothing, errors in the prediction of future states are also important to identify. Eq. (4.22) shows the prediction of future crack size a_{i+k} based on previous measurements $m_{1:i}$. The h_i denotes all the hidden nodes in i time step, which is the joint probability distribution of X_i and a_i in Fig. 4.11. Once the posterior distribution of X_i is obtained, the future state of a_{i+k} can be easily computed by marginalizing out all the intermediate X_t and a_t nodes from $i+1$ to $i+k$ time steps.

$$P(a_{i+k}|m_{1:i}) = \sum_x P(h_i = x|m_{1:i})P(X_{i+k}|h_i = x) \tag{4.22}$$

Again, it can be assumed that the error of estimating the POF for $t(t > i)$ is driven by the maximum probability bin of a_{t-1} that reaches critical size at a_t node. However, for the DBNs, as the nodes at the current time step are linked to the nodes at the future time step, the error of computing crack size growth at the current time step will also be brought to the future time step, resulting in an incorrect prediction. Therefore, this assumption can be slightly modified by assuming that the error of estimating the POF for $t(t > i)$ is driven by the bin of X_t or a_{t-1} that have the maximum probability of crack size increase from the a_{t-1} to the a_t node.

Instead of considering error that each bin goes to failure, this assumption considers the error that is transmitted and leads to failure after time step t. This error is therefore called the prediction error. If $q(X_t, a_{t-1})$ denotes the joint probability table of $a_t > a_{t-1}$ for a different combination of X_t and a_{t-1}, which can be written as $P(a_t > a_{t-1}|m_{1:i})$, then Eq. (4.23) and Eq. (4.24) show the calculation of prediction error for a_{t-1} and X_t nodes.

$$
\begin{aligned}
E_{pred}(a_{t-1}) &\propto max(\sum_{X_t} q(X_t, a_{t-1})) \\
&\propto max(\sum_{X_t} \sum_{a_t > a_{t-1}} P(a_{t-1}|m_{1:i}) P(X_t|m_{1:i}) P(a_t|X_t, a_{t-1}))
\end{aligned}
\tag{4.23}
$$

$$
\begin{aligned}
E_{pred}(X_t) &\propto max(\sum_{a_{t-1}} q(X_t, a_{t-1})) \\
&\propto max(\sum_{a_{t-1}} \sum_{a_t > a_{t-1}} P(a_{t-1}|m_{1:i}) P(X_t|m_{1:i}) P(a_t|X_t, a_{t-1}))
\end{aligned}
\tag{4.24}
$$

4.5.3 Proposed reliability purposed dynamic discretization algorithm

Therefore, based on the equations presented above, a dynamic discretization algorithm can be developed which is suitable for reliability-based deterioration process DBNs models. The algorithm is composed of five major steps, which are explained below.

1. **Initialization** Though the proposed dynamic discretization algorithm is not highly sensitive to the initial discretization, the initial discretization still needs to be carefully considered, as it is helpful in making the algorithm more efficient. A recommended method is to use a uniform discretization for root nodes and perform a Monte Carlo simulation for the remaining nodes. The initial intervals of those nodes can then be divided according to the sampling distribution. Also, the initial interval range must be large enough to cover both the prior and posterior distribution.

2. **Conditional probability tables (CPTs) generation** After initialization step, the CPT must be generated before executing the inference algorithm in each iteration. *Straub* (2009) proposed a novel discretization approach for any continuous random variables in the DBN. Consider discretization of any single continuous variable represented by node N, where the parents of N denote

N_p, and $\hat{N}_p^{(k)}$ denotes the corresponding discrete variable at k state. Straub's method performs integration on the prior distribution times a conditional probability distribution (CPD) relation within each interval of N_p. If the N_p is the root node (meaning that it does not have any parents), that approximation will not cause much error. While the N_p is not the root node, a uniform prior distribution is further assumed if the $\hat{N}_p^{(k)}$ has the upper and lower boundaries, and an exponential distribution is assumed if only one boundary exists. As each time slice in the DBN shares the same nodal distributions, the bin intervals used in this discretization must support a variety of different distributions over time. Thus, the distribution shape can change at different time steps. This makes such an approximation to estimate CPTs accurately more challenging to construct. Additionally, the numerical integration can be computationally expensive in an iterative discretization scheme. Therefore, in our approach, if the N_p is not the root node, the prior distribution is neglected and only one or a few points are selected to estimate the probability within each interval, which is shown in Eq. (4.25). Here, only one point is selected for approximating the X_t node while three points are used for a_t and M_t nodes, as more accuracy is needed.

$$F_N(N|\hat{N_p}^{(k)}, Y_p) \approx \frac{1}{j} \sum_{\substack{n_p=[\hat{N}_{pl}^{(k)}, \hat{N}_{pm}^{(k)}, \hat{N}_{pu}^{(k)}] \\ or \;\; n_p=\hat{N}_{pm}^{(k)}}} F_N(N|n_p, Y_p) \tag{4.25}$$

Where Y_p are realizations of all random variables that are parents to N excluding N_p; $\hat{N}_{pl}^{(k)}$, $\hat{N}_{pm}^{(k)}$ and $\hat{N}_{pu}^{(k)}$ represent the lower bound, mean, and upper bound for each interval. If only one boundary exists in an interval, Straub's method can still be applied, which assumes an exponential prior for the N_p node. Although the approximation in Eq. (4.25) for a two boundaries bin seems to be "rough", the error of each interval is approximately proportional to the size of the inter-

val, and can be reduced by dividing intervals with larger errors. However, for the intervals with only one boundary, the exponential prior approximation can potentially cause more error for the POF calculation since the error cannot be reduced by reducing the interval size. The calculation of the POF of the a_t node is the summation of bins that range between l_c and infinity, which includes the final infinite boundary bin. Therefore, to help reduce the POF error for the a_t node, there should be at least one bin with a finite upper boundary above l_c that accounts for the majority of the POF. If $\hat{a}_k$ $(k = 1, 2, 3, \ldots, j)$ denote the discrete variable with j states, and the j-th state has the bin with one boundary, the following relationship holds:

$$P((\hat{a}_j)_{1:T}|m_{1:i}) \ll P((\hat{a}_{j-1})_{1:T}|m_{1:i}) \tag{4.26}$$

3. **Compute the error** After generating CPTs, the smoothing error and prediction error are calculated according to Eq. (4.21) and Eq. (4.24), respectively. For the effective convergence, the prediction error will be computed between time steps i and T using posterior distribution of nodes and CPD relations according to Eq. (4.23) and Eq. (4.24). To compute the smoothing error, the "virtual evidence" is inserted at the largest bin of a_t node with non-zero posterior probability at time step t_v $(2 < v < i)$. Then, different strategies are applied to query the posterior distributions of nodes. For the a_t nodes, the posterior distributions are obtained through time steps 1 to $v-1$, while, for the X_t nodes, the posterior distributions are obtained between 1 and i. Finally, the maximum probability of the bin and the index of that bin are stored for each time step.

4. **Stopping criteria judgement** Two stopping criteria have been established. The first criterion is to judge whether the iteration reaches the maximum num-

ber of iterations since the computational cost can become too expensive to continue performing network inference. The second criterion is to check if $\sum_{t=1}^{T} |\beta_t^{(l)} - \beta_t^{(l-1)}| \ / k_c \leq \alpha$, where $\beta_t^{(l)}$ is the reliability index at iteration l for time step t and k_c is a normalizing constant appropriate for the problem. Here $k_c = \sum_{t=1}^{T} |\beta_t^{(2)} - \beta_t^{(1)}|$, is used, which compares the remaining improvement in β to the initial improvement made by the algorithm in the first cycle. For this work, α is chosen between 0.5% and 1%, which means the variation between $\beta_t^{(l)}$ and $\beta_t^{(l-1)}$ is much less than the initial iteration.

5. **Subdivide the intervals** The subdivision operation is performed at each iteration of the algorithm. Smoothing error and prediction error are run separately and the subdivision intervals are found from the intervals with maximum smoothing and prediction errors at each queried time step, which can be directly obtained through Eq. (4.21) to Eq. (4.24). When repetitive subdivision intervals are obtained, only one will be recorded. Although it may be possible to further improve the speed of the algorithm by optimizing the query time step list, in the present implementation, all time steps are queried in terms of smoothing and prediction tasks. If the stopping criteria are not satisfied, those recorded split intervals index will update the discretization at the next iteration. Right now the bins that need to be subdivided will be split equally into two although further study can be performed for the optimum split location of the bin.

A simple merge operation has also been considered in the proposed algorithm, which tries to merge the zero posterior distribution bins or the bins with the least error. However, it has proven to only slightly reduce computational cost while introducing a potential iteration-to-iteration instability where intervals can be merged and then subdivided on successive iterations. Therefore, merge operators were not used in this calculation. The flowchart of proposed algorithm is shown in Fig. 4.16.

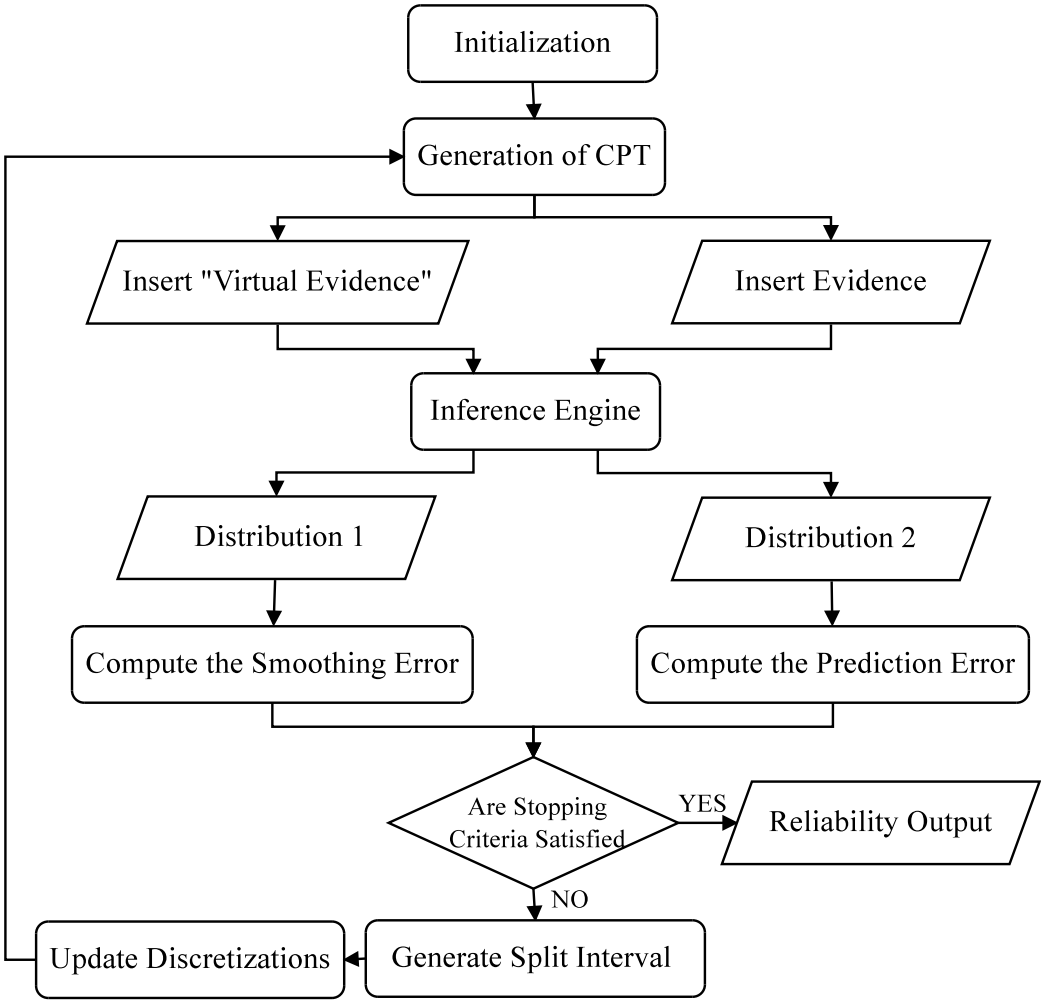

Figure 4.16: Flowchart of dynamic discretization for deterioration process modeling.

4.5.4 Example cases

4.5.4.1 Overview

The proposed algorithm will be applied in the following two examples: first is a simple constant crack growth model where all the nodes satisfy the Gaussian distribution, and the second one is the stochastic crack growth model from *Straub* (2009)'s paper. The reliability index error ε_β for the proposed method will be compared with static discretization for each iteration calculated according to Eq. (4.27). It will be shown that using static discretization, such as uniform discretization for reliability purposed inference, is less accurate and more computationally expensive while the new RPDD algorithm can produce a more accurate reliability estimation for these problems with lower computational cost.

$$\varepsilon_\beta = \frac{1}{T}\sum_{t=1}^{T} |\beta_{approx} - \beta_{true}| \tag{4.27}$$

4.5.4.2 A simple constant crack growth model

A simple constant crack growth model used is shown in Fig. 4.17 to present an application of the proposed algorithm. As shown in Fig. 4.17, only one node da_t is used as the crack growth parameter X_t, which represents the crack size increment between time step $t-1$ and time step t. All those nodes are continuous and assumed to satisfy the normal distribution, thus the exact distribution can be solved by the Bayesian linear regression method from *Carlin and Louis* (2009). The relations of all those nodes are shown in Eq. (4.28) which assume the same prior distribution of crack increment at each time step for $t = 1, 2, 3, \ldots, T$.

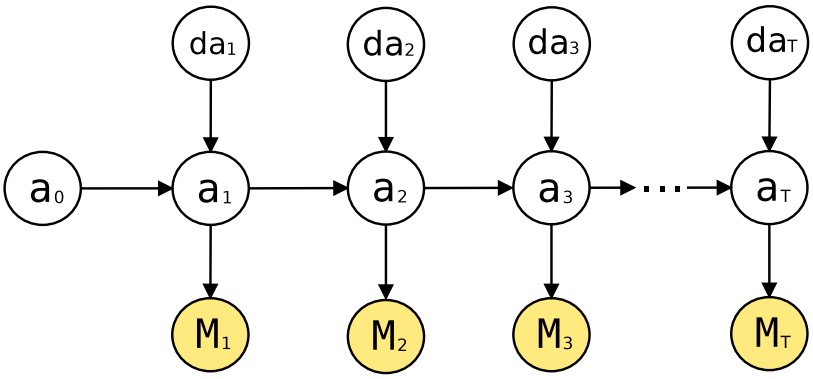

Figure 4.17: A simple constant crack growth model.

$$\begin{cases} a_0 \sim Normal(\mu_{a_0}, \sigma^2_{a_0}) \\ da_t \sim Normal(\mu_{da}, \sigma^2_{da}) \\ a_t = a_{t-1} + da_t \\ M_t \sim Normal(a_t, \sigma^2_{\epsilon}) \end{cases} \tag{4.28}$$

Thus, this network can be transferred into a standard Bayesian linear regression problem. For $i = 1, 2, \ldots, n (n \leq T)$, the conditional distribution of M_i given a set of explanatory variables $\boldsymbol{\phi_i^\intercal} = (\phi_{i0}, \phi_{i1}, \phi_{i2}, \phi_{i3}, , \phi_{iT})$ can be specified as

$$M_i = \boldsymbol{\phi_i^\intercal} \mathbf{da} + \epsilon_i \tag{4.29}$$

Where $\mathbf{da}$ is a $(T+1) \times 1$ vector and ϵ_i is a normally distributed variable with a mean of 0 and standard deviation of σ_ϵ, representing the measurement error. The objective is to find the posterior distribution of the actual crack size a_{pred} by providing the life cycle measurement data sets $(\mathbf{\Phi}, \mathbf{M})$. Here $\mathbf{\Phi}$ is a $(T+1) \times n$ matrix and $\mathbf{M}$ is a $n \times 1$ vector. Since all these nodes are currently assumed to satisfy the normal distribution, the exact solutions can be obtained for the rest of the nodes, which are also all normally distributed. The posterior distribution of $\mathbf{da}$ is shown from

Eq. (4.30) to Eq. (4.31) and the predictive distribution of a_{pred} is shown in Eq. (4.32).

$$P(\mathbf{da}|\mathbf{\Phi},\mathbf{M}) \propto P(\mathbf{M}|\mathbf{da},\mathbf{\Phi})P(\mathbf{da}) = Normal(\mathbf{da}|\boldsymbol{\mu_N},\boldsymbol{\sigma}_{\boldsymbol{N}}^{T}) \tag{4.30}$$

where $\boldsymbol{\mu_N} = \boldsymbol{\sigma_N^2}((\boldsymbol{\sigma_0^2})^{-1}\boldsymbol{\mu_0} + 1/\sigma_\epsilon^2\mathbf{\Phi M})$ and $\boldsymbol{\sigma_N^2} = ((\boldsymbol{\sigma_0^2})^{-1} + 1/\sigma_\epsilon^2\mathbf{\Phi\Phi}^T)^{-1}$. Both $\boldsymbol{\mu_0}$ and $\boldsymbol{\sigma_0^2}$ are $(T+1)\times(T+1)$ diagonal matrix with

$$\begin{cases} (\boldsymbol{\mu_0})_{11} = \mu_{a_0} & (\boldsymbol{\mu_0})_{jj} = \mu_{da} \\ (\boldsymbol{\sigma_0^2})_{11} = \sigma_{a_0}^2 & (\boldsymbol{\sigma_0^2})_{jj} = \sigma_{da}^2 \end{cases} \text{ for } t = 1,2,3,\ldots,T \tag{4.31}$$

The predictive distribution of a_{pred} given $\boldsymbol{\phi}_{\boldsymbol{pred}}^{\intercal}$ becomes

$$\begin{aligned} P(a_{pred}|\mathbf{\Phi},\mathbf{M},\mathbf{da}) &= \int P(a_{pred}|\mathbf{da})P(\mathbf{da}|\boldsymbol{\phi}_{\boldsymbol{pred}}^{\intercal},\mathbf{M})d(da) \\ &= Normal(a_{pred}|\boldsymbol{\phi}_{pred}^{\intercal}\boldsymbol{\mu_N},\boldsymbol{\phi}_{pred}^{\intercal}\boldsymbol{\sigma}_N^2\boldsymbol{\phi}_{pred}) \end{aligned} \tag{4.32}$$

The parameters of this model are summarized in Table 4.8. To avoid negative values of da_t and a_t, the mean value of initial crack size and da chosen is relatively large.

Table 4.8: Parameters of constant crack growth model.

Variable	Distribution	Mean	Standard Deviation
da_t(mm)	Normal	1	0.3
a_0(mm)	Normal	7	3
M_t(mm)	Normal	a_t	2
l_c(mm)	Deterministic	30	–

The network is configured to have 20 slices, representing 20 time steps. Of these 20 time steps, three pairs of measurement data are provided as follows: $m_5 = 10$ mm, $m_{10} = 14$ mm and $m_{15} = 25$ mm. The reliability index must be estimated for a_t node which contains both smoothing ($t \leq 15$) and prediction ($15 < t \leq 20$) ranges. The Bayes Net Toolbox (BNT) (*Murphy*, 2001) for Matlab efficiently provides the posterior solutions and is used here as the inference engine. To begin with the proposed algorithm, the initial discretization must be generated for da_t, a_t, and M_t nodes,

which is summarized in Table 4.9. The initial number of intervals should be as small as possible while the range of intervals should cover the whole probability domain, especially the low probability tail region. For the discretization of a_t, l_{max} denotes the boundary of the last bin where only one boundary exists. Here, $l_{max} = 60$ mm is chosen which satisfies Eq. (4.26).

Table 4.9: Initialization of nodes for constant crack growth model.

Variable	Number of States	Discretization
da_t(mm)	4	$[0 : 5/3 : 5, +\infty]$
a_t(mm)	5	$[0 : l_c/3 : l_c, l_{max}, +\infty]$
M_t(mm)	4	$[0 : l_c/3 : l_c, +\infty]$

The discretization results at 13 iterations are shown in Fig. 4.18, demonstrating the results of applying the method presented in Section 4.5.3. The number of intervals for the da_t, a_t and M_t nodes increase to 111, 146, 96, respectively. For the a_t node, dense intervals have been generated between approximately 20 mm and 35 mm, where the posterior distribution of a_t is higher than the rest of the region and contributes significantly to the POF. Similar results occur for the region of the da_t node between 1.1 mm and 1.5 mm. Conversely, when a_t is above or below that region, the interval size is larger, indicating that either a smaller posterior probability region or a smaller contribution on the POF. Similarly, relatively coarse discretization has also been generated for the da_t node where crack increment is large and for the M_t node when crack size is small. Therefore, it is evident that the RPDD algorithm has the ability to adjust the discretization accordingly and distinguish the different contributions for the reliability calculation according to the posterior distribution.

To demonstrate the accuracy and efficiency of the proposed algorithm, static uniform discretization has also been applied with the same number of intervals for all nodes in every time step and iteration. The error of reliability index ε_β output is then calculated for both discretizations according to Eq. (4.27), which is shown in Fig. 4.19. It is evident that, when starting with the same error level, the error of the

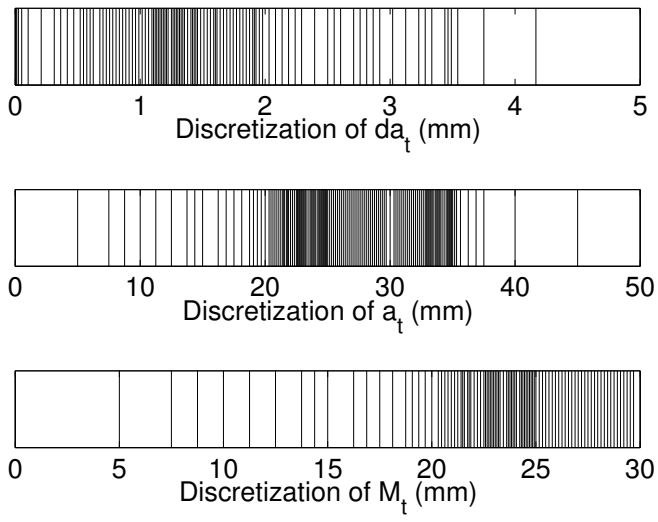

Figure 4.18: The discretization of da_t, a_t and M_t at 13 iterations.

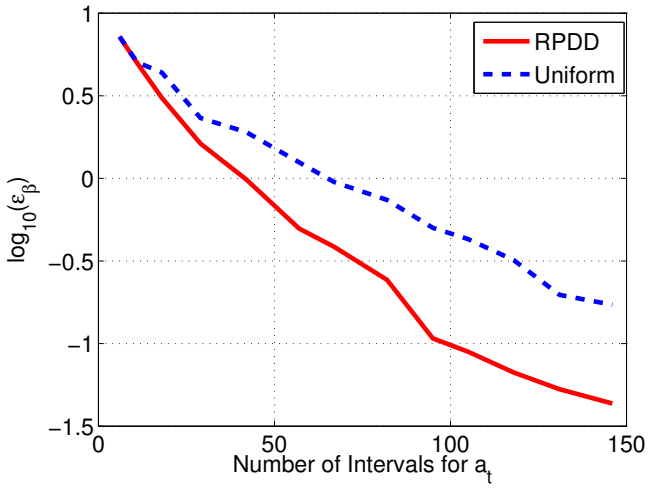

Figure 4.19: The comparison of error between RPDD algorithm and uniform discretization.

RPDD algorithm is reduced much faster when the number of intervals increases. The reliability index after 13 iterations of the RPDD algorithm is then compared with the exact solution shown in Fig. 4.20. The reliability output is shown to already be highly accurate and sufficient for engineering prediction purposes.

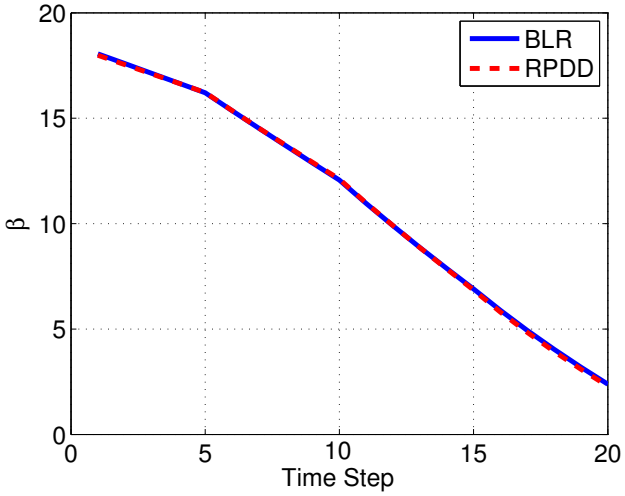

Figure 4.20: The comparison of β between exact solution and RPDD at 13 iterations.

4.5.4.3 A stochastic crack growth model

Straub's stochastic crack growth model (*Straub*, 2009) is based on *Yang and Manning* (1996)'s method, where the crack growth rate is expressed by a lognormal random process. The expression is shown in Eq. (4.33).

$$a_t = [\left(1 - \frac{m}{2}\right) CX_tY(a_{t-1})^m \Delta S^m \pi^{\frac{m}{2}} n + a_{t-1}^{1-\frac{m}{2}}]^{\frac{1}{1-\frac{m}{2}}} \tag{4.33}$$

The variable a_t is the crack size at time step t, C and m are the material constants, Y is the geometric function relating the stress intensity factor to current crack length, ΔS is the range of cyclic stress applied to the crack, and X_t is a stationary lognormal random process with a median value of 1.0 and a standard deviation σ_X. The lognormal random process X_t can be further characterized by its auto-covariance function. This function defines the deviation from median crack growth relationship

owing to material and model imperfections. In general, the auto-covariance function of the crack growth rate should decrease as the interval of two time instances t_1 and t_2 increases. Thus, an exponential form of auto-covariance function with standard deviation function of σ_X was proposed by Yang and Manning as follows:

$$\mathrm{Cov}[X_{t_1}, X_{t_2}] = \sigma_X^2 exp(-\alpha_X |t_2 - t_1|) \tag{4.34}$$

Within this function, α_X is the measure of correlation time for $X(t)$. Therefore, a parametric crack growth model under a discrete time step can be expressed in a generic form of

$$a_t = f(a_{t-1}, n, X_t, \sigma_X, \alpha_X) \tag{4.35}$$

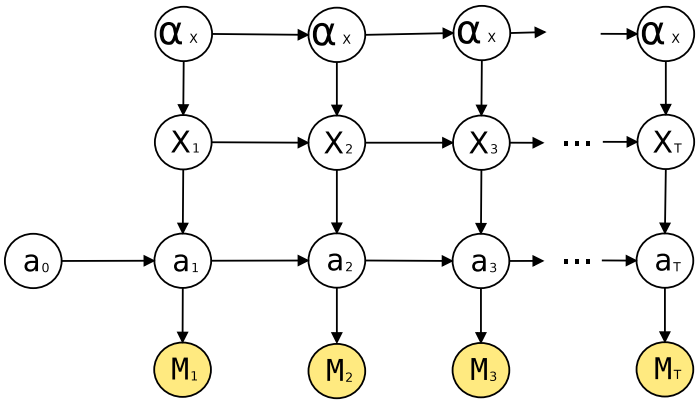

Figure 4.21: A stochastic crack growth DBN model.

A corresponding stochastic crack growth DBN model is proposed accordingly in Fig. 4.21. The number of cycles has been divided into an equal number of steps with T time steps in total. α_X and X_t are hyperparameters, a_t and M_t are the same in the previous example. The details of this model can be found in *Straub* (2009)'s paper.

The crack for this example is assumed to be an edge crack growing into a finite width plate, a well-studied problem with similarities to many crack growth problems in ship and offshore structures. The plate has dimensions of 200 mm $\times$ 100 mm ($b = 100$ mm, $2h = 200$ mm) with plane strain conditions assumed. The material is assumed to be pure elastic with Young's modulus $E = 73.1$ MPa. A constant

amplitude cyclic stress is applied on both sides of plate with $S_{max} = 60$ MPa and $S_{min} = 0$ MPa. An initial edge crack with length $a_0 = 1$ mm is formed at the mid-height of the plate. Three inspections are performed for total of 50 time slice: which result in crack measurements of $m_{10} = 1.4$mm, $m_{20} = 2$mm, $m_{30} = 5$mm. The parameters of this model and the initial discretization are summarized in Table 4.10 and Table 4.11, respectively. To reduce the approximation error from the one boundary interval, according to Eq. (4.26), the two boundary intervals of the a_t node range from 0 to plate width b instead of l_c in *Straub* (2009)'s paper. A small number of states are given for this initial discretization. In this example, a large measurement error is used, which increases the uncertainty of the POF at each time step. In reality, if the inspection data is available at time step t and measurement technique is sufficiently accurate, the reliability estimation before time step t can be neglected.

Table 4.10: Parameters of the stochastic crack growth model.

Variable	Distribution	Mean	Standard Deviation	Auto-covariance
α_X(cycle)	Lognormal	1E4	1E4	–
X_t	Logormal	1.2	0.8	Eq. (4.34)
a_0(mm)	Exponential	1	1	–
M_t(mm)	Normal	a_t	5	–
ΔS(MPa)	Deterministic	60	–	–
C	Deterministic	5.85E-14	–	–
m	Deterministic	3.59	–	–
l_c (mm)	Deterministic	60	–	–
n(cycle)	Deterministic	1E4	–	–

Table 4.11: Initialization of nodes for stochastic crack growth model.

Variable	Number of States	Discretization
α_X(cycle)	4	$0, 10\text{^}[1:5/(4-1):6]$
X_t	4	$[0:(15-0)/(4-1):15]$
a_t(mm)	6	$0, \exp[\ln(0.01):(\ln(l_c)-\ln(0.01))/(6-3):\ln(l_c)], b, +\infty$
M_t(mm)	5	$0, \exp[\ln(0.01):(\ln(l_c)-\ln(0.01))/(5-2):\ln(l_c)], +\infty$

The discretization results after 16 iterations have been shown in Fig. 4.22. The

number of intervals for α_X, X_t, a_t, and M_t are 18, 68, 148, 147, respectively. Based on the figure, it is evident that the nodes of a_t and M_t generally maintain a logarithmic discretization, as the crack size grows exponentially with an increase in the number of cycles. Fewer intervals are generated by the RPDD algorithm for the nodes of α_X and X_t since those parameters are less sensitive to the a_t node and maintain a very similar distribution within different time steps.

Since the exact solution is not available for this model, fine discretization is generated using Straub's logarithmic static discretization for comparison. The logarithmic static discretization uses the same discretization method as shown in Table 4.11, but the number of intervals used for each node is increased gradually until the reliability output is stationary. The final number of intervals for the α_X, X_t, a_t and M_t have been increased to 150, 265, 318 and 318, respectively. The error of the RPDD algorithm is then compared to the static discretization using both uniform and logarithmic discretization at each iteration, which is shown in Fig. 4.23. This demonstrates that, when starting from the same error level, all three discretization methods generally reduce their errors until they maintain a certain level; however, the uniform discretization performs the worst among all three methods. For the RPDD algorithm, initially the error drops slower than the logarithmic discretization before approximately 20 intervals of the a_t node. This is because, at each iteration, a subdivision occurs at the middle of each interval, while the logarithmic discretization allocates more effort to small crack sizes, which is closer to the optimum discretization. When the number of intervals at a_t node is above 20, the RPDD algorithm performs much better and takes only about 50 intervals of a_t to reach the lowest error, while the logarithmic algorithm takes almost 150 intervals to reach the same level error. After that, the error of the RPDD remains stable, which indicates the dominance of other types of discretization errors at that stage. The reliability index after 16 iterations for the RPDD algorithm is then plotted in Fig. 4.24.

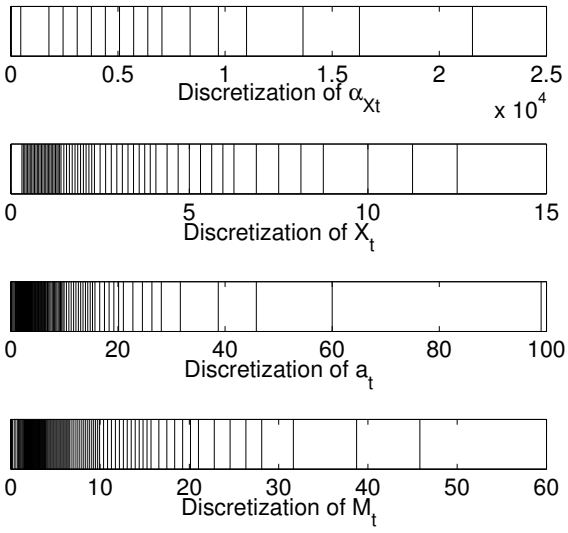

Figure 4.22: The discretization of α_{Xt}, X_t, a_t and M_t at 16 iterations.

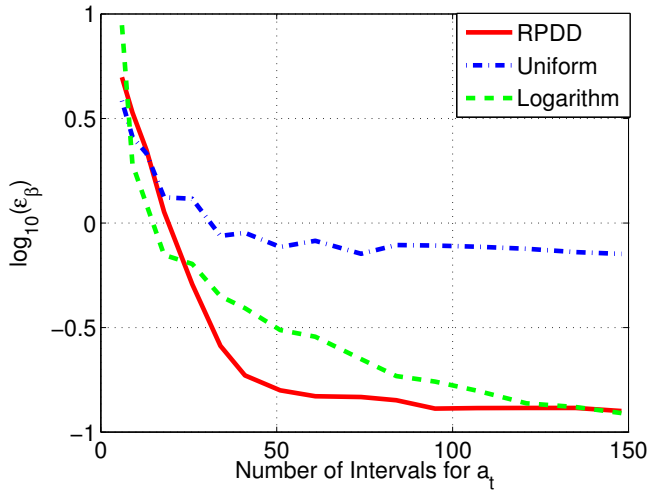

Figure 4.23: Error comparison between RPDD, uniform and logarithmic discretization vs. dense solution.

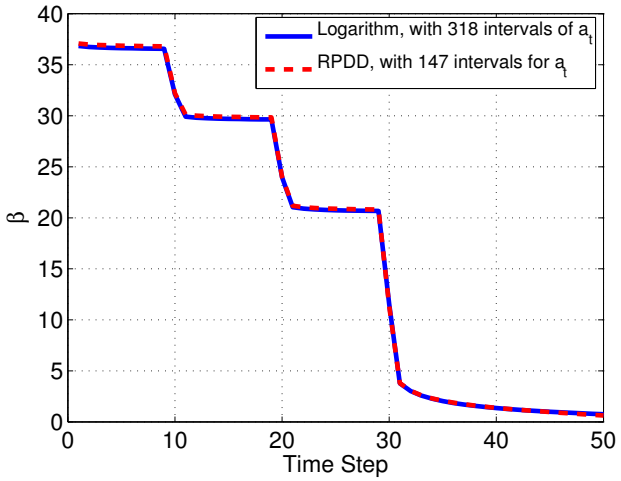

Figure 4.24: The comparison of β between fine discretization and RPDD at 16 iterations.

While the focus of this work has been to effectively discretize the DBN for probability of failure calculations, it is interesting to investigate if the initial crack size distribution is well-resolved by this approach. In fracture mechanics-based life prediction, the initial crack size is a highly important parameter, but difficult to estimate at the design stage (*Cohen et al.*, 2011; *Sankararaman et al.*, 2010) as it depends on a host of material and fabrication parameters. As shown in Fig. 4.25, the initial crack size distribution with the RPDD algorithm is broadly similar to the initial crack size distribution obtained by the fine discretization case. Particularly, when the CDF is between 0.9 and 1, that distribution is consistent with a fine discretization case. The proposed algorithm has concluded that this region is more critical to the accuracy of reliability output in future time steps, as large initial crack sizes are likely to result in cracks growing about l_c. This result indicates that the RPDD approach is concentrating the accuracy of the discretization in the areas viewed as critical to the limit state. If no evidence of a crack is seen during inspections, an alternate discretization approach may be needed if the objective of the smoothing approach is to update the initial crack size distribution vs. update the probability of failure. This might involve

further refining the whole discretization by increasing the number of states or certain related regions.

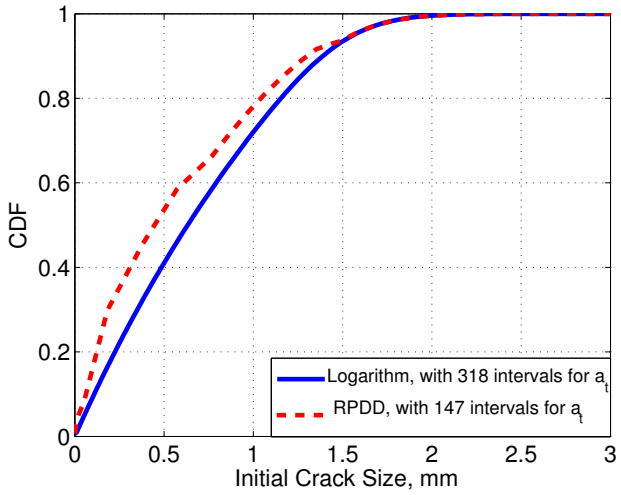

Figure 4.25: The initial crack size CDF distribution.

4.5.5 Summary

In summary, a new iterative discretization algorithm was presented for more accurate and efficient reliability evaluations of deteriorations processes modeled with DBN. A new reliability purposed dynamic discretization algorithm was developed that separates the error analysis into two stages, smoothing and prediction, and subdivides the discretization intervals iteratively according to the reliability contribution from each intervals. The proposed techniques were compared with static discretization in two crack growth examples. Both examples illustrated the robustness and efficiency of the proposed algorithm. Generally, the results show that the proposed algorithm can achieve the same accuracy level as the static discretization which using less than half the number of intervals. Also, it avoids the need to manually iterate through different static discretization methods and resolution levels to achieve convergence. Moreover, this algorithm can be applied to the inference of initial crack size distribution, which gave an accurate estimation of initial crack occurrence probability at the

"tail region". In spite of the significant potential of this algorithm, the accuracy of reliability estimation is still highly sensitive to the generation of CPTs. The method of CPTs generation was improved based on Straub's method. The proposed method removes the need for complex numerical integration of each bin. An exploration of the method's ability to handle other types of structural reliability applications in addition to crack growth should also be considered in future research.

4.6 Conclusions

A stress life based fatigue management approach was proposed first in this chapter, followed by a fracture mechanics based management approach. Both of approaches have their pros and cons: the stress life based approach can manage multiple cracks with a single set of parameters, however, the crack is only evaluated by pass-fail metric and no actual size information can be provided. While the fracture mechanics based approach can predict the actual crack size, however, only one crack's detail was explored so far. For the fracture mechanics based approach, a reliability purposed adaptive discretization was proposed which focuses on an accurate reliability estimation with fewer discretizations. Two examples were given and results were compared with traditional static discretization, which was proved to be more accurate and efficient.

CHAPTER V

CASE STUDY

5.1 Introduction

This chapter presents a methodology for XFEM-aided fatigue life updating by using Bayesian approaches. A new SHM concept is proposed that integrates the proposed life-time load updating methodology as well as the dynamic discretization scheme for reliability-purposed life updating. This concept relies on all of the developments described in previous chapters. Both the hogging and sagging bending moment are updated, both of which are combined into the stress range distribution. A ship structure type panel is then applied as an example to predict the crack growth rate with all SHM information. The proposed RPDD algorithm is also used with stress intensity factor being computed for the first time by XFEM technique.

As illustrated in the previous chapter, a load updating strategy can be applied first in order to predict lifetime load distribution by using the synthetic loading from LAMP. Then a crack growth Bayesian model can then be constructed so as to incorporate crack size inspection record. With the help of the proposed RPDD, an accurate reliability prediction can be obtained. Two types of SHM information are utilized: Collected VBM information during the vessel operation as well as corresponding sea environment and operational profiles and the crack inspection records.

A stiffened panel with a given initial crack on the upper deck of JHSS mid-section

will be used as an example. An XFEM technique will be applied in order to simulate the crack propagation process and to compute the stress intensity factor, as the analytical approximation of stress intensity factor is generally unknown. The major advantage of XFEM compared to the conventional FE method is that it avoids the re-meshing during the crack propagation. This makes a direct cycle-by-cycle fatigue simulation possible at greatly reduced the computational cost. Details of this technique can be found in Appendix A. Stress intensity factors will be extracted and scaled according to the updated load level in each cell. At this point, both load information and crack inspection results can be combined for the fatigue reliability updating.

5.2 Extended finite element aided fatigue life updating by using Bayesian approaches

5.2.1 Update lifetime load range distribution

Since the cyclic stress range is more important than stress peaks for fatigue life calculation, both hogging and sagging moment peak distributions must to be updated based on observed cells. Whereas in Chapter Three all the cells were re-predicted whether or not they were observed, this chapter uses peak distribution from cell-based updating for those observed cells in order to construct lifetime load distribution, and applies the same load updating strategy for those unobserved cells. Although, it is possible to utilize SHM data directly for observed cells, the data size should be large enough to facilitate smooth peak prediction, especially for low probability events.

Since the methodology for updating sagging moment peak distribution was presented in Chapter Three, only the methodology for hogging moment updating and constructing the stress range will be explained below. The procedure for hogging moment updating is very similar to the sagging moment update, however, only two

hyperparameters will be considered: a scaling factor k and bandwidth correction term χ. The skewness factor μ_3 can not be applied for hogging moment updating, as μ_3 is less than zero, yielding a non-monotonic transformation. A stress range distribution will be conducted according to both the obtained sagging and hogging moment.

Following the procedure outlined in Chapter Three, the hogging peak points have been extracted from those observed cells with data simulated by LAMP. By using three proposed two level updating strategy, the re-predicted CDF hogging distribution is then compared to the original data via the EMD error as shown in Fig. 5.1. Since there is no skewness hyperparameter, only case I, II, and III listed in Table 3.4 have been run. Similar with Fig. 3.8, all three cases show a steady decrease in error with increased number of observations, although small fluctuation occurs in case I II.

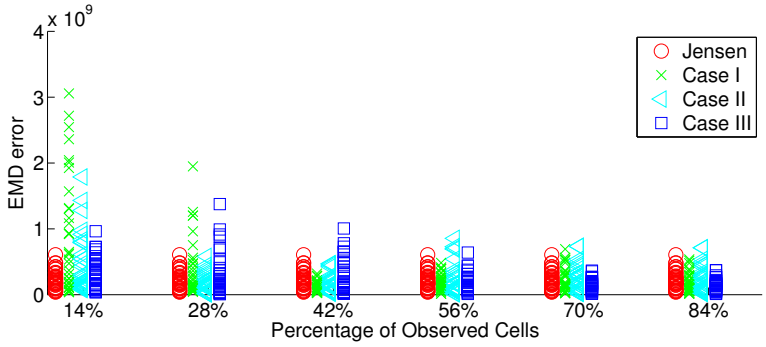

Figure 5.1: The EMD error for hogging CDF distribution.

Lifetime hogging peak CDF distribution for selected observation levels is also plotted in Fig. 5.2 to allow comparison with Fig. 3.9, which shows lifetime sagging peak distribution in specific. As indicated by EMD error, however, improvement can be seen when compared to Jensen's method, all those three cases perform worse than the sagging peak prediction shown in Fig. 3.9. This may be because the number of hyperparameters for hogging cases is smaller than the number for the sagging cases which makes the CDF prediction less flexible in adjusting itself to fit the original data.

The VBM range is then obtained for the fatigue loading calculation by combining

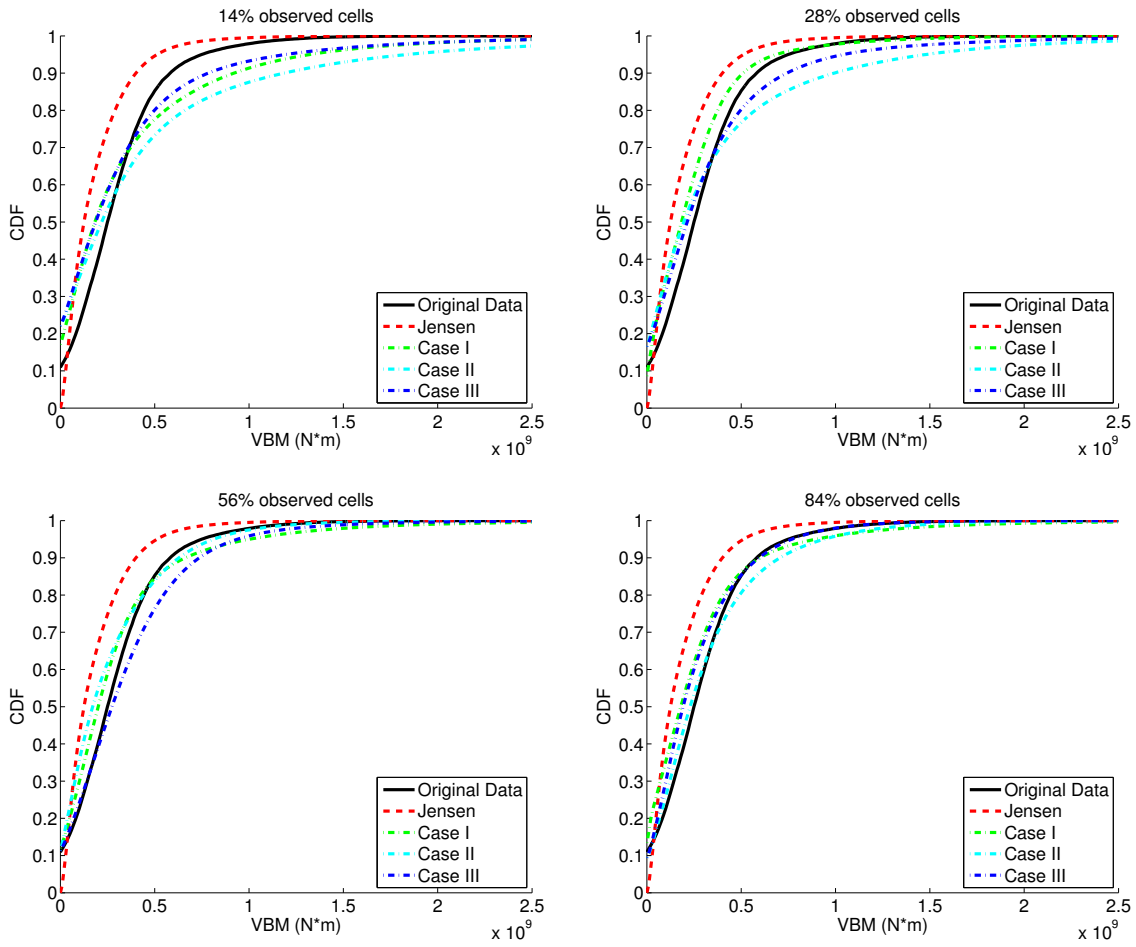

Figure 5.2: Lifetime hogging bending moment CDF prediction with different observed cells.

both sagging and hogging moments. If we assume that hogging and sagging distributions are independent of each other, then VBM range distribution can be calculated by combining both sagging and hogging distribution with convolution integral. A discretized form of convolution is expressed below.

$$\begin{aligned} P_r(M=m) &= (P_{sag} * P_{hog})(M=m) \\ &\approx \sum_{n=-\infty}^{\infty} P_{sag}(M=n) \cdot P_{hog}(M=m-n) \end{aligned} \tag{5.1}$$

where n is the index that covers all possible events of distribution. In order to obtain the lifetime moment range distribution, the convolution integral has to be performed within every cell and then lifetime range distribution can be constructed according to the probability of occurrence for each cell. Fig. 5.3 shows the results for this by comparing different observation levels. As mentioned above, when certain cells are observed, only cell-based prediction will be used. The results in Fig. 5.3 shows that when about 28% of cells are observed, all three cases possess sufficient accuracy to predict the original data; when 84% of cells are observed, all of the above mentioned methods are almost consistent with original data.

5.2.2 Model the stiffened panel by using XFEM

XFEM is an alternative method to the finite element method that allows for discontinuities to be incorporated into the element definition in order to model flaws in the structures such as cracks, voids and inclusions. When coupled with so-called level set method, the XFEM technique enables the FE to capture the discontinuities during the crack propagation without any remeshing. A detailed description of XFEM is available in the Appendix A.

A stiffened panel on the upper deck of JHSS (*Okasha et al.*, 2010a) mid-section has been chosen as our example. Three stiffeners, which enable easy model extention, especially with the XFEM technique, are modelled in Abaqus with an embedded

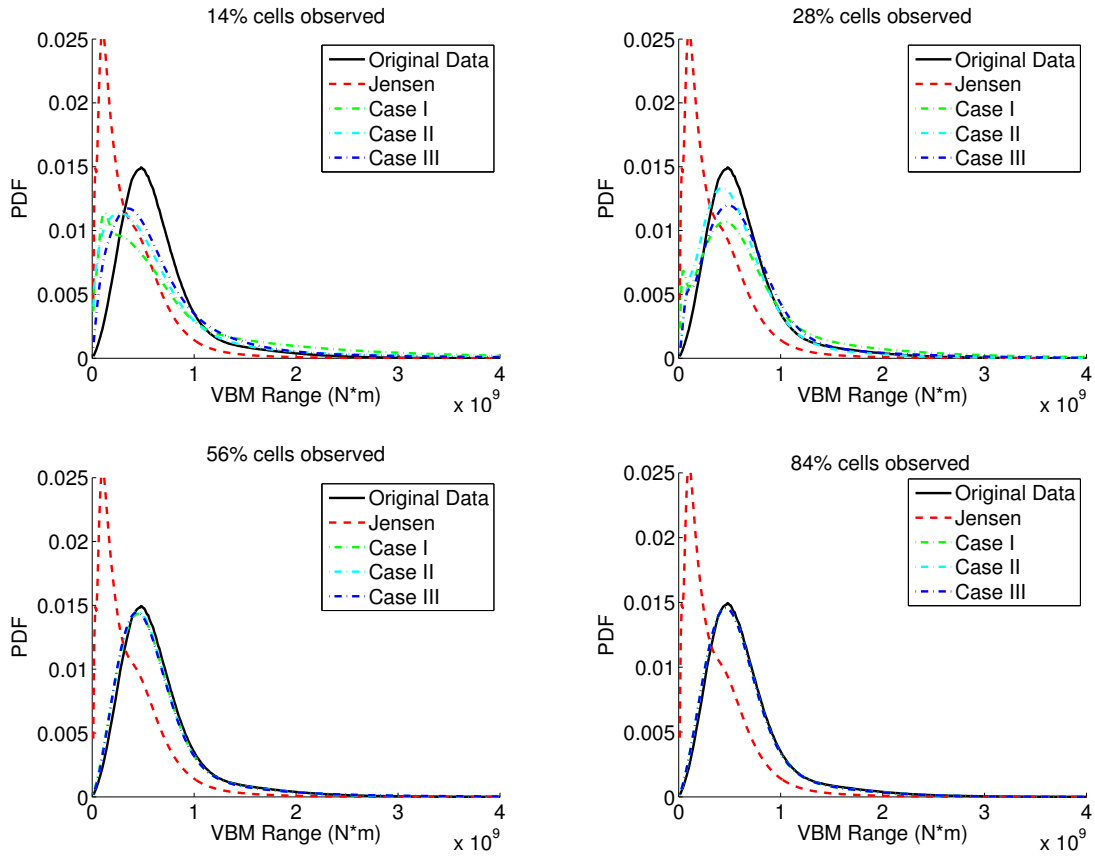

Figure 5.3: Lifetime VBM range distribution for one cycle with different observed cells.

XFEM package being provided. A initial quarter-circle edge crack with 3 mm radius is assumed starting from flange at the middle stiffener. A fine mesh is applied around the initial crack as well as the potential crack propagation region; while a relatively coarse mesh is applied on the region farthest from the crack. A triangular mesh is applied on the transitional region. A fixed boundary is applied on one end of the plate, while a 138 MPa uniform load has been applied on the other side of the plate. The load amplitude is chosen according to design maximum bending moment during vessel operation and the results can be scaled according to actual load level, since a linear elastic analysis is performed. As XFEM enables the crack growth with consistent mesh, a python script has been written to simulate the crack propagation process. For each iteration, the stress intensity factor is calculated first by XFEM around the crack front; normal direction to the crack front is also decided. The growth direction of the crack for the next iteration is assumed to be normal according to the current crack front and the distance is controlled by the maximum allowable crack growth size which is defined at the beginning of the simulation. The number of cycles experienced is then recorded according to the Paris' law. Generally, the smaller the maximum allowable crack growth size is, the more accuracy and robust the simulation will be. However, this will increase computational cost, as it increases the number of Abaqus solutions. Fig. 5.4 shows an example of crack growth when the crack is on both the flange and web as well as primary stress contour plot around the crack.

Fig. 5.5 shows crack growth on the stiffened panel with a logarithm of the number of cycles experienced towards the next crack front specified above. Since the crack front is a two-dimensional curve, crack length is calculated as the summation of the length in the flange, web, and plate. Crack length and crack area percentage versus number of cycles are both plotted in Fig. 5.6 with the total length and total area being defined as $bf + hw + 2B$ and $bf \times tf + hw \times tw + 2B \times tp$, respectively. It can be seen from Fig. 5.6 that under current load level, crack growth rate is generally small

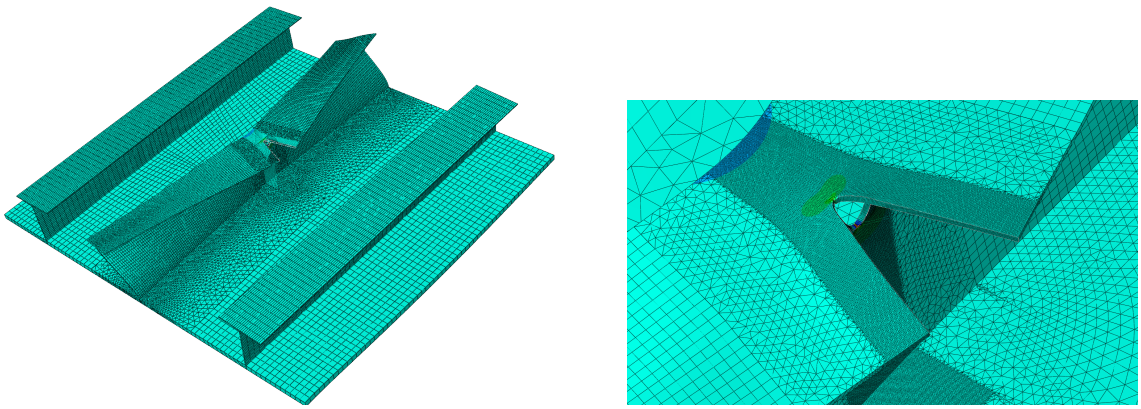

Figure 5.4: Example of XFEM model when crack is on both flange and web(left) and corresponding contour plot of primary stress in the direction of stiffener (right).

when the crack is still on the flange. If it propagates to the web and plate, crack growth rate increases significantly. As shown in Fig. 5.7, the stress intensity factor is then transferred to the geometric function with respect to crack length by using Eq. 4.13. The data is divided into two regions according to the transitional area where the crack goes into the plate and the stress intensity factor jumps. Two smoothing splines are constructed for these regions. Only the parameters of the fitted spline are stored in order to predict the stress intensity factor for different crack lengths.

5.2.3 Update fatigue reliability

Updated load information is then incorporated into a DBN-based stochastic fatigue crack growth model. In order to study the effect of the incorporation of both load and crack inspection information, we assume that the vessel has been in service for two years with half of this time spent in head sea and following sea conditions. (Beam sea condition is neglected.) Therefore, the number of cycles encountered during every year can be approximated according to expected encountering frequency. A stochastic crack growth model has then been constructed according to the interval time of a half year. The calculated number of cycles per half year is $\Delta N = 3.67E5$.

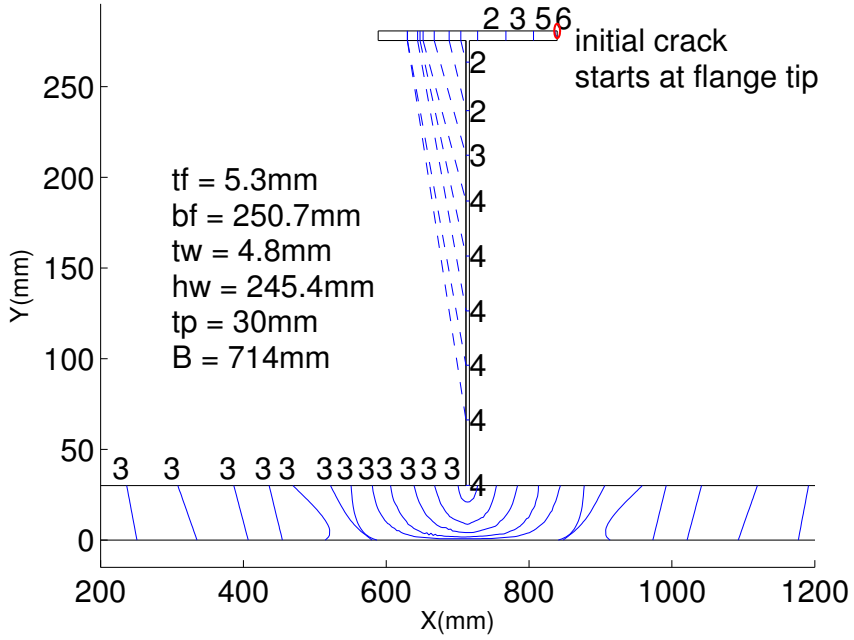

Figure 5.5: Crack front on the stiffened panel using XFEM.

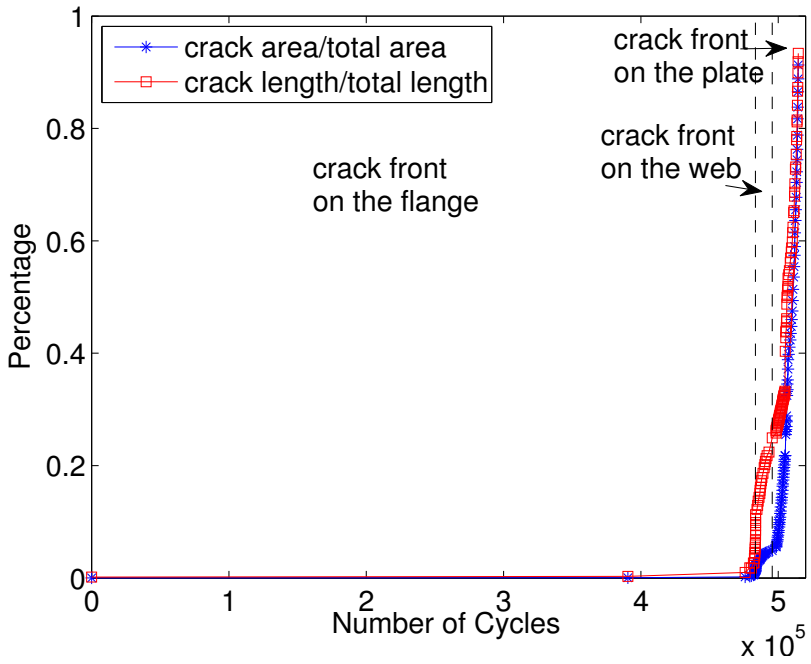

Figure 5.6: Crack growth on the stiffened panel using XFEM.

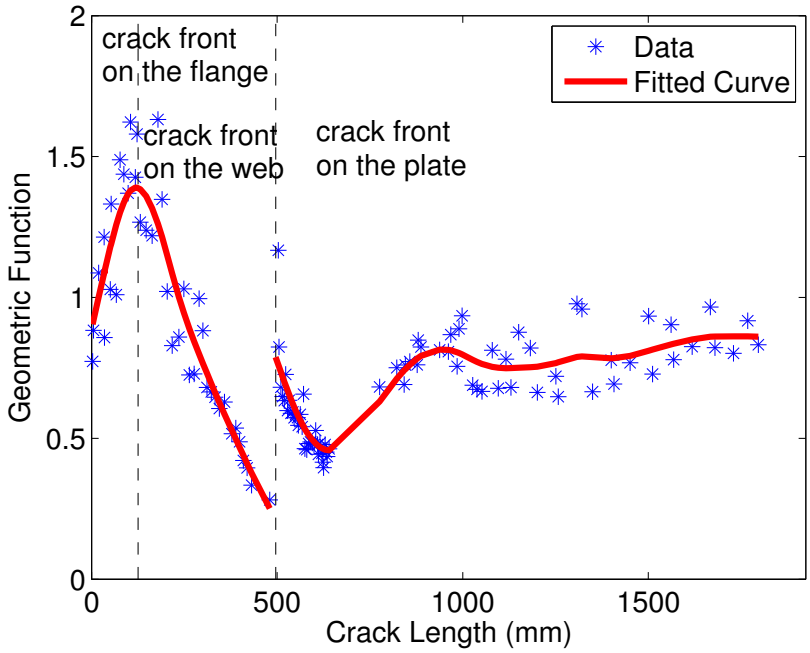

Figure 5.7: Geometric function vs. crack length.

In contrast to the model in Fig. 4.21, where a deterministic stress range value is given, here the input is the half year expected stress distribution. To calculate this distribution, the convolution integral has been performed ΔN times; results are given in Fig. 5.8 for different observation percentages. Because loads have already been updated in the load updating strategy, it is assumed they will not be updated again in the crack growth model from crack inspection records. Therefore, the updated load distributions will be directly incorporated into the CPD generation, while no extra nodes will be added into the DBN model.

The stochastic crack growth model of *Straub* (2009) shown in Fig. 4.21 has been applied again, as has the proposed reliability purposed dynamic discretization. The parameters of this model are summarized in Table 5.1. The updated load distribution is chosen from Fig. 5.8 with 56% of the cells observed. According to Fig. 5.6, when the crack front reaches the bottom plate, the crack grows much faster and takes very few cycles to propagate through the plate. Therefore, failure has been defined in

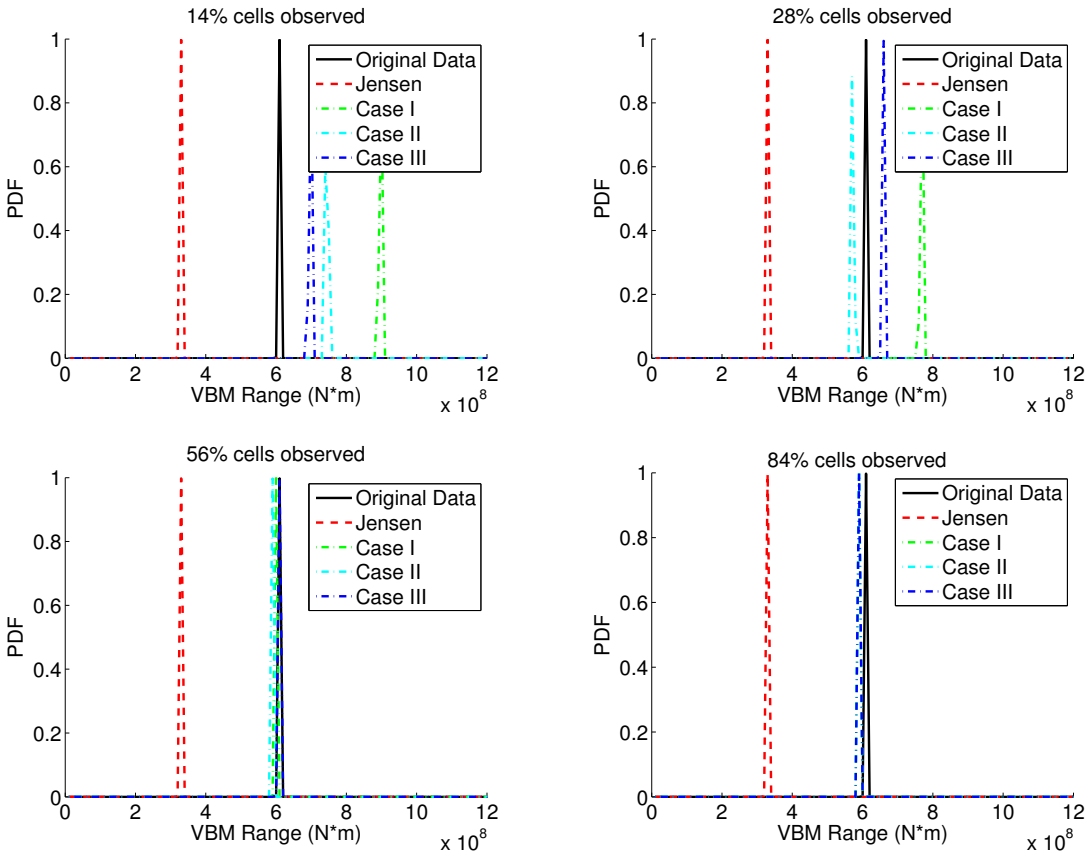

Figure 5.8: Lifetime VBM range distribution for N cycles with different observed cells.

terms of a critical crack size of $b_f + h_w$ when the crack front reaches the bottom plate. Inspection records assumes that there is a crack being inspected at the year two with a length of 50 mm.

Table 5.1: Parameters of the stochastic crack growth model.

Variable	Distribution	Mean	Standard Deviation	Auto-covariance
α_X(cycle)	Lognormal	1E5	1E5	–
X_t	Logormal	1.2	0.8	Eq. (4.34)
a_0(mm)	Exponential	3	3	–
M_t(mm)	Normal	a_t	3	–
C	Deterministic	2.18E-13	–	–
m	Deterministic	3.00	–	–
l_c (mm)	Deterministic	496.1	–	–
n(cycle)	Deterministic	3.67E5	–	–
ΔS(MPa)	Stochastic	Satisfy the distribution in Fig. 5.8, assume 56% cells observed		

The results for crack size distribution with and without crack inspection records are shown in Fig. 5.9. Original data represents the load simulated from LAMP and Jensen's method represents the design stage load prediction. The upper figure shows the crack size distribution without any inspection updating, while the bottom figure shows the crack size distribution with the inspection updating. Since the design stage load prediction generally under-predicts the observed loading level, crack size that includes the updated stress range is larger than the design prediction. It is also the case that with inspection updating, standard deviation of future crack prediction decreases significantly. The reliability index with and without crack inspection updating has also been plotted in Fig. 5.10. Again, design stage prediction generally underestimates the probability of failure. Even with the inspection updating, the predicted reliability index is still far away from the true value, which implies that significant errors exist in both load and crack growth model. For those updated load cases, if only load has been updated, the β becomes much closer to the actual value compared with design stage prediction. This implies that the error from loading has been removed and that the error from crack growth model becomes dominant. When

both load and inspected crack are both updated, the result is generally consistent with the true value in case I, II, and III. This implies that both load updating and crack inspection updating are necessary to ensure accurate reliability estimation. For this example, case I, II, and III are consistent with each other, but it is not the general case if a lower number of loading conditions are available.

5.3 Conclusions

This chapter demonstrated an SHM updating concept that considered both loading information and crack inspection. A load updating strategy and a DBN-based crack size updating model that utilized a proposed dynamic discretization technique were integrated. In order to determine updated stress range, a similar load updating strategy was applied to update both hogging and sagging bending moments. A stiffened panel on the upper deck of the JHSS mid-section was modeled. An initial edge crack on the flange was assumed and an Abaqus script was written to simulate the crack propagation process by using the XFEM technique. The geometric function under different crack size was also extracted. Then the load information and the geometric function of the crack sizes were incorporated for CPD generation of the DBN-based stochastic crack growth model. With the help of the proposed reliability purposed dynamic discretization technique, the reliability index was updated. The results show that for the proposed SHM framework, both load updating and crack inspection updating are necessary for accurate reliability estimation. The model errors are largely removed across case I, II, and III.

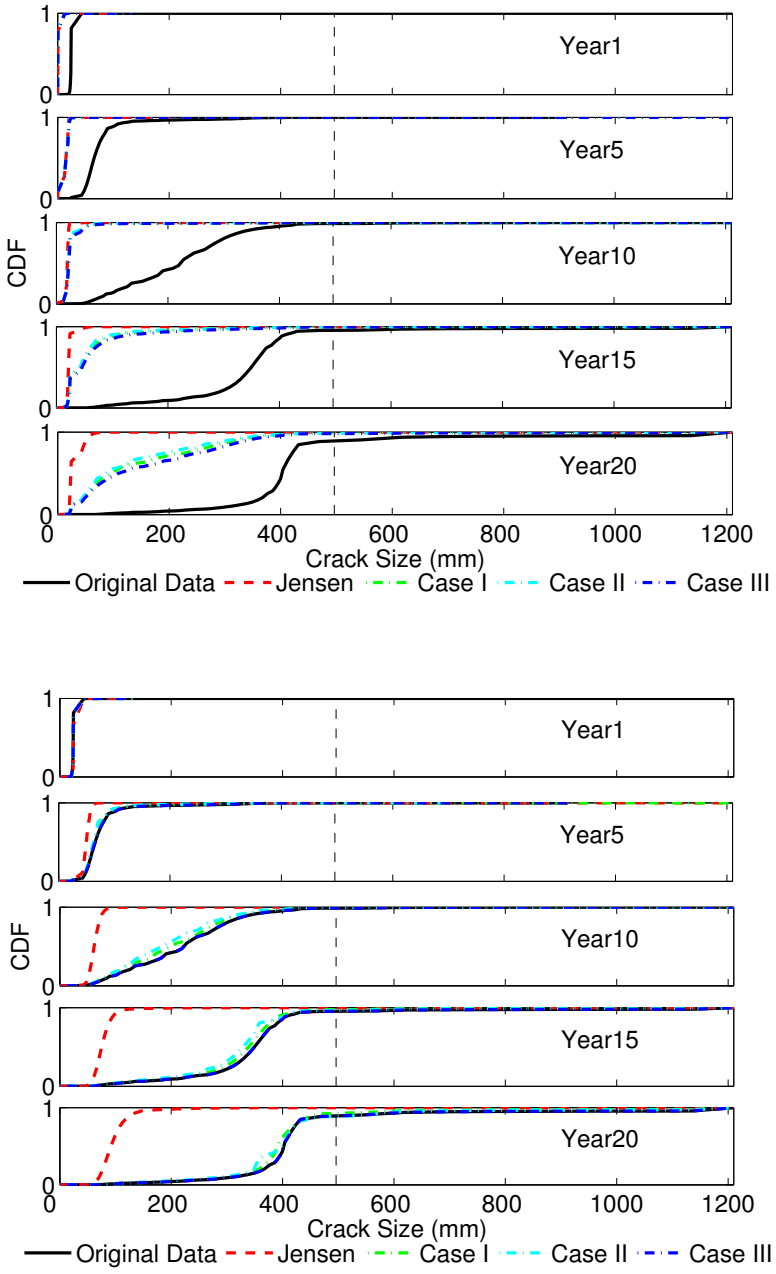

Figure 5.9: Crack size distribution at different years (upper: without any crack inspection result; bottom: with crack inspection result).

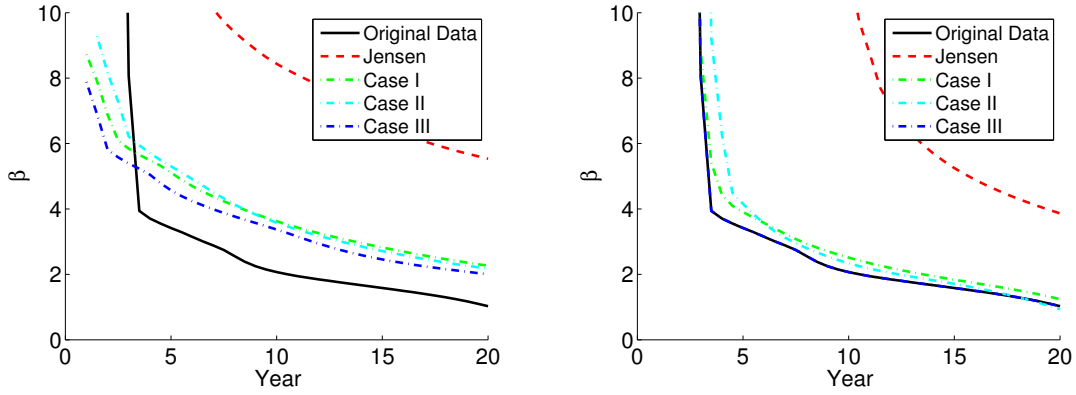

Figure 5.10: Reliability index at different years (left: without any crack inspection result; right: with crack inspection result).

CHAPTER VI

SUMMARY

6.1 Conclusions

The objective of this research was to construct an SHM framework using Bayesian techniques for accurate fatigue load and reliability estimation of high speed vessels. Fatigue life estimation for ships is generally subject to a significant amount of uncertainty because of the nature of the operational environment and hence the nature of structural loading as well as crack growth properties. Nevertheless, through inspection and monitoring, information such as crack location and size or wave and environmental conditions can be obtained which can potentially be used for successful fatigue management purpose. This research developed novel Bayesian updating techniques in order to incorporate such SHM data for the purpose of more accurate life prediction; this constitutes a powerful and flexible statistic based machine learning tool. Fundamental contributions were made in two areas: a load updating framework and a fatigue management framework. Different Bayesian updating techniques were developed accordingly.

A load updating framework was proposed in order to update the wave-induced vertical bending moment and was based on collected VBM measurements. The VBM is a major component of the fatigue loading. The ship's lifetime experience was firstly divided into many load cells with each cell corresponding to unique combinations of

sea state, vessel heading relative to the waves, vessel speed, and vessel condition. The framework was constructed by using a two-level updating strategy: cell-based updating was used to characterize every load cell by means of three hyperparameters, and a surrogate model was used to predict hyperparameters in those unobserved cells as well as peak cumulative distribution function. The proposed model also allows changing operational profiles and environments to be considered. A group of three updating parameters were selected to capture the impact of ship speed on the experienced loads, wave height on the skewness of the load distribution, and the bandwidth of the loading process. Three Bayesian learning approaches were explored: the continuous MCMC method, a discrete methods and a simple linear regression method. These methods were extended specifically to accommodate the probabilistic input data. Two updating models were also used: an empirical equation based model when empirical knowledge was available and a linear response surface model when empirical knowledge was not available.

Validation was performed first by using simulated data with assumed parameters. Therefore, the posterior distribution of parameters could be compared with true values. The results show that when observation data is limited, the empirical equation based model performs better than the linear response surface model, as the model is helpful in avoiding some unreasonable prediction. However, when additional observation data becomes available, the situation changes, since the empirical equation based model loses some flexibility to accommodate the real world data. This framework was further validated by using high fidelity LAMP simulation results as systematic structural health monitoring data. The lifetime wave load was predicted in terms of the different percentage of observed cells. The results prove that with increased observations, there is improvement in the accuracy of the vertical bending moment peak distribution, and when around 42% of data is observed, the proposed methods predict more accurately than the original predictions based on Jensen's simplified method.

Moreover, although the empirical equation based model has an "over-fit" issue when a large amount of data is observed, it still predicts the vertical bending moment distribution more accurately, which implies better accuracy in cells with a high probability of occurrence.

A fatigue integrity management framework was then developed to refine the fatigue life prediction and support the inspection planning and decision making by using SHM information. Two models were proposed according to different purposes: one is based on a design S-N fatigue approach and the other on a fracture mechanics approach. The S-N based approach collects the inspection information from multiple locations and uses MCMC to update fatigue parameters from local fatigue approaches. Two different methods of interpreting inspection results and predicting future fatigue performance were presented: a simple logit regression approach and a probit regression approach based on determining the overall life distribution factors. The results generally shows that when a sufficient amount of fatigue details have been investigated, the probit model, which more closely reflected the underlying statistical model used to generate the data, is better able to predict the future fatigue cracking of the vessel. The simple logit regression model produced reasonable results and generally performed the best when data was more limited, such as the one-frame inspection case.

Although the stress life based fatigue management approach is efficient to assess multiple fatigue spots, it only gives a simple pass-fail output and does not include any information about crack size. Therefore, a fracture mechanics based fatigue management approach which captures actual crack growth information is preferable. The DBN based deterioration process in *Straub* (2009) was extended first to model a two-dimensional crack growth process with both crack depth and crack length. The model was applied to a offshore mooring chain jack fatigue reliability updating problem. Then, the accuracy and efficiency of reliability estimation was further in-

vestigated. A new reliability purposed dynamic discretization (RPDD) algorithm was developed to separates the error analysis into two stages, smoothing and prediction, and subdivides the intervals iteratively according to the reliability contribution from each interval. The proposed techniques were compared with static discretization in two crack growth examples: a simple constant crack growth model where the analytical solution is available and a stochastic crack growth model. Both examples illustrated the robustness and efficiency of the proposed algorithm.

Generally, the results show that the proposed algorithm can achieve the same accuracy level as the static discretization with less than half of the number of intervals used. Also, it avoids the need to manually iterate through different static discretization methods and resolution levels to achieve convergence. Moreover, this algorithm can be applied to the inference of initial crack size distribution, which gave a very accurate estimation of initial crack occurrence probability at the "tail region". In spite of the significant potential of this algorithm, the accuracy of reliability estimation is still highly sensitive to the generation of CPTs. The method of CPTs generation was improved based on Straub's method. The proposed method removes the need for complex numerical integration of each bin.

The lifetime load updating strategy and the DBN-based crack growth model were integrated in final case study. A stiffened panel on the upper deck of the JHSS midsection was used as an example. An initial edge crack on the flange was assumed and XFEM techniques were applied to capture the crack propagation and determine the stress intensity factor as crack size grew. Both lifetime hogging and sagging moment distributions were updated to obtain the stress range distribution as fatigue load input. Finally, the updated stress range and stress intensity factor results as well as crack inspection record were integrated into a DBN-based stochastic crack growth model. With the help of the proposed dynamic discretization algorithm, the reliability index was compared before and after receiving those SHM information. The

results show that both load updating and crack inspection updating are necessary to achieve an accurate reliability estimation, thereby demonstrating the value of the developments in this thesis.

6.2 Recommendations for future work

In the future, alternative updating parameters for the proposed load updating framework should be investigated. These parameters should be more flexible in representing measured load distribution and indicate the bias of design parameters. Another potential extension would be to apply a similar approach to updating the extreme load distribution for a ship's ultimate strength analysis. Since the current focus involves the load range distribution for fatigue estimation, the accuracy of load distribution around rare events has never been investigated. This might also involve with updating multiple, distinct, physical loading processes, such as wave-induced bending and slamming. Also using the convolution integral to transfer from the load peak distribution to the load range distribution assumes that hogging and sagging moments are independent with each other. Relaxing or further exploring this assumption would be of value. An alternative way of updating the load range distribution would involve directly by treating the load range as a variable and relating it to design input parameters.

For the life-cycle fatigue management model, performance predictions for multiple crack locations prediction by using proposed fracture mechanics based on a DBN model might be explored. Since the number of nodes for each time slice is expected to increase significantly, a corresponding efficient DBN inference algorithm should be developed. The DBN model might also be extended to combine both crack initiation and crack propagation stages. Therefore, the total number of cycles to the failure would be updated instead of crack propagation cycles. A sensitivity analysis would be performed to investigate the dominate parameters and would help support the

decision making process.

A test against independent real world SHM data sources should be performed with more complicated structural details. This could involve either laboratory data or a real-world vessel structure. Multiple crack locations are expected and the proposed model should be able to track these different cracks as well as reflect the information of each structural detail and a general assessment of vessel condition.

APPENDICES

APPENDIX A

EXTENDED FINITE ELEMENT (XFEM) FOR CRACK GROWTH SIMULATION

A.1 Introduction

The idea of XFEM is to model the crack discontinuity by enriched elements. This thereby avoids mesh updating when the crack propagates. Therefore, unlike the conventional FE method, XFEM can use a constant mesh during crack growth, thereby making possible a direct cycle-by-cycle fatigue simulation possible. A more detailed introduction of XFEM will be presented in this appendix. A review of XFEM development will be given in Section 2, which is then followed by a detailed introduction of XFEM technique in Section 3. Two examples, a mode I crack case and a mixed mode crack case will be given in order to validate the XFEM approach in Section 4. The conclusions will be made in Section 5.

A.2 A review of XFEM development

The effort to develop an extended finite element methodology can be traced back to 1999 when *Belytschko and Black* (1999) presented a minimal remeshing finite

element method to model crack growth. Later on, *Moes et al.* (1999) improved the method and gave the method a formal name–the extended finite element (XFEM). This method allowed for the representation of the crack by constructing the enriched element by means of two more terms for the representation of discontinuity. *Sukumar and Moës* (2000) then extended this method to model three dimensional cracks. The computational geometry issues associated with the representation of the crack and the enrichment of the finite element approximation were also addressed. Level set methods were first introduced by *Stolarska et al.* (2001) for the modeling of crack propagation. *Belytschko et al.* (2001) approximated discontinuities in terms of a signed distance functions by using the Galerkin method so that level sets could be used to update the position of the discontinuities. In addition to these major contributions, other extensions of XFEM methods can be found in a number of available review papers and documents, including *Belytschko et al.* (2009), *Pommier* (2011), *Yazid et al.* (2009) ,*Mohammadi and online Library.* (2008), *Lua et al.* (2009), and *Lua et al.* (2010).

A.3 Introduction of XFEM method

A.4 Governing equation of FE

Consider the domain Ω bounded by Γ. The boundary Γ is composed of the sets Γ_u, Γ_t, and Γ_c, such that $\Gamma = \Gamma_u \bigcup \Gamma_t \bigcup \Gamma_c$. This is shown in Fig. A.1. Prescribed displacements are imposed on Γ_u, while tractions are imposed on Γ_t. The crack surface Γ_c is assumed to be traction-free. The equilibrium equations and boundary

conditions are

$$\begin{aligned} \nabla \cdot \boldsymbol{\sigma} + \boldsymbol{b} = 0 \quad & in \quad \Omega \\ \boldsymbol{\sigma} \cdot \boldsymbol{n} = \bar{\boldsymbol{t}} \quad & on \quad \Gamma_t \\ \boldsymbol{\sigma} \cdot \boldsymbol{n} = 0 \quad & on \quad \Gamma_{c^+} \\ \boldsymbol{\sigma} \cdot \boldsymbol{n} = 0 \quad & on \quad \Gamma_{c^-} \end{aligned} \tag{A.1}$$

where $\boldsymbol{n}$ is the unit outward normal, σ is the Cauchy stress, and b is the body force per unit volume. If small strains and displacements are considered, the kinematics equations therefore consist of the strain-displacement relation

$$\boldsymbol{\varepsilon} = \boldsymbol{\varepsilon}(\boldsymbol{u}) = \nabla_s \boldsymbol{u} \tag{A.2}$$

where ∇_s is the symmetric part of the gradient, and ε is the linear strain tensor. The constitutive relation is given by Hooke's Law,

$$\boldsymbol{\sigma} = \boldsymbol{C} : \boldsymbol{\varepsilon} \tag{A.3}$$

where $\boldsymbol{C}$ is the Hooke tensor. The corresponding weak form of the equilibrium equa-

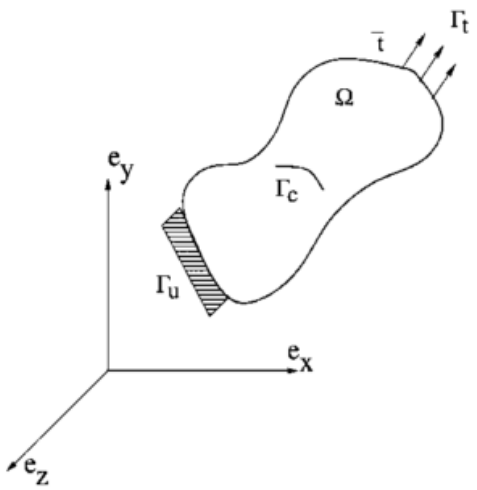

Figure A.1: Body with internal boundary subjected to loads (*Belytschko and Black*, 1999).

tions can be written as

$$\int_{\Omega} \boldsymbol{\sigma} : \boldsymbol{\varepsilon}(\boldsymbol{v}) d\Omega = \int_{\Omega} \boldsymbol{b} \cdot \boldsymbol{v} d\Omega + \int_{\Gamma_t} \bar{\boldsymbol{t}} \cdot \boldsymbol{v} d\Gamma \tag{A.4}$$

A.4.1 Discontinuity modeling by element enrichment

Consider x, a point in a two-dimensional FE model. Also, assume there is a discontinuity in the arbitrary domain discretized into some n node finite elements. In the XFEM, the following approximation is utilized to calculate the displacement for the point x locating within the domain as shown in Fig. A.2

$$\boldsymbol{u}^h = \sum_{i \in I} \boldsymbol{u}_i \phi_i + \sum_{j \in J} \boldsymbol{b}_j \phi_j H(\boldsymbol{x}) + \sum_{k \in K} \phi_k (\sum_{l=1}^{4} \boldsymbol{c}_k^l F_l(\boldsymbol{x})) \tag{A.5}$$

where the first term derives from standard FE, the second term is the element enriched by discontinuity function which is denoted by circled nodes in Fig. A.2, and the third term is the element enriched by crack tip enrichment function which is denoted by squared nodes in Fig. A.2. The last two terms utilizes additional degrees of freedom in order to facilitate modeling the existence of any discontinuous field, such as a crack, without modeling it explicitly in the finite element mesh. Also ϕ is the shape function, and $H(\boldsymbol{x})$ is a heave-side function which is defined as

$$H(\boldsymbol{x}) = \begin{cases} 1 & \text{for} \quad \boldsymbol{x} > 0 \\ -1 & \text{for} \quad \boldsymbol{x} < 0 \end{cases} \tag{A.6}$$

And the functions $F_l(\boldsymbol{x})$ are defined from LEFM asymptotic stress field around the crack tip.

$$\{F_l(r,\theta)\} = \{\sqrt{r}\sin(\frac{\theta}{2}), \sqrt{r}\cos(\frac{\theta}{2}), \sqrt{r}\sin(\theta), \sqrt{r}\cos(\frac{\theta}{2})\sin(\theta)\} \tag{A.7}$$

where (r,θ) are the local polar co-ordinates at the crack tip. There are three types of degrees of freedom that need to be solved: $\boldsymbol{u}_i$ are the nodal displacements, and $\boldsymbol{b}_j$

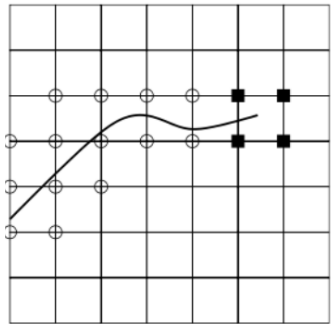

Figure A.2: Element enrichment for an arbitrary crack placed on a mesh.

and $\boldsymbol{c}_k^l$ are vectors of additional degrees of nodal freedom for modelling crack faces and crack tip, respectively.

A.4.2 Crack location track by level set method

In the XFEM framework, discontinuities are modeled independent of the finite element mesh. This creates the problem of how to keep track of the evolution of the cracks as they are not explicitly defined by the finite element mesh. One powerful tools for tracking interfaces is the level set method. In level set method, the interface of the crack is represented as two orthogonal level set functions. The $\psi(x)$ level set is used to track the crack body, while the $\phi(x)$ level set is used to track the crack tip. More specifically, the $\psi(x)$ and $\phi(x)$ level set functions are defined as follows:

$$\begin{aligned} &\psi(x) < 0 \;\text{ below crack path} && \phi(x) < 0 \;\text{ behind crack tip} \\ &\psi(x) > 0 \;\text{ above crack path} && \phi(x) > 0 \;\text{ in front of crack tip} \\ &\psi(x) = 0 \;\text{ along crack path} && \phi(x) = 0 \;\text{ at crack tip} \end{aligned} \tag{A.8}$$

One common choices for the level set functions involves simply defining in terms of the signed distance function. As the crack grows, the $\phi(x)$ and $\psi(x)$ level set functions need to be updated in order to capture the evolution of the crack.

One drawback of the level set method is that the function is one dimension higher than the dimension of the interface which potentially leads to higher storage and

computational costs.

A.4.3 J-integral for computing stress intensity factor

The displacement, strain, and stress obtained by XFEM can then be used for evaluation of the stress intensity factor K and the energy release rate G by a path-independent contour J-integral. A general expression of J-integral for a crack along the x axis of isotropic elastic material can be defined as

$$J = \int_{\Gamma} (W_s \mathrm{d}y - \boldsymbol{t}\frac{\partial \boldsymbol{u}}{\partial x}\mathrm{d}\Gamma) \tag{A.9}$$

where W_s is the strain energy density $W_s = \int_0^{\varepsilon} \sigma_{ij}\mathrm{d}\varepsilon_{ij}$, t is the traction vector, and $\boldsymbol{u}$ is the displacement vector. For general mixed-mode problems we have the following relationship between the value of the J-integral and the stress intensity factors

$$J = \frac{K_I^2}{E^*} + \frac{K_{II}^2}{E^*} \tag{A.10}$$

where E^* is defined in terms of Young's modulus E and Poisson's ratio v as

$$E^* = \begin{cases} E & \text{plane stress} \\ \frac{E}{1-v^2} & \text{plane strain} \end{cases} \tag{A.11}$$

To solve for the K_I and K_{II}, a auxiliary stress field is introduced, which should satisfy both the equilibrium equation and the traction free boundary condition on the crack face. If state 1, $(\sigma_{ij}^{(1)}, \varepsilon_{ij}^{(1)}, u_i^{(1)})$, corresponds to the present state and state 2, $(\sigma_{ij}^{(2)}, \varepsilon_{ij}^{(2)}, u_i^{(2)})$, is an auxiliary state that will be chosen as the asymptotic fields for modes I or II. The J-integral for the sum of the two states is

$$J^{(1+2)} = \int_{\Gamma} [\frac{1}{2}(\sigma_{ij}^{(1)} + \sigma_{ij}^{(2)})(\varepsilon_{ij}^{(1)} + \varepsilon_{ij}^{(2)})\delta_{1j} - (\sigma_{ij}^{(1)} + \sigma_{ij}^{(2)})\frac{\partial(u_i^{(1)} + u_i^{(2)})}{\partial x_1}]n_j \mathrm{d}\Gamma \tag{A.12}$$

In order to solve for the mixed mode fracture problem, we make a judicious choice of auxiliary state. Considering state 2 as pure mode I asymptotic fields with $K_I^{(2)} = 1$

gives mode I stress intensity factor for state 1 in terms of the interaction integral. The stress intensity factor for mode II can be determined in a similar fashion.

A.4.4 Crack growth direction

The direction of the crack propagation is established as a function of the mixed-mode stress intensity factors at the crack tip. There are several different criteria for choosing the direction from the calculation. Some of the most widely used mixed mode criteria are: the maximum tangential stress criterion, the maximum energy release rate criterion, the zero K_{II} criterion ($K_{II} = 0$), and the maximum circumferential stress criterion. Here only maximum circumferential stress criteria will be introduced.

The maximum circumferential stress criterion assumes that the crack will propagate from its tip in a direction θ_c, so that the circumferential stress $\sigma_{\theta\theta}$ in the direction of the crack propagation is a principal stress. The expression of a stress field around the crack tip circumferential stress and the shear stress equation under mixed mode loadings are given as follows

$$\begin{aligned}\left\{ \begin{array}{c} \sigma_{\theta\theta} \\ \sigma_{r\theta} \end{array} \right\} =& \frac{K_I}{\sqrt{2\pi r}} \frac{1}{4} \left\{ \begin{array}{c} 3\cos(\theta/2) + \cos(3\theta/2) \\ \sin(\theta/2) + \sin(3\theta/2) \end{array} \right\} \\ &+ \frac{K_{II}}{\sqrt{2\pi r}} \frac{1}{4} \left\{ \begin{array}{c} -3\sin(\theta/2) - 3\sin(3\theta/2) \\ \cos(\theta/2) + 3\cos(3\theta/2) \end{array} \right\}\end{aligned} \tag{A.13}$$

Then θ_c can be determined by setting the shear stress $\sigma_{r\theta}$ into zero which is given as

$$\theta_c = 2\arctan\frac{1}{4}\left[\frac{K_I}{K_{II}} - sign(K_{II})\sqrt{(\frac{K_I}{K_{II}})^2 + 8}\right] \tag{A.14}$$

A.5 Example

Two validation examples are given here to compare the stress intensity factor results from XFEM with the results from analytical solutions or experiment. The first

example validates mode I edge crack and center crack. The second example validates the mixed mode crack. The results presented below are from a simple XFEM code implemented in Matlab (*Pais*, 2011) and have been re-checked by Abaqus 6.12 XFEM package. The crack domain uses a hexahedral reduced integration element type and the size of the element should be small enough that at least five elements exist on the crack face. After validation is performed, a similar strategy is applied to represent the more complicated model illustrated in Chapter Five.

A.5.1 Mode I crack validation

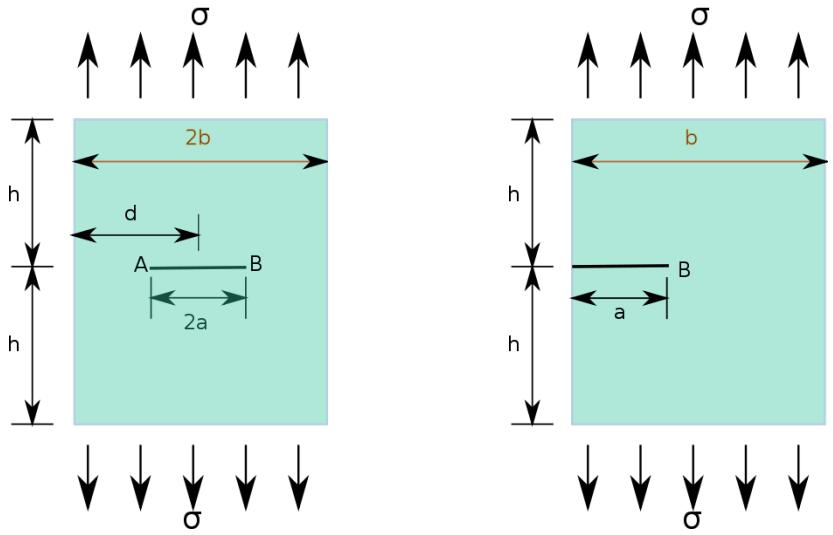

Figure A.3: Illustration of center crack (left) and edge crack.

As shown in Fig. A.3, a center crack and an edge crack case are examined. Both cases have the same plate dimension with $2h = 2$ m and $b = 1$ m and is made of steel. A Uniform stress is applied to each side of the plate with an amplitude of 1. The stress intensity factor is extracted which is then transferred to the geometric function according to Eq. 4.13. For both cases, the experiment results are also available which

are shown as follows:

$$\begin{aligned} &\text{Center Crack} \quad F(\alpha) = \frac{1 - 0.5\alpha + 0.326\alpha^2}{\sqrt{1-\alpha}} \quad \text{for } \frac{h}{b} \geq 1.5 \\ &\text{Edge Crack} \quad F(\alpha) = 0.265(1-\alpha)^4 + \frac{0.857 + 0.265\alpha}{(1-\alpha)^{3/2}} \quad \text{for } \frac{h}{b} \geq 1.0 \end{aligned} \tag{A.15}$$

where $\alpha = a/b$. The comparisons of geometric function between the XFEM results and the experiment results under different crack size are shown in Fig. A.4. It can be seen that for both edge and center crack cases, the XFEM results are consistent with the results of the experiment, while the cost of XFEM simulation is much lower than a case by case experiment.

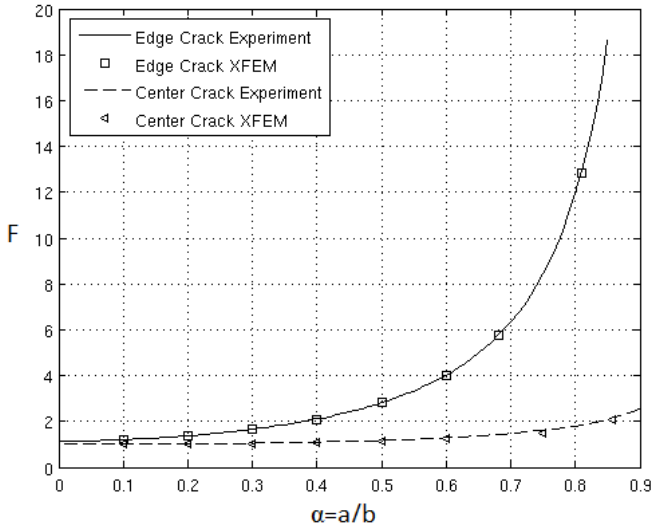

Figure A.4: The geometric function between XFEM results and experiment results for center crack and edge crack.

A.5.2 Mixed mode crack validation

A mixed mode crack case is also validated as illustrated in Fig. A.5. This involves a slanted crack of length $2a$ in an uni-axial stress field σ in a infinite plate. The β is the angle made by the crack with the x axis. Analytical solutions are available for

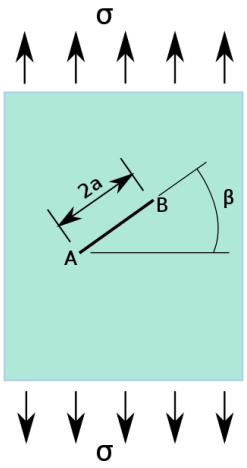

Figure A.5: Illustration of mixed mode crack.

both mode I and mode II intensity factors through LEFM which are given as follows:

$$\begin{aligned} K_I = &\quad \sigma \cos\beta^2 \sqrt{\pi a} \\ K_{II} = &\quad \sigma \sin\beta \cos\beta \sqrt{\pi a} \end{aligned} \tag{A.16}$$

The Fig. A.6 shows the geometric function for mixed mode crack using XFEM. Again, it can been seen that for both mode I and mode II stress intensity factors, the results compare favourably with LEFM results.

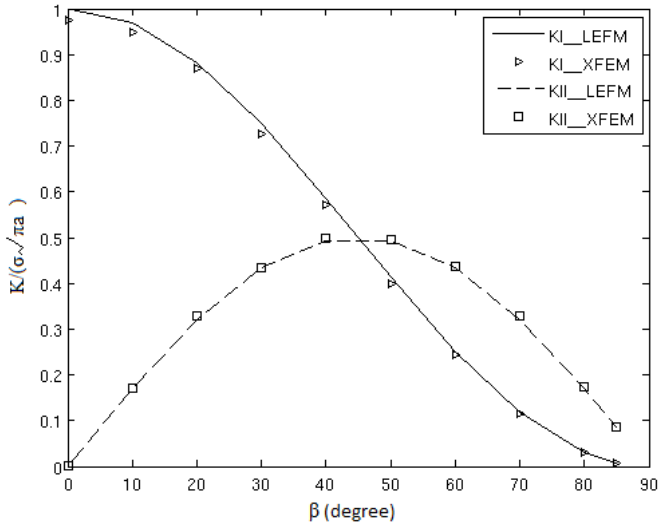

Figure A.6: The geometric function between XFEM results and LFEM results for a mixed mode crack.

BIBLIOGRAPHY

BIBLIOGRAPHY

Albert, J. H., and S. Chib (1993), Bayesian analysis of binary and polychotomous response data, *Journal of the American Statistical Association*, *88*(422), 669–679.

An, D., J.-H. Choi, N. H. Kim, and S. Pattabhiraman (2011), Fatigue life prediction based on Bayesian approach to incorporate field data into probability model, *Structural Engineering and Mechanics*, *37*(4), 427–442.

Bai, Y. (2003), *Marine structural design*, 606 pp., Elsevier.

Beck, J. L., and S.-K. Au (2002), Bayesian updating of structural models and reliability using Markov chain Monte Carlo simulation, *Journal of Engineering Mechanics*, *128*(4), 380–391.

Belytschko, T., and T. Black (1999), Elastic crack Growth in Finite Elements with Minimal Remeshing, *International Journal for Numerical Methods in Engineering*, *45*(5), 601–620.

Belytschko, T., N. Moes, S. Usui, and C. Parimi (2001), Arbitrary discontinuities in finite elements, *International Journal for Numerical Methods in Engineering*, *50*(4), 993–1013.

Belytschko, T., R. Gracie, and G. Ventura (2009), A review of extended/generalized finite element methods for material modeling, *Modelling and Simulation in Materials Science and Engineering*, *17*(4), 43,001–43,024.

Bensi, M., A. D. Kiureghian, and D. Straub (2013), Efficient Bayesian network modeling of systems, *Reliability Engineering & System Safety*, *112*, 200–213.

British Standards Institution (2005), *BS7910: Guide to methods for assessing the acceptability of flaws in metallic structures*, London.

Carlin, B. P., and T. A. Louis (2009), *Bayesian methods for data analysis*, 3rd ed., 552 pp., Chapman and Hall/CRC.

Chang, K. C., and H. D. Chen (2005), Efficient inference for hybrid dynamic Bayesian networks, *Optical Engineering*, *44*(7), 077,201–077,201–7.

Cheng, J., and M. Druzdzel (2000), AIS-BN: An adaptive importance sampling algorithm for evidential reasoning in large Bayesian networks, *Journal of Artificial Intelligence Research*, *13*, 155–188.

Cohen, M. L., S. S. Kulkarni, and J. D. Achenbach (2011), Probabilistic approach to growth and detection of a truncated distribution of initial crack lengths based on Paris' law, *Structural Health Monitoring*, *11*(2), 225–236.

Collette, M. (2011), Hull structures as a system: supporting lifecycle analysis, *Naval Engineers Journal*, *123*(3), 45–55.

Darwiche, A. (2009), *Modeling and reasoning with Bayesian networks*, 562 pp., Cambridge University Press, Cambridge.

Dirlik, T. (1985), Application of computer in fatigue analysis, Ph.D. thesis, University of Warwick.

Ditlevsen, O., and H. O. Madsen (1996), *Structural relaibility methods*, 384 pp., Wiley, New York.

Faber, M. H., D. Straub, E. Heredia-Zavoni, and R. Montes-Iturrizaga (2012), Risk assessment for structural design criteria of FPSO systems. Part I: Generic models and acceptance criteria, *Marine Structures*, *28*(1), 120–133.

Farrar, C. R., S. W. Doebling, and D. A. Nix (2001), Vibration-based structural damage identification, *Philosophical Transactions of the Royal Society A: Mathematical, Physical and Engineering Sciences*, *359*(1778), 131–149.

Flynn, E. B., and M. D. Todd (2010), Bayesian probabilistic structural modeling for optimal sensor placement in ultrasonic guided wave-based structural health monitoring, in *The International Society for Optical Engineering*, vol. 7648, p. 76480Z, San Diego, USA.

Friis-Hansen, A. (2000), Bayesian networks as a decision support tool in marine applications, Ph.D. thesis, Technical University of Denmark.

Gamerman, D., and H. F. Lopes (2006), *Markov chain Monte Carlo: stochastic simulation for Bayesian inference*, 2nd ed., 344 pp., Chapman and Hall/CRC.

Gao, Z., and T. Moan (2007), Fatigue damage induced by non-Gaussian bimodal wave loading in mooring lines, *Applied Ocean Research*, *29*(1-2), 45–54.

Garbatov, Y., and C. Guedes Soares (2009), Structural maintenance planning based on historical data of corroded deck plates of tankers, *Reliability Engineering & System Safety*, *94*(11), 1806–1817.

Geman, S., and D. Geman (1984), Stochastic relaxation, Gibbs distributions, and the Bayesian restoration of images, *Pattern Analysis and Machine Intelligence, IEEE Transactions on*, *PAMI-6*(6), 721–741.

Gogate, V., and R. Dechter (2005), Approximate inference algorithms for hybrid bayesian networks with discrete constraints, in *the Twenty-First Conference Annual Conference on Uncertainty in Artificial Intelligence (UAI-05)*, pp. 209–216, AUAI Press, Arlington, Virginia.

Goksyr, O. y. (2009), Hull integrity management: Best practises for maintenance of bulk carriers, in *International Conference on Design and Operation of Bulk Carriers*, pp. 73–82, Royal Institution of Naval Architects, Norway.

Guedes Soares, C., and Y. Garbatov (1996), Fatigue reliability of the ship hull girder accounting for inspection and repair, *Reliability Engineering & System Safety*, *51*(3), 341–351.

Hanson, J., A. Lübben, and M. L. M. Kaminski (2010), Wave measurements for the Monitas system, in *Offshore Technology Conference (OTC)*, pp. 1–12, Houston, US.

Hastings, W. K. (1970), Monte Carlo sampling methods using Markov chains and their applications, *Biometrika*, *57*(1), 97–109.

Heggelund, S. E., G. Storhaug, and B.-K. Choi (2011), Full scale measurements of fatigue and extreme loading including whipping on an 8600TEU post panamax container vessel in the asia to Europe trade, in *the International Conference on Offshore Mechanics and Arctic Engineering (OMAE)*, vol. 2, pp. 273–282, American Society of Mechanical Engineers.

Heredia-Zavoni, E., R. Montes-Iturrizaga, M. H. Faber, and D. Straub (2012), Risk assessment for structural design criteria of FPSO systems. Part II: Consequence models and applications to determination of target reliabilities, *Marine Structures*, *28*(1), 50–66.

Hosti, D. L., M. L. M. Kaminski, and P. Aalberts (2010), Overview of the Monitas JIP, in *Offshore Technology Conference (OTC)*, pp. 1–9, Houston, US.

Hughes, O. F., and J. K. Paik (2010), *Ship structural analysis and design*, Society of Naval Architects and Marine Engineers(SNAME), Jesey City, New Jensey.

Jensen, F. V. (1996), *An introduction to Bayesian networks*, 178 pp., Springer, New York.

Jensen, F. V., S. L. Lauritzen, and K. G. Olessen (1990), Bayesian updating in causal probabilistic networks by local computations, *Computational Staistics Quarterly*, (4), 269–282.

Jensen, J., and A. Mansour (1994), Inspection planning for fatigue damage using Bayesian updating, in *the 6th International Conference on Structural Safety and Reliability (ICOSSAR'93)*, pp. 1185–1188, A.A. Balkema, Innsbruck, Austria.

Jensen, J., and A. Mansour (2002), Estimation of ship long-term wave-induced bending moment using closed-form expressions, *RINA Transactions*, pp. 41–55.

Jensen, J., A. Mansour, and A. Olsen (2004), Estimation of ship motions using closed-form expressions, *Ocean Engineering*, *31*(1), 61–85.

Jensen, J. J. (2001), *Load and global response of ships*, 352 pp., Elsevier Science.

Jiao, G., and T. Moan (1990), Methods of reliability model updating through additional events, *Structural Safety*, *9*(2), 139–153.

Kalman, R. E. (1960), A new approach to linear filtering and prediction problems, *Transactions of the ASME–Journal of Basic Engineering*, *82*(Series D), 35–45.

Kesavan, A., S. John, and I. Herszberg (2007), Structural health monitoring of composite structures using artificial intelligence protocols, *Journal of Intelligent Material Systems and Structures*, *19*(1), 63–72.

Kim, B., X. Wang, and Y.-S. Shin (2007), Extreme load and fatigue damage on FPSO in combined waves and swells, in *10th International symposium of practical design of ships and other floating structures*, pp. 203–210, Houston, US.

Langseth, H., T. Nielsen, R. Rumí, and A. Salmerón (2009), Inference in hybrid Bayesian networks, *Reliability Engineering & System Safety*, *94*(10), 1499–1509.

Larsen, R. J., and M. L. Marx (2012), *An introduction to mathematical statistics and its applications*, 5th ed., 768 pp., Prentice Hall, Boston.

Lauritzen, S. L., and D. J. Spiegelhalter (1988), Local computations with probabilities on graphical structures and their application to expert systems, *Journal of the Royal Statistical Society. Series B*, *50*(2), 157–224.

Lauritzen, S. L., A. P. Dawid, B. N. Larsen, and H.-G. Leimer (1990), Independence properties of directed markov fields, *Networks*, *20*(5), 491–505.

Lee, Y., J. Pan, R. Hathaway, and M. Barkey (2004), *Fatigue testing and analysis: theory and practice*, 1–416 pp., Elsevier Butterworth-Heinemann.

Lepar, V., and P. P. Shenoy (1998), A comparison of Lauritzen-Spiegelhalter, Hugin, and Shenoy-Shafer architectures for computing marginals of probability distributions, *Uncertainty in Artificial Intelligence*, *14*, 328–337.

Lin, W.-M., J. Bergquist, M. Collette, D. Liut, T. Treakle, K. Weems, M. Weems, and S. Zhang (2008), Large Amplitude Motion Program (LAMP) for ship motions and wave loads predictions, *Tech. rep.*, Science Applications International Corporation.

Ling, Y., and S. Mahadevan (2012), Integration of structural health monitoring and fatigue damage prognosis, *Mechanical Systems and Signal Processing*, *28*, 89–104.

Lo Nigro, A., L. Brunori, G. Guassardo, and Panebianco (2005), Risk based approach to oil tankers and bulk carriers vetting, in *Offshore Mediterranean Conference and Exhibition*, Ravenna, Italy.

Lua, J., J. Shi, P. Liu, and N. Thammadi (2009), XFEM toolkit for crack path and life prediction of aluminum structures, in *50th AIAA/ASME/ASCE/AHS/ASC Structures, Structural Dynamics and Materials Conference*, Collection of Technical Papers - AIAA/ASME/ASCE/AHS/ASC Structures, Structural Dynamics and Materials Conference, American Institute of Aeronautics and Astronautics Inc., Princeton, US.

Lua, J., J. Shi, Z. Lu, and Y. Liu (2010), Life Prediction of Aerospace Structures by Combined XFEM and Advanced Fatigue Models, in *51st AIAA/ASME/ASCE/AHS/ASC Structures, Structural Dynamics, and Materials Conference*, Structures, Structural Dynamics, and Materials and Co-located Conferences, American Institute of Aeronautics and Astronautics, Orlando,US.

Lutes, L., M. Corazao, S. Hu, and J. Zimmerman (1984), Stochastic fatigue damage accumulation, *Journal of Structural Engineering*, *110*(12), 2585–2601.

Mahadevan, S., R. Zhang, and N. Smith (2001), Bayesian networks for system reliability reassessment, *Structural Safety*, *23*(3), 231–251.

Mansour, A. E., and J. P. Wasson (1995), Charts for estimating nonlinear hogging and sagging bending moments, *Journal of Ship Research*, *39*(3), 240–249.

Marquez, D., N. Martin, and N. Fenton (2010), Improved reliability modeling using Bayesian networks and dynamic discretization, *Reliability Engineering and System Safety*, *95*(4), 412–425.

Melchers, R. E. (1996), *Structural reliability analysis and prediction*, 2nd ed., 456 pp., Wiley, New York.

Méndez, A., and A. Csipkes (2013), Overview of fiber optic sensors for NDT applications, in *Nondestructive Testing of Materials and Structures SE - 26*, *RILEM Bookseries*, vol. 6, pp. 179–184, Springer Netherlands.

Metropolis, N., A. W. Rosenbluth, M. N. Rosenbluth, A. H. Teller, and E. Teller (1953), Equation of state calculations by fast computing machines, *Journal of Chemical Physics*, *21*(6), 1087–1092.

Miner, M. A. (1945), Cumulative damage in fatigue, *Journal of Applied Mechanics*, *12*(67), A159–A164.

Moan, T. (2011), Life-cycle assessment of marine civil engineering structures, *Structure and Infrastructure Engineering*, *7*(1-2), 11–32.

Moan, T., E. Ayala-Uraga, and X. Wang (2004), Reliability-based service life assessment of FPSO structures, in *SNAME Maritime Technology Conference & Expo*, Washington DC.

Moes, N., J. Dolbow, and T. Belytschko (1999), A finite element method for crack growth without remeshing, *International Journal for Numerical Methods in Engineering*, *46*(1), 131–150.

Mohammadi, S., and W. online Library. (2008), *Extended finite element method for fracture analysis of structures*, 280 pp., Wiley-Blackwell, Oxford ; Malden, MA.

Mohanty, S., A. Chattopadhyay, and P. Peralta (2010), Adaptive residual useful life estimation of a structural hotspot, *Journal of Intelligent Material Systems and Structures*, *21*(3), 321–335.

Mohanty, S., A. Chattopadhyay, P. Peralta, and S. Das (2011), Bayesian statistic based multivariate Gaussian process approach for offline/online fatigue crack growth prediction, *Experimental Mechanics*, *51*(6), 833–843.

Montes-Iturrizaga, R., E. Heredia-Zavoni, F. Vargas-Rodriguez, M. H. Faber, D. Straub, and J. de Dios de la O (2009), Risk based structural integrity management of marine platforms using Bayesian probabilistic nets, *Journal of Offshore Mechanics and Arctic Engineering*, *131*(1), 011,602.

Munse, W., T. Wilbur, M. Tellalin, K. Nicoll, and K. Wilson (1982), SSC-318: Fatigue characterization of fabricated ship details for design, *Tech. rep.*, Ship Structure Committe.

Murphy, K. (2001), The bayes net toolbox for matlab, *Computing Science and Statistics*, *33*, 1–20.

Neil, M., M. Tailor, and D. Marquez (2007), Inference in hybrid Bayesian networks using dynamic discretization, *Statistics and Computing*, *17*, 219–233.

Nielsen, U. D., and J. Jensen (2011), A novel approach for navigational guidance of ships using onboard monitoring systems, *Ocean Engineering*, *38*(2-3), 444–455.

Nielsen, U. D., J. Jensen, P. T. Pedersen, and Y. Ito (2011), Onboard monitoring of fatigue damage rates in the hull girder, *Marine Structures*, *24*(2), 182–206.

Ochi, M. K. (1990), *Applied probability and stochastic processes: In Engineering and Physical Sciences (Wiley Series in Probability and Statistics)*, \ ed., 520 pp., Wiley-Interscience.

Okada, T., Y. Takeda, and T. Maeda (2006), On board measurement of stresses and deflections of a Post-Panamax containership and its feedback to rational design, *Marine Structures*, *19*(2-3), 141–172.

Okasha, N. M., D. M. Frangopol, and A. Decò (2010a), Integration of structural health monitoring in life-cycle performance assessment of ship structures under uncertainty, *Marine Structures*, *23*(3), 303–321.

Okasha, N. M., D. M. Frangopol, D. Saydam, and L. W. Salvino (2010b), Reliability analysis and damage detection in high-speed naval craft based on structural health monitoring data, *Structural Health Monitoring*, *10*(4), 361–379.

Pais, M. (2011), MATLAB Extended Finite Element (MXFEM) Code v1.2, *www.matthewpais.com*.

Palmgren, A. (1924), Durability of ball bearings, *ZVDI*, *68*(14), 339–341.

Pascoal, R., and C. Guedes Soares (2009), Kalman filtering of vessel motions for ocean wave directional spectrum estimation, *Ocean Engineering*, *36*(6-7), 477–488.

Patil A, Huard D, F. C. (2010), PyMC: Bayesian stochastic modelling in Python, *Journal of Statistical Software*, *35*(4), 1–81.

Pommier, S. (2011), Extended finite element method for crack propagation.

Rabiei, M., and M. Modarres (2013a), Quantitative methods for structural health management using in situ acoustic emission monitoring, *International Journal of Fatigue*, *49*, 81–89.

Rabiei, M., and M. Modarres (2013b), A recursive Bayesian framework for structural health management using online monitoring and periodic inspections, *Reliability Engineering & System Safety*, *112*, 154–164.

Radaj, D. (1996), Review of fatigue strength assessment of nonwelded and welded structures based on local parameters, *International Journal of Fatigue*, *18*(3), 153–170.

Rice, S. O. (1945), Mathematical analysis of random noise, *Bell System Technical Journal*, *24*(1), 46–156.

Rooke, D. P., and D. J. Cartwright (1976), *Compendium of Stress Intensity Factors*, 330 pp., H.M. Stationery Office, London.

Rubner, Y., C. Tomasi, and L. J. Guibas (2000), The earth mover's distance as a metric for image retrieval, *International Journal of Computer Vision*, *40*(2), 99–121.

Sankararaman, S., Y. Ling, and S. Mahadevan (2010), Statistical inference of equivalent initial flaw size with complicated structural geometry and multi-axial variable amplitude loading, *International Journal of Fatigue*, *32*(10), 1689–1700.

Sankararaman, S., Y. Ling, and S. Mahadevan (2011), Uncertainty quantification and model validation of fatigue crack growth prediction, *Engineering Fracture Mechanics*, *78*(7), 1487–1504.

Sarkani, S., D. Kihl, and J. Beach (1994), Fatigue of welded joints under narrowband non-Gaussian loadings, *Probabilistic Engineering Mechanics*, *9*(3), 179–190.

Shenoy, P., and G. Shafer (1990), Axioms for probability and belief-function propagation, *Uncertainty in Artificial Intelligence*, *4*, 169–198.

Sikora, J. P. (1983), A method for estimating lifetime loads and fatigue lives for swatch and conventional monohull ships, *Naval Engineers Journal*, *95*(3), 63–85.

Sikora, J. P., R. W. Michaelson, and B. M. Ayyub (2002), Assessment of cumulative lifetime seaway loads for ships, *Naval Engineers Journal*, *114*(2), 167–180.

Souza, G., and B. Ayyub (2000), Probabilistic fatigue life prediction for ship structures using fracture mechanics, *Naval Engineers journalournal*, *112*(4), 375–397.

Stolarska, M., D. Chopp, N. Moës, and T. Belytschko (2001), Modelling crack growth by level sets in the extended finite element method, *International Journal for Numerical Methods in Engineering*, *51*(8), 943–960.

Storhaug, G., E. Moe, and G. Holtsmark (2007), Measurements of wave induced hull girder vibrations of an ore carrier in different trades, *Journal of Offshore Mechanics and Arctic Engineering*, *129*(4), 279–289.

Straub, D. (2009), Stochastic modeling of deterioration processes through dynamic Bayesian networks, *Journal of Engineering Mechanics*, *135*(10), 1089–1099.

Straub, D. (2011), Reliability updating with equality information, *Probabilistic Engineering Mechanics*, *26*(2), 254–258.

Straub, D., and A. Der Kiureghian (2008), Improved seismic fragility modeling from empirical data, *Structural Safety*, *30*(4), 320–336.

Straub, D., and M. H. Faber (2007), Temporal variability in corrosion modeling and reliability updating, *Journal of Offshore Mechanics and Arctic Engineering*, *129*(4), 265–272.

Straub, D., and A. D. Kiureghian (2010a), Bayesian network enhanced with structural reliability methods: application, *Journal of Engineering Mechanics*, *136*(10), 1259–1270.

Straub, D., and A. D. Kiureghian (2010b), Bayesian network enhanced with structural reliability methods: methodology, *Journal of Engineering Mechanics*, *136*(10), 1248–1258.

Sukumar, N., and N. Moës (2000), Extended finite element method for threedimensional crack modelling, *International Journal for Numerical Methods in Engineering*, *48*(11), 1549–1570.

Suresh, S. (1998), *Fatigue of materials*, 2nd ed., 683 pp., Cambridge University Press.

Tada, H., P. C. Paris, and G. R. Irwin (2000), *The Stress analysis of cracks handbook*, 3 ed., 677 pp., ASME Press, New York.

Takaoka, Y., K. Nihei, P. Vargas, and P. Aalberts (2010), Application of fatigue damage sensors in the monitas system, in *Offshore Technology Conference (OTC)*, pp. 1–8, Houston, US.

Wang, G., M. Lee, C. Serratella, S. Botten, S. Ternowchek, D. Ozevin, J. Thibault, and R. Scott (2010), Testing of acoustic emission technology to detect cracks and corrosion in the marine environment, *Journal of Ship Production and Design*, *26*(2), 5.

Wang, X., and J. Sun (2005), Effect of skewness on fatigue life with mean stress correction, *Journal of Sound and Vibration*, *282*(3-5), 1231–1237.

Wang, Y. (2010), Spectral fatigue analysis of a ship structural detail A practical case study, *International Journal of Fatigue*, *32*(2), 310–317.

Weber, P., G. Medina-Oliva, C. Simon, and B. Iung (2012), Overview on Bayesian networks applications for dependability, risk analysis and maintenance areas, *Engineering Applications of Artificial Intelligence*, *25*(4), 671–682.

Winterstein, S. R. (1988), Nonlinear vibration models for extremes and fatigue, *Journal of Engineering Mechanics*, *114*(10), 1772–1790.

Winterstein, S. R., and T. Kashef (2000), Moment-based load and response models with wind engineering applications, *Journal of Solar Energy Engineering*, *122*(3), 122–128.

Wirsching, P., and E. B. Haugen (1974), A general statistical model for random fatigue, *Journal of Engineering Materials and Technology*, *96*(1), 34–40.

Wirsching, P., and A. Shehata (1977), Fatigue under wide band random stresses using the rain-flow method, *Journal of Engineering Materials and Technology*, *99*(3), 205–211.

Wirsching, P. H., and M. C. Light (1980), Fatigue under wide band random stresses, *Journal of the Structural Division*, *106*(7), 1593–1607.

Wu, M., and T. Moan (2006), Numerical prediction of wave-induced long-term extreme load effects in a flexible high-speed pentamaran, *Journal of Marine Science and Technology*, *11*(1), 39–51.

Yamamoto, N., T. Koiwa, H. Dobashi, O. Muragishi, and Y. Takaoka (2007), A study of a fatigue management system for long LNG carriers using a new fatigue damage sensor, *Ships and Offshore Structures*, *2*(4), 361–370.

Yang, J., and S. Manning (1996), A simple second order approximation for stochastic crack growth analysis, *Engineering Fracture Mechanics*, *53*(5), 677–686.

Yazid, A., N. Abdelkader, and H. Abdelmadjid (2009), A state-of-the-art review of the X-FEM for computational fracture mechanics, *Applied Mathematical Modelling*, *33*(12), 4269–4282.

Yu, L., P. K. Das, and N. D. P. Barltrop (2004), A new look at the effect of bandwidth and non-normality, *Fatigue & Fracture of Engineering Materials & Structures*, *27*(1), 51–58.

Zárate, B. a., J. M. Caicedo, J. Yu, and P. Ziehl (2012), Bayesian model updating and prognosis of fatigue crack growth, *Engineering Structures*, *45*, 53–61.

Zhu, B., and D. M. Frangopol (2013), Reliability assessment of ship structures using Bayesian updating, *Engineering Structures*, *56*, 1836–1847.

Zhu, J., and M. Collette (2011), Lifecycle fatigue management for high-speed vessels using local approaches, in *11th International Conference on Fast Sea Transportation*, Honolulu, Hawaii, USA.

Zhu, J., and M. Collette (2013), A dynamic discretization method for reliability inference in dynamic Bayesian networks, *submitted to Reliability Engineering & System Safety*.